Development of Charcoal-Based Nanofluids for Enhanced Oil Recovery

Ifeoluwa Zainab Akande

Doctor of Philosophy

Aston University

September 2023

Development of Charcoal-Based Nanofluids for Enhanced Oil Recovery

Ifeoluwa Zainab Akande

Doctor of Philosophy

Thesis Summary

Amid global efforts to combat climate change and transition to renewable energy sources, the importance of oil and gas for meeting current energy demands remains undeniable. As initiatives like the Paris Agreement aim to limit global warming, cost-effective and sustainable methods for oil recovery become increasingly crucial. This study delves into the development of charcoal-based nanofluids for enhanced oil recovery (EOR) flooding.

Oil recovery is carried out in stages; The first is the primary stage via natural pressure depletion, which generally drives about 20% of the original oil in place (OOIP) to the oil well. Next is the secondary stage also known as water flooding, at this stage, an incremental recovery of ~30% of OOIP can be achieved from a high-quality reservoir. To further recover the remaining 60-70% OOIP, the tertiary stage also known as the EOR (enhanced oil recovery), is applied, which can recover an additional 10-30% of OOIP at the best case scenario.

The fluid flooding of EOR needs to overcome the flow path formed during water flooding and effectively spread to a large volume of the complicated structured reservoir driving out the oil in a mixture of brine and gas.

Nanofluids of various metal oxides such as SiO_2 and TiO_2, Al_2O_3 and Fe_2O_3 have been examined for their performance in enhanced oil recovery and have demonstrated an oil recovery capacity of 8-16% of the original oil in place (OOIP) after water flooding for SiO_2, Al_2O_3 and TiO_2.

Charcoals derived from abundant and agricultural wastes rice husk (RHC), wheat straw char (WSC) as well as active carbon (AC) as a reference sample were selected for this study. The study covers the preparation and characterisation of their aqueous nanofluids for size/size distribution of nanoparticles, nanoparticle surface chemistry and interaction with each other, and more importantly, their enhancement on the viscosity of the aqueous charcoal-based nanofluids. The charcoal nanofluids were prepared by wet milling in water. Size analysis detected the nanoparticle size approximately at 154 nm for RHC, 96 nm for WSC and 210 nm for AC at pH 7.0. These sizes varied with the pH values of the nanofluids according to their surface chemistry.

The viscosity of the charcoal-based nanofluids was systematically studied for the effect of charcoal concentration (0.5 - 2.5 wt%) and pH values (pH 2.0-pH 11.0). The viscosity enhancement was observed from the three types of charcoal-based nanofluids in the concentration and pH ranges studied. The enhancement was evaluated by the Dispersion Factor (DF), which is proposed in this study based on Chen et al. (2007) equation to comprehensively evaluate the effect of nanoparticle

dispersion in a fluid on its viscosity. The higher the dispersion factor, the stronger the interaction of the nanoparticles to the dispersion liquid, and the higher the viscosity enhancement. The DF values of RHC and WSC nanofluids were slightly higher than those of the nanofluids of TiO_2 and SiO_2 with 5-10 times smaller particle sizes in the literature. More impressively the viscosity enhancement of AC nanoparticles is comparable to that of carbon nanotubes at concentrations below 0.6 vol.% and surpasses carbon nanotubes when the concentration is higher than 0.6 vol.%. The viscosity study shows the potential of the charcoal-based nanofluids to enhance their oil displacement efficiency in EOR.

The EOR flooding tests of the charcoal-based nanofluids were conducted on sand-packed cores to mimic sandstone-dominated oil reservoirs. A sectional flooding method is applied, i.e., the nanofluids equivalent to 20% of the pore volume were injected into the packed cores after water flooding saw a levelled oil recovery rate. Water flooding was restored after the nanofluid injection. The effect of nanoparticle concentrations and pH levels of the nanofluids were examined on the enhanced oil recovery. The results showed that 1) a higher nanofluid concentration recovered more original oil in place in the range of 15.4% - 19.3% of OOIP for AC pH 6.0 1 wt% and 2 wt% respectively; 2) the pH value of the nanofluids had a sensible effect on their EOR performance. At a pH that the nanofluids showed a higher viscosity, the oil recovery rate is higher. 3) Most impressively the active carbon nanofluid at pH 2.0 demonstrated a manipulatable flow pattern by pH value in the side of the packed core and eventually yielded a notable further 34.1% of original oil-in-place at a concentration of 2 wt%.

Overall, the findings underscore the promising potential of charcoal-based nanofluids as effective EOR flooding fluids. Their abundant renewable nature, as a by-product of biofuel productions and low-cost position them as attractive alternatives of viscosity enhancement agents for advancing EOR technologies and, meanwhile, storing the carbon-rich nanoparticles in the oil reservoir after utilisation.

Keywords: charcoal nanoparticles, charcoal-based nanofluids, viscosity enhancement, enhanced oil recovery

Acknowledgements

Over the past 4 years, I have worked hard to make sure that the sacrifice of those around me does not go to waste, and so I can be proud of what I achieve in the end. There is a saying in Nigeria, “It takes a village to raise a child”, I see my thesis as a child, and I would like to thank the village that made it possible.

To my Supervisors, Dr Qing Yuan, and Prof. Tony Bridgewater, who trusted me to take on this challenge and provided me with full support and guidance throughout the journey, I want to say thank you.

To the staff, lecturers, and researchers at EBRI (Energy & Bioproducts Research Institute) and Aston University, such as Iram, Reni, Jinesh, Daniel, Jude, Carmen, Helena, Jai, Regina, Petra, among so many other great people. Thank you.

To those at RCCG House of Praise Christian Centre, who prayed for me non-stop, Tayo, Moyo, Abiola, Gozie, Funke, Esther, Esther, Niyi, Ayo, Ola, Ayo, Ayo, Debbie, Ore g, Ore b, Tife, Tayo, Rebekha, and other amazing people. Thank you.

To my 22+ friends, Racheal, Lb, Hannah, Lizzie, Eunice, Seyi, Simi and Smith. Thank you.

To my loving family, Toyin, Mummy Omotoso, Daddy Omotoso, Jola, Simi, Janet, Tola, Eniola, SOJ and Tunde. Thank you.

To my amazing Fiancé Femi, thank you for the encouragement and support. I love and appreciate you.

Finally, I would like to say thank you to the one who made it all happen, the reason I am here today, God.

I dedicate this thesis to my late father, Dr Adewale Taofiki Akande, the man who taught me that nothing is impossible if you set your mind on it.

This is for you Daddy!

Table of Contents

List of Abbreviations and Acronyms

σ_{ow}	Interfacial energy between oil and water
σ_{ws}	Interfacial energy between water and solid
[μ]	Intrinsic viscosity

μ	Dynamic viscosity
AC	Active carbon
ASP	Alkaline surfactant polymer
daf	Dry ash-free
db	Dry basis
DF	Dispersion Factor
DLS	Dynamic light scattering
EOR	Enhanced oil recovery
ICP	Inductively Coupled Plasma
k	Permeability
M	Mobility ratio
OOIP	Original oil in place
PZC	Point of zero charge
RHC	Rice husk char
WSC	Wheat straw char
λ	Mobility
μ_{eff}	Effective dynamic viscosity
μ_{bf}	Dynamic viscosity of the base fluid
φ_m	Maximum particle volume fraction
σ_{os}	Interfacial energy between oil and solid

List of Figures

List of Tables

1. Chapter 1: Introduction to Research and Motivation

1.1. Research background and motivation

Oil and gas have been the major resources for energy, and chemical feedstock and supported the so-called carbon economy for nearly a century. The use of oil and gas as well as coal has resulted in the concentration increase of greenhouse gases and significant global warming, with coal, oil and gas accounting for over 75% of the global greenhouse gas emissions and nearly 90% of all carbon dioxide emissions [1].

World leaders and scientists are striving to combat this global warming emergency in the form of, the Paris Agreement signed in 2016, stating that the global temperature should be kept below 2°C above pre-industrial levels and limited to an increase of 1.5°C [2]. Additionally, initiatives at regional levels, such as the European Commission's target to reduce greenhouse gas emissions by at least 40% from 1990 levels by 2030 [3], and the Committee on Climate Change's (CCC) goals for net-zero greenhouse gas (GHG) emissions in England by 2050, Scotland by 2045, and a 95% reduction in greenhouse gases in Wales by 2050 [4].

To achieve these long-term temperature goals, Zero-carbon solutions have been under development and becoming competitive across economic sectors representing 25% of emissions [2] and expected to be competitive in other sectors representing over 70% of global emissions by 2030. This includes the increase in the UK production of alternative energy sources like wind, solar and hydro with about 7% (30 TWh) more renewable generation in 2023 than in 2022 [5].

Although oil accounts for over 75% of global greenhouse gas emissions, the consumption of oil and gas has been continuously increasing, e.g., to 3.15×10^{10} barrels of oil equivalent in 2019 [6]. Oil and gas are expected to remain vital energy sources for future generations, due to factors such as population growth [7] and industrialisation [8]. Oil remains the primary fuel for transportation and a crucial feedstock for numerous industrial processes, underpinning its continued importance in the global energy landscape. Moreover, oil and gas reserves offer energy security to many nations and contribute significantly to economic growth and development.

While there is growing interest in renewable energy sources such as solar, wind, and hydroelectric power, the transition away from oil and gas is expected to be gradual

due to the existing infrastructure, economic considerations, and technological limitations.

Alongside a large amount of crude oil consumption, environmental concerns, the finite nature of oil reserves [6] and the growing battle to locate new oil and gas fields are also a cause of uneasiness, as this will devastate future generations. Ideally, future oil recovery methods should centre upon cost-effective production with minimal impact on the environment, most notably via carbon removal, contributing to solving the ever-growing global warming problem.

The application of nanotechnology in the oil and gas industry is an emerging phenomenon, with an increasing number of publications on experiments and simulations on its use in areas such as; drilling [9-11], improved oil recovery [12] and enhanced oil recovery [13-16] as a result of their rheology enhancement and interfacial property alteration. The environmental impact of oil recovery can be limited with the introduction of carbon-based nanofluids, which contribute to both carbon sequestration and an increase in recovery factor, bringing the oil industry steps closer to achieving net-zero greenhouse gas emissions.

Oil recovery is carried out in stages. The primary stage is achieved by the natural pressure depletion in the reservoir, which generally drives about 20% of the original oil in place (OOIP) to the oil well [17]. As the pressure depletes, water is pumped via injection wells into the reservoir to increase the pressure and push the oil to the production well; this is the secondary stage also known as water flooding [18]. At this stage, an incremental recovery of ~30% of OOIP can be achieved from a high-quality reservoir [19]. Representatively, these two stages can recover 30-40% of OOIP [17]. To further recover the remaining 60-70% of OOIP, the tertiary stage also known as the EOR (enhanced oil recovery), is applied, which can recover an additional 10-30% of OOIP at the best-case scenario [19].

The fluid flooding of EOR needs to overcome the flow path formed during water flooding and effectively spread to a large volume of the complicated structured reservoir driving out the oil in a mixture of brine and gas. The flooding fluid should be environmentally friendly and cost-effective. So far, various gases such as CO_2 [20], thermal [21, 22], and chemical [23] solutions have been applied as EOR fluids. Alkaline, surfactant and/or polymers are typical chemicals used to change the interfacial interaction of the flooding fluid to the reservoir rock and reservoir fluids,

and/or as viscosity enhancers to enhance oil recovery. Nanofluids such as SiO_2 [24-26] and TiO_2 [27, 28] have been studied for their use as EOR fluids.

This research project aims to develop nanofluids from abundant and low-cost charcoals as effective EOR flooding fluids. The charcoal is rich in carbon as a by-product of bio-oil processing by pyrolysis. The carbon in the charcoal nanofluid will be sequestrated in the reservoir after flooding, therefore, achieving carbon capture and storage benefiting the environment.

1.2. Research aims and objectives

The primary aim of this research project is to develop nanofluids from abundant and low-cost charcoals and investigate their suitability as effective EOR flooding fluids, as shown in Figure 1.1.

The charcoal produced following the conversion of agricultural, or forestry waste into biofuel or bioenergy via pyrolysis, will be used in this project. The first step will be to; carry out proximate analysis to determine the contents of moisture, volatile matter, fixed carbon, and ash in the samples. Determine the main elemental constituents of the samples (carbon, hydrogen, nitrogen, sulphur, and oxygen, obtained by difference). Determine the charcoal chemical bonds and functionalities using a Fourier Transform infrared (FT-IR) spectrometer. Determine the pH at the point of zero charge.

Once all the analysis has been carried out, 2 types of charcoal samples are chosen and dispersed in di-ionised water to be milled into nanofluids. The size change during milling will be monitored via optical microscopy, scanning electron microscopy and particle size analysis using a DLS (Dynamic Light Scattering).

The charcoal nanofluids will then be characterised towards EOR through viscosity analysis at different concentrations and pH, before being flooded into a laboratory core which will simulate an oil reservoir flooding.

Once the oil is flooded into the core the amount of oil recovered will be measured using a measuring cylinder.

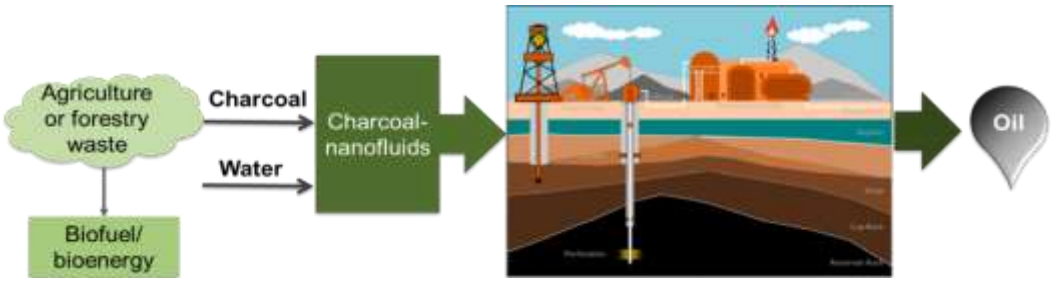

Figure 1.1: illustrates the workflow of the research project, from charcoal selection and nanofluid preparation to oil recovery experiments, highlighting the key stages and objectives of the study. With oil reservoir image from [29].

2. Chapter 2: An In-Depth Literature Review

2.1. Introduction

An oil reservoir, depicted schematically in Figure 2.1, is a subsurface formation containing hydrocarbons, primarily of sedimentary origin. These formations typically consist of heterogeneous porous rock structures, predominantly sandstone, limestone, or dolomite, with interconnected pore spaces that hold oil, water, or gas [8]. The composition and presence of different phases within the reservoir are influenced by factors such as depth, temperature, pressure, composition, and the properties of the surroundings.

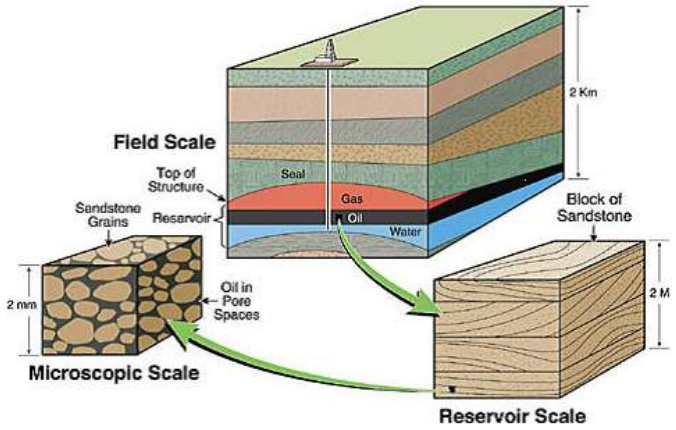

Figure 2.1: A depiction of an oil reservoir [17].

The hydrocarbons such as C_1, C_2, iC_3, nC_4, iC_5, nC_5, C_6, and C_{7+} can be in liquid and/or gaseous phases which are determined by temperatures and pressures [30]. The relationship between the temperature and pressure effects on the hydrocarbon phase can be used to classify different types of reservoirs, which include:

- Undersaturated oil reservoir: the initial reservoir pressure is greater than the bubbling point pressure of the reservoir fluid.
- Saturated oil reservoir: the initial reservoir pressure is equal to the bubbling point pressure of the reservoir fluid.
- Gas-cap reservoir: the initial reservoir pressure is less than the bubbling point pressure of the reservoir fluid.

The complexity of oil reservoirs presents several challenges, including:

- Unpredictability of Pore Space: The nature and shape of pore spaces within the reservoir are often unknown and vary widely, making it challenging to predict fluid flow patterns and distribution.
- Rock Properties: Different types of rock formations, such as sandstone, limestone, and dolomite, can affect fluid behaviour and reservoir characteristics.
- High Temperature: Elevated temperatures within the reservoir can impact fluid properties and increase the complexity of recovery processes.
- Reservoir Salinity: The salinity of reservoir fluids can influence fluid-rock interactions and affect recovery efficiency.
- Reservoir Pressure: Changes in reservoir pressure over time can alter fluid flow dynamics and impact recovery rates.

To recover oil from an oil reservoir, the first stage or primary stage is to drill a hole into the reservoir which uses the formation pressure within the reservoir to push the original oil in place (OOIP) out [31, 32]. The primary recovery method relies solely on the natural energy available in the reservoir to move fluids through the rock formation [33]. The pressure gradient within the reservoir decreases with time which leads to a decrease in the oil recovery rate.

Subsequent stages of oil recovery, namely the secondary and tertiary stages, involve artificial supplementation of natural energy through fluid injection [18], the fluid used for flooding at this stage can either be gas or/and liquid.

The focus of the literature review in this study is on the challenges faced in EOR and the advancements made to address them, beginning with an exploration of the fundamentals of EOR techniques. Understanding these challenges and developments is critical for optimising oil recovery from complex reservoirs.

2.2. Fundamentals of enhanced oil recovery

Following the first two stages of oil recovery, about 40% of the OOIP [19], in a very promising scenario, can be recovered from a high-quality reservoir due to the reality that the OOIP is dispersed in porous oil reservoirs and water flooding results in the formation of water fingers in the porous reservoirs.

Water fingering, also known as viscous fingering, describes the phenomenon of instabilities that arise during the displacement of fluids within porous materials,

particularly in reservoirs. This occurrence often occurs due to variations in viscosity between different phases of fluids within the reservoir [34].

In a porous medium, such as rock formations in an oil reservoir, fluids like water and oil interact and displace each other as they flow through the pores. When there's a significant contrast in viscosity between these fluids, the flow patterns can become unstable, leading to the formation of finger-like structures within the porous medium. For example, if a less viscous fluid (like water) displaces a more viscous fluid (like oil), the less viscous fluid may penetrate deeper into the pore spaces in a finger-like manner, leaving behind channels that are not efficiently swept by the displacing fluid, as shown in Figure 2.2. The water-fingering formation increases the difficulty in recovering the remaining OOIP for the next stage, i.e., the enhanced oil recovery (EOR) stage. Hence, the literature review focuses on the challenges confronting EOR and the developments to combat the challenges, starting with the fundamentals of EOR.

Understanding water fingering is crucial in various applications, especially in the oil and gas industry, where efficient displacement of fluids within reservoirs is essential for maximizing production and recovery rates.

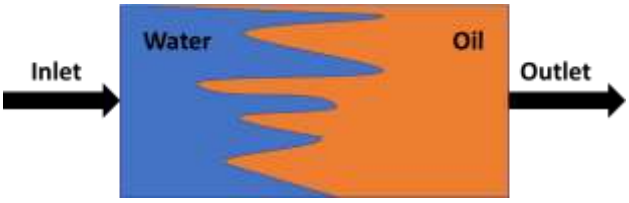

Figure 2.2: Viscous fingering effect: Water finger formation in the reservoir during water flooding.

The parameter of mobility ratio has been developed to describe the relative movement of the oil and flooding fluid in a porous medium. The mobility of a fluid in a porous medium is the ratio of the fluid permeability in the porous medium to its viscosity, as shown in Equation 2.1 [35]. Permeability is the property of a porous medium that depicts the resistance of fluid through it. Permeability is affected by porosity, fluid property, and interaction with the surface of the porous medium. The mobility ratio compares the mobility of the flooding fluid to that of the oil in the same reservoir, as shown in Equation 2.2 [35].

$$\lambda_i = k_i/\mu_i \quad \text{Equation 2.1}$$

$$M = \frac{\lambda_F}{\lambda_O} \quad \text{Equation 2.2}$$

where λ_i is the mobility of fluid phase i, k_i is the relative permeability of fluid phase i (md), and μ_i is the dynamic viscosity of fluid phase I (Pa·s). Flooding fluid mobility is λ_F, the mobility of the Oil λ_O and M is the mobility ratio.

Theoretically, a mobility ratio equal to or less than one is desired to reduce the viscous fingering and improve volumetric spreading efficiency [35, 36]. A large spreading efficiency means the flooding fluids can reach a large volume of the reservoir [37]. By manipulating the properties: of viscosity, interfacial tension of the flooding fluid and/or that of the OOIP, one can create a system in which the injected fluid will be diverted from a higher to lower permeability zone [38]; the flooding fluid will be swept to a large volume of the reservoir, achieving a higher spreading efficiency.

On a microscopic level, the complexity of an oil reservoir originates from not only the heterogeneous porous structure and reservoir fluids but also the mineral content of the reservoir rock. The mineral content varies from one reservoir to another reservoir; these include carbonate minerals, clay minerals, and quartz minerals [39]. The effect of mineral content is highlighted in the rock wettability, as some minerals such as quartz minerals display water-wet properties while others such as carbonate minerals exhibit oil-wet properties, as shown in Figure 2.3 [40]. In oil-wet rock scenarios, the amount of oil trapped within the pore throats, which are the small spaces where two grains meet, is typically lower than in water-wet rock. This discrepancy arises from the heightened affinity between the oil and the rock surface, characterised by a contact angle exceeding 90°. In the case of water-wet rocks, there is an increase in the water film on the rock surface during water injection. The water film leads to the formation of a bridge of water at the connection between pores, trapping oil droplets within the pore, with a contact angle of less than 90° [38]; these properties of the water-wet rock result in a higher overall recovery, which is desirable.

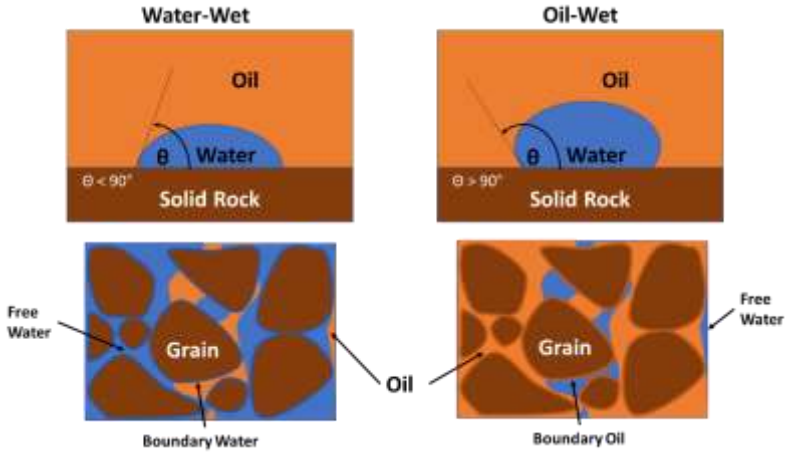

Figure 2.3: Water-Wet and Oil-Wet rocks.

The ions present in reservoir rock minerals can significantly influence the attractive and repulsive nature of the reservoir through various mechanisms: The presence of ions on the surface of mineral grains can create a net electrical charge, resulting in either a positive or negative surface charge. This surface charge affects the interaction between minerals and fluids within the reservoir [41]. For example, clay minerals commonly have negatively charged surfaces due to the presence of ions such as aluminium and silicon [42]. This charge can influence the adsorption of ions and molecules from the reservoir fluids. Some minerals in reservoir rocks, particularly clay minerals, can exchange ions with the reservoir fluids. This ion exchange process can alter the chemical composition and surface charge of the minerals, thereby affecting the interaction between the minerals and the fluids. For instance, the exchange of cations like sodium (Na^+) and calcium (Ca^{2+}) in clay minerals with other cations present in the reservoir fluids can impact fluid-rock interactions [43]. The presence of specific ions can influence the wettability of the reservoir rock surface, determining whether it is water-wet, oil-wet, or intermediate-wet. This, in turn, affects the distribution and movement of fluids within the reservoir. For example, certain ions may promote oil-wet conditions by enhancing the affinity of the rock surface for oil molecules, while others may promote water-wet conditions [31, 40]. Ions in the reservoir fluids can interact with mineral surfaces, leading to the dissolution or precipitation of minerals. This process can alter the pore structure and permeability of the reservoir rock, impacting fluid flow and distribution.

Overall, the presence and behaviour of ions in reservoir rock minerals play a crucial role in determining the attractive and repulsive forces between the rock and reservoir

fluids, influencing fluid flow, distribution, and recovery processes in hydrocarbon reservoirs.

In conclusion, understanding the behaviour of fluids within porous reservoirs and the influence of mineral content is essential for effective Enhanced Oil Recovery. By addressing challenges such as water fingering and considering factors like rock wettability and ion interactions, engineers can develop strategies to improve recovery rates and maximize production efficiency.

2.3. Enhanced oil recovery methods

2.3.1. Thermal methods

Thermal methods depend on the use of thermal energy to reduce the viscosity of the oil present in the reservoir, leading to an increase in the mobility of the oil, and in turn, a reduction in the mobility ratio, making the thermal method more suitable for heavy oils [19, 21]. Steam injection and in situ combustion of the oil in the reservoir are the most commonly used thermal EOR methods [21, 22].

Superheated steam is injected between 300 to 400°C as shown in Figure 2.4; however, the temperature reduces as the superheated steam moves from the steam injector through the reservoir towards the producer, implying the recovery factor of the steam decreases with time [23]. At a depth of 900 m and an initial oil viscosity of 1000 mPa.s, about 55% of OIP (Oil in Place) can be recovered using the steam injection method [23]. The steam used has a lower viscosity than that of water, resulting in breakthrough/ leakage of steam.

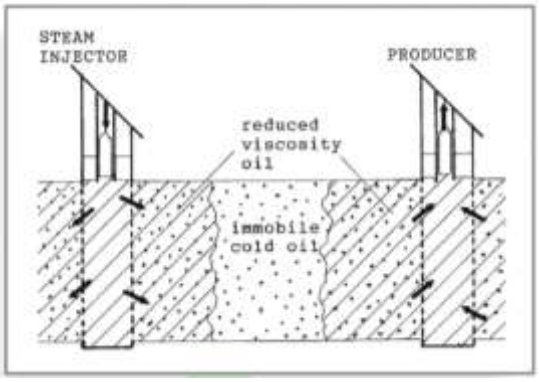

Figure 2.4: An illustration of a thermal method: Superheated steam injection [44].

In situ combustion of the oil is the injection of oxygen or air into the reservoir to promote combustion of a portion of the oil in the reservoir in a controlled manner. It

works by burning 6 to 25% of the oil in the reservoir, generating heat in the temperature range of 200 to 650°C, leading to a reduction in viscosity and an increase in the mobility of the oil [23]. One of the challenges facing this process is the high volume (20 to 250 m^3 per day) and pressure (20 to 90 atm) of oxygen or air required to be used as oxidising agents to initiate and sustain the combustion process. The combustion of the oil within the reservoir typically leads to the production of CO_2 which is a greenhouse gas that contributes to global warming [36].

2.3.2. Gas injection methods

EOR Gas injection methods are the injection of gases such as CO_2 and N_2 to reduce the viscosity and density of oil in the reservoir. This includes immiscible and miscible, and water alternating gas method.

Immiscible gases are injected below the minimum miscibility pressure (MMP), while miscible gases are injected at or above MMP [19]. MMP is the pressure needed to recover 90% of oil using CO_2 [20]. The injection of gases such as N_2 and CO_2, at low pressure, is known as the immiscible method [31]. The gas (N_2 or CO_2) is dissolved in the lighter fraction of the oil, giving rise to the swelling of the oil and reduction in viscosity, both of which improve oil recovery [31].

Miscible gas injection is more efficient than immiscible gas injection, as miscible gas injection improves the microscopic displacement efficiency, thereby reducing the interfacial tension between the oil and the miscible gas [38]. The reduction in interfacial tension leads to the decline of both viscosity and density of the oil, prompting an increase in the oil mobility [31, 38], seeing up to 35% recovery of OOIP with the injection of CO_2 [44]. The gases commonly used for miscible gas injection are CO_2 and N_2 [19, 38]. Due to the retention of gas within the reservoir, the volume of gas for re-injection to maintain reservoir pressure reduces with time [38].

During gas flooding, the gas displaces the oil within the reservoir and can lead to viscosity fingering. To further increase the recovery factor, water is injected following gas in a method known as Water Alternating Gas (WAG) flooding [38]. The CO_2 is first injected through the injection well after which water is pumped into the reservoir which drives the oil towards the production well as shown in Figure 2.5. While the gas lowers the viscosity of the oil, the water slows the movement of the gas, which in turn reduces viscous fingering and increases the displacement spreading efficiency [45]. Although WAG has shown great success in the application as it can result in

about 10 to 20% reduction in the viscosity of the oil, bringing about a recovery of about 7 to 15% of the oil in place [23], there is still an occurrence of gas breakthrough where the CO_2 breakthrough to the production well prematurely, bypassing significant portion of the reservoir and gravity segregation where the less dese injected gas than the reservoir fluids tends to rise vertically within the reservoir, which can contaminate water around the reservoir.

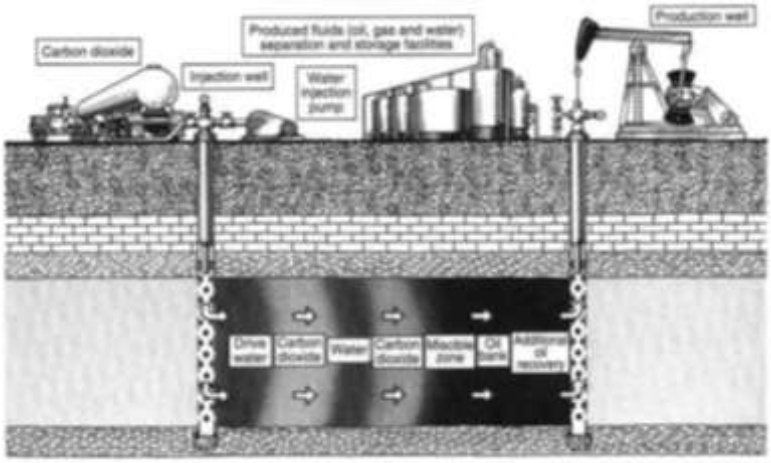

Figure 2.5: An illustration of a CO_2 gas flooding process [46].

2.3.1. Chemical injection

Chemical injection involves the addition of different chemicals to the flooding water [32], thereby decreasing the interfacial tension (IFT) by using alkaline or surfactants between the oil and the flooding fluid or increasing the viscosity of the flooding fluid by utilising polymers, in turn increasing the recovery factor.

Alkaline flooding is the dissolving of chemicals such as sodium hydroxide, sodium carbonate, and sodium silicate in water, making a solution capable of altering the wettability of the rock surface and reducing the interfacial tension between the oil and the flooding fluid [47]. The alkaline reacts with the organic acids present in the oil, leading to the formation of emulsifying surfactant. The surfactants are capable of reducing the interfacial tension between the oil and the flooding fluid. The quantity of organic acid in the oil and the concentration of the alkaline determines the degree of reduction in interfacial tension [21]. The effect of alkaline flooding is highly dependent on the rock formation present in the oil reservoir. For example, rocks with high salt content do not favour a high recovery as it increases interfacial tension between the oil and the flooding fluid. Equally, the presence of clay which is generally chlorite,

illite, kaolinite, smectite and montmorillonite [48] in the reservoir rock can lead to a decrease in pH due to ion exchange at this moment, increasing the interfacial tension. An average of 20% of OIP has been recovered from both pilot and large-scale projects worldwide [23, 49-53]. However, the oil recovered requires further treatments due to elevated pH levels and potential high salinity due to the formation of stable emulsions causing additional costs.

Similar to the behaviour of the surfactant produced during the reaction of alkaline with organic acids, surfactants are adsorbed on the oil/water interface, reducing the interfacial tension [54, 55]. There are different types of surfactants: anionic, non-ionic, and cationic [55]. Anionic surfactants like sulfonates and carboxylates are widely used in sandstone reservoirs, as they perform better in low salinity conditions and can tolerate high temperatures above 60°C [56]. Non-ionic surfactants such as polyoxyethylene and alcohol ethoxylates can withstand high salinity conditions. Still, the hydrogen bonds are weakened at high temperatures, leading to the poor dissolution of the surfactant in water [56]. Field applications of surfactants have reported an increase of 12 to 30% OOIP [57].

Polymer flooding is used in EOR to increase the viscosity of the fluid, which further changes the relative mobility ratio to less than 1 [21, 38]. Typical examples of polymers used are natural xanthan gum and partially hydrolysed polyacrylamide (PHPA) [21, 55]. Polymer flooding has been successfully used for reservoirs with temperatures between 80 to 100°C, low clay content, and oil viscosity between 10 to 150 cP [23], these include Dagang China, where HPAM (Hydrolysed Polyacrylamide) polymer was used, and a recovery of 8.0% was observed. Another example is from Rapdan Canada, where HPAM polymer was also used, and a recovery of 11.0% of OIP, was achieved [23].

Alkaline Surfactant Polymer (ASP) flooding combines the injection of a mixture of alkaline, surfactant, and polymer with water into the oil reservoir. The surfactant reduces the IFT between water and oil while stabilising the emulsion. The alkaline reduces the adsorption of the surfactant onto the pore walls and controls the salinity of the mixture, further decreasing the IFT. Finally, the polymer increases the viscosity, improving the mobility of the flooding fluid [38, 58]. When compared to polymer flooding used in Chinese pilot plants such as Daqing and Shengli, an incremental oil recovery of up to 14.0% of OOIP was obtained for a good quality reservoir using

polymer flooding [59]. In comparison, the implementation of ASP saw an incremental recovery of up to 25.0% of OOIP [60]. Alongside the higher recovery factor, it also increases the well's running lifetime by at least 4 years, meaning the well can produce for a longer duration [61]. However, like every other chemical EOR method, the ASP flooding is expensive with a total cost per barrel of incremental oil is $11 to $15 [62].

2.4. Nanofluids in EOR

Nanofluids are defined as fluids with nanometre-sized solid particles or nanoparticles [63] which are in the range of 1-100 nm [64]. A variety of research into nanoparticles has realised their potentiality as a sustainable flooding fluid. Nanoparticles can be categorised by their differing chemical properties and material morphology.

Nanofluids of various metal oxides such as SiO_2 [24-26] and TiO_2 [27, 28], Al_2O_3 [27, 28, 65] and Fe_2O_3 [65, 66] have been examined for their performance in enhanced oil recovery and have demonstrated an oil recovery capacity of 8-16% of the original oil in place (OOIP) after water flooding [28, 67, 68] for SiO_2, Al_2O_3 and TiO_2. The research described in the literature covers the effect of nanoparticle composition, concentration, and other properties such as size distribution, shape, porosity and surface chemistry on the viscosity, wettability of the flooding fluid and enhanced oil recovery.

Youssif et al. (2018) [69] studied the oil recovery performance of porous silica nanofluids. The SiO_2 nanoparticles studied had a monomodal size distribution, averaged at 22 nm, and a specific area of 370 m^2/g. The nanofluids in 3 wt% of NaCl aqueous solution were used to recover the oil loaded in sandstone cores, and the results showed that the oil recovered firstly increased with the silica concentration and reached the maximum oil recovery capacity of 53.1% of the OOIP at a SiO_2 concentration of 0.1 wt%. At this concentration, a further 13.0% of the OOIP is recovered after the water flooding or 12.0% more of the OOIP is recovered compared to water flooding alone. The SiO_2 nanofluid of 0.1 wt% was determined to have a viscosity of 1.2 mPa.s.

Table 2.1 presents the results of various nanofluid flooding experiments, illustrating the potential of nanofluids to enhance oil recovery percentages. The table underscores the impact of factors such as concentration, base fluid, and temperature on nanofluid behaviour as a flooding fluid. Oil recovery in reservoirs is influenced by

the viscosity of the flooding fluid and interfacial properties, necessitating an understanding of how nanoparticle addition affects these properties.

The data in Table 2.1 reveals that the efficacy of EOR nanofluids varies depending on the base fluid and nanoparticle type. For instance, Al_2O_3 nanoparticles dispersed in surfactants yielded oil recovery rates of up to 53.5% of Original Oil in Place (OOIP) [70], whereas those dispersed in water resulted in recovery rates of up to 16.0% of OOIP [25]. It's noteworthy that much of the research on nanofluids in EOR focuses on metal oxides.

Several researchers have studied the potential of titanium oxide (TiO_2) nanoparticles for enhanced oil recovery. Ehtesabi et al. (2014) [71] looked at the use of nanoparticles of a TiO_2 diameter of approximately 60 nm dispersed in different salinity, for the reduction of the oil-brine IFT in heavy oil. It was found that when the nanoparticles were added to the water it did not have any significant effect on the viscosity. However, the contact angle measurements showed that nanoparticle sedimentation altered the wettability of the surface, with a reduction in contact angle from 125 ± 3° to 90 ± 3° (i.e., from oil-wet to water-wet). The change in wettability increased oil recovery when the core flooding in sandstone was carried out. This research showed the importance of nanoparticle concentration. Following water flooding, only 49.0% of the oil was recovered, and the injection of TiO_2 in 5000 ppm brine at a concentration of 0.01% saw an improvement of 80.0%. In comparison, the injection of 1.0% TiO_2 saw a recovery of 42.0%. In another study, Ehtesabi et al. (2015) [72], using a lower concentration of TiO_2, stated that manipulation of wettability of the rock surface from oil-wet to water-wet due to the deposition of TiO_2 nanoparticles was a vital method for increasing oil flooding.

William et al. [73] studied the use of Copper Oxide (CuO) and Zinc Oxide (ZnO) nanofluids in xanthan gum. CuO and ZnO particles of diameter less than 50 nm, were dispersed in a xanthan gum aqueous solution as a base fluid at concentrations of 0.1 to 0.5 wt%, while 1.0 vol% of the prepared liquid was added to water. The rheology of the nanofluid was studied at different temperatures (25 to 110 °C) and pressures (0.1 mPa and 10.0 mPa). It was observed that an increase in temperature stemmed in a decrease in the viscosity of the fluid, because of thermal expansion, while increasing pressure heightened the viscosity due to compression. Where it was found

that the viscosity at a higher pressure of 10.0 mPa was much lower than at 0.1 mPa, shear-thinning characteristics were observed.

One of the most commonly used nanoparticles in enhanced oil recovery is silica nanoparticles (SiNPs) [69]. This can be attributed to their environmentally friendly nature, cheapness, and ease of manipulation, and is the main composition of sandstone reservoirs.

Along with the physical morphology, nanoparticle surface treatment formulated with a very small number of surface-active agents or polymers, changes the nanoparticle surface chemistry and wettability to the reservoir rock, and the influence of such modifications on SiO_2 nanoparticle performance has been investigated. Azarshin et al. (2017) [74] modified silica nanoparticles (10-15 nm) surface with amine ((3-Aminopropyl) triethoxysilane) to improve the performance of water flooding in oil-wet reservoirs (carbonate cores). Core flood tests of 0.25 wt% of the amine-functionalised silica nanofluid showed a paramount increase of 18.0% in total oil recovery compared to that of the nanoparticles without surface modification, thus amounting to an impressive 28.0% increase compared to water flooding alone.

Carbon nanotubes are a group of carbon-based materials that have a hollow cylindrical morphology in the low nanometre range. They are a different type of nanomaterials in terms of composition and morphology compared to metal oxide nanoparticles, and it is thus of interest to investigate their performance in enhanced oil recovery. Alnarabiji et al. (2016) [75] examined the performance of nanofluids of multiwall carbon nanotubes (MWCNT) in enhanced oil recovery. Their research showed that the nanofluid of 0.05 wt% MWCNT gave an impressive recovery efficiency of 31.8% of the residual oil in place (ROIP).

Cellulose nanoparticles are gaining interest from researchers due to their sustainability, biodegradability, nontoxicity, and EOR activity. Agi et al. [76] used ascorbic acid extracted from plants and fruits to synthesise cellulose nanoparticles (CNP) (117 nm), by using nanoprecipitation and hydrolysis-assisted ultrasonic methods. The zeta potential result (-36.8 mV) showed that cellulose nanofluid (CNF) was stable. The oil recovery after water flooding was 48.0% of OOIP, following the injection of CNF 20.0% of OOIP was recovered. The use of 0.5-2.0 wt% cellulose nanocrystals (CNC) of length 130 nm and width 5.9 nm dispersed in water for core flooding in sandstone was studied by Molnes et al. [77]. The nanofluid was stable

with a zeta potential of -49.4 mV, which showed that CNC could be used as both salt stability and flooding fluid into a core medium.

Overall, nanofluids offer a versatile and potentially effective approach to enhance oil recovery in reservoirs, with ongoing research focusing on optimising nanoparticle properties and understanding their interactions with reservoir fluids and rock formations.

Table 2.1: Recovery of OOIP Percentage with Nanoparticle Types in Varied Base Fluids, Concentrations, Temperatures, and Rock Types

Nanoparticle Type	Base Fluid	Nanoparticle Concentration (wt %)	Temp (°C)	Rock Type	Recovery % of OOIP	Ref
SiO_2	Sodium dodecyl sulphate (Surfactant)	-	35	Sand pack	20	[24]
	Water	0.1	-	Sandstone	16	[25]
	Hydrolysed Polyacrylamides (HPAM)	-	80	Quartz Sand	10.54	[26]
	polyacrylamide grafted silica particle (PAAGS)	2.5	-	Quartz Sand	21	[78]
	Polyacrylamide (SHPAM)	-	82.3	Sandstone	20	[79]

Table 2.1 continues: Recovery of OOIP Percentage with Nanoparticle Types in Varied Base Fluids, Concentrations, Temperatures, and Rock Types

Nanoparticle Type	Base Fluid	Nanoparticle Concentration (wt %)	Temp (^{o}C)	Rock Type	Recovery % of OOIP	Ref
Modified Clay Nanoparticles	HPAM	0.1	-	Carbonate	33	[80]
Al_2O_3	Brine (NaCl)	0.05	-	Sandstone	8	[27]
	Deionised water	0.005	60	Limestone	9.9	[28]
	Propanol	0.15	-	Sandstone	20.2	[65]
	Deionised water + Sodium Dodecyl Sulphate	0.05	-	Glass bead	53.53	[70]

Table 2.1 continues: Recovery of OOIP Percentage with Nanoparticle Types in Varied Base Fluids, Concentrations, Temperatures, and Rock Types

Nanoparticle Type	Base Fluid	Nanoparticle Concentration (wt %)	Temp (°C)	Rock Type	Recovery % of OOIP	Ref
Fe_2O_3	Propanol	0.15	-	Sandstone	17.3	[65]
	Distilled water	0.3	-	Sand	9.2	[81]
	Deionised water	0.01	-	Glass bead	38	[66]
TiO_2	Brine (NaCl)	0.05	-	Sandstone	11	[27]
	Deionised water	0.005	60	Limestone	6.6	[28]

2.5. Viscosity of nanofluids

Viscosity is a property of rheological behaviour presented when an area of fluid is subjected to an external force. In 1687 Sir Isaac Newton [82], defined the relationship between shear stress (mPa) and shear rate (1/s) of a fluid as a constant known as viscosity (mPa.s), as shown in Equation 2.3. Viscosity property varies with the composition, temperature, and pressure of the fluid, making it a thermophysical property.

$$\sigma = \mu \times \dot{\gamma} \quad \text{Equation 2.3}$$

where σ denotes the shear stress (mPa), μ signifies the viscosity (mPa.s) and $\dot{\gamma}$ indicate the shear rate (1/s).

Fluids which are independent of the shear rate and viscosity are known as Newtonian fluids, meaning they obey the Newton equation shown in Equation 2.3. While fluids that display a varying viscosity with the shear rate, or a non-linear correlation between the shear rate and shear stress, in the form of shear thickening or shear thinning, are classified as non-Newtonian, as shown in Figure 2.6 [83].

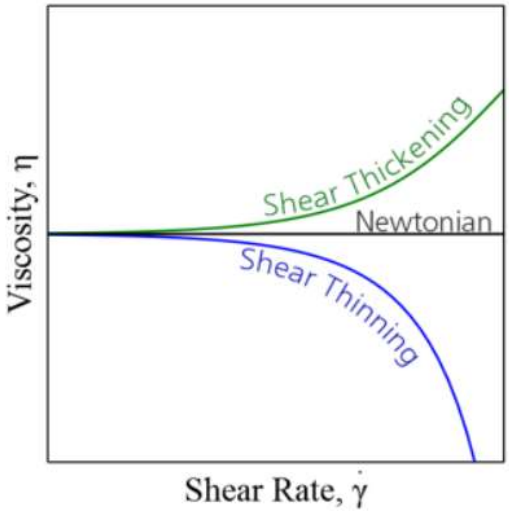

Figure 2.6: Viscosity vs shear rate of Newtonian and non-Newtonian fluids [84].

The viscosity of a liquid is a constant that reflects the liquid's intermolecular interaction. Some fluids have higher viscosity due to more vital molecular interactions, while others have a lower viscosity due to weaker molecular interactions. Enhancement of viscosity requires an understanding of the effects of thermophysical

properties on shear rate and shear stress, which will be discussed in the next sections.

2.5.1. Viscosity model for nanofluids

The viscosity enhancement is evaluated by relative viscosity, i.e., the viscosity ratio of the nanofluid to the base liquid. It increases with the particle volume fraction, as described by the equations reported in [85-88]. These equations incorporate molecule-to-molecule interactions mediated by the viscosity of the base fluid but do not include interactions of solvated molecules to nanoparticles, nor nanoparticle-to-nanoparticle interactions. The nanoparticle volume fraction expressed in Equations 2.4-2.10 is described for spherical particles without the inclusion of any parameters that distinguish particle size, shape, and composition of the particles (e.g. surface chemistry). However, the effect of particle properties on the viscosity enhancement can be very significant, as has been demonstrated by the studies of particle size [89-92], shape, i.e., morphology [93, 94], material type, i.e. chemical composition [95] concerning nanoparticle concentration [89, 90, 95-98]. Unexplained phenomena such as the relative viscosity decreasing with particle size reduction towards the lower nanometre range [99, 100] and inconsistency in experimental data from different laboratories [101-104] have been repeatedly observed. For example, various groups studied TiO_2 aqueous nanofluids with a nanoparticle volume fraction of 0.02. For TiO_2 nanoparticles of 21 nm [101] determined a relative viscosity of 1.1, whereas [102] reported a value of 1.6 at the same temperature of 25°C. The origin of this discrepancy is unclear. It is even more puzzling that at the volume fraction of 0.02 for an aqueous nanofluid of TiO_2 nanoparticles of 90-200 nm, Jarahnejad et al. [99] reported a relative viscosity of 1.9. Similarly enigmatic results have been reported for Al_2O_3 aqueous nanofluids, in that at a volume fraction of 0.03, Duan et al. [100] reported a relative viscosity of 1.5 for 25 nm Al_2O_3 nanoparticles, whereas Chandrasekar et al. [103] reported a relative viscosity of 1.5 for 43 nm Al_2O_3 nanoparticles, and Moldoveanu et al. (2018) [104] reported a relative viscosity of 3.0 for 45 nm Al_2O_3 nanoparticles. There is a definite need to explain these as yet inexplicable experimental results to get insight into other factors, beyond the nanoparticle volume ratio and nanoparticle size, that affect the magnitude of viscosity enhancement.

The comparison of these various reported experimental results with the calculated values resulting from the different theoretical treatments shows that the theoretical equations of [85-87, 105], all give values for the relative viscosity of nanofluids that are significantly lower than the experimental ones, while the calculated values resulting from the empirical equation by Pak and Cho [88] represent the upper limit in the nanoparticle concentration range for which Pak and Cho's empirical equation is derived. The values of the literature data that are located between the values calculated using the treatments by Einstein or Pak and Cho cannot be explained. Chen and co-authors [106] modified the Krieger-Dougherty equation by introducing an agglomeration ratio parameter to describe the particles' agglomeration in the dispersion, but the modelling result leads to the explanation that the viscosity enhancement increases with the agglomeration ratio, which does not obey the general understanding of dispersion systems and or guide the relevant practice work.

Various theories have been developed to explain and predict the influence of particle addition on fluid viscosity. The first attempt has been reported by Einstein as early as 1906 [85]. Equation 2.4 shows the Einstein equation, which expresses the ratio of the effective dynamic viscosity of the nanofluid (η_{eff}) and the dynamic viscosity of the base liquid (also termed base fluid, abbreviated as bf) (η_{bf}) at a particular temperature as being equal to 1 + 2.5 φ, in which φ is the volume fraction of the spherical nanoparticles suspended in the base liquid.

$$\frac{\eta_{\mathrm{eff}}}{\eta_{\mathrm{bf}}} = (1 + 2.5\varphi) \qquad \text{Equation 2.4}$$

The Einstein equation is valid for dilute suspensions with a nanoparticle volume fraction less than 0.01, hence its limitation is that it does not consider the interaction between hard-spherical particles in the suspension.

In 1952, Brinkman [105] expanded on Einstein's treatment by estimating the concentration-dependence of any particle quantity at higher concentrations if the result for infinite dilution is known, which resulted in Equation 2.5 which is valid for a particle volume fraction of up to 0.04.

$$\frac{\eta_{\mathrm{eff}}}{\eta_{\mathrm{bf}}} = \frac{1}{(1-\varphi)^{2.5}} \qquad \text{Equation 2.5}$$

When the volume fraction of suspended solid particles increases further, the interaction among the particles increases due to Brownian motion. In 1977, Batchelor

[86] modified Einstein's equation by including the effect of Brownian motion of spherical hard particles for an isotropic suspension, thus resulting in Equation 2.6, which is suitable for predicting the suspension viscosity for particle volume fractions of up to 0.1.

$$\frac{\eta_{\mathrm{eff}}}{\eta_{\mathrm{bf}}} = 1 + 2.5\varphi + 6.2\varphi^2 \qquad \text{Equation 2,6}$$

In 1998, Pak and Cho [88] specified Equation 2.7, resulting from experimental data of aqueous suspensions of γ-Al_2O_3 and TiO_2 nanoparticles, which has a similar form to that of Batchelor, but the constants involved are much larger.

$$\frac{\eta_{eff}}{\eta_{bf}} = 1 + 39.11\varphi + 533.9\varphi^2 \qquad \text{Equation 2.7}$$

Building on the equations related to Einstein's model, [87] introduced their power law-based equation in 1959, Equation 2.8, which predicts the effect of the volume fraction of micro/millimetre-sized particles in suspensions on the relative viscosity. It predicts the viscosity of non-diluted suspensions with randomly monodispersed hard spherical particles by introducing the maximum particle volumetric fraction (φ_m), at which the particles are just able to flow.

$$\frac{\eta_{\mathrm{eff}}}{\eta_{\mathrm{bf}}} = \left(1 - \frac{\varphi}{\varphi_{\mathrm{m}}}\right)^{-[\eta]\varphi_{\mathrm{m}}} \qquad \text{Equation 2.8}$$

$$where\ [\eta] = \lim_{\varphi \to 0} \frac{\eta - \eta_0}{\eta_0 \varphi}$$

The maximum particle volume fraction φ_m varies from 0.50 to 0.54 under quiescent conditions, while at high shear rates, the value is approximately 0.61. [η] is the intrinsic viscosity (the measure of a solute's contribution to the viscosity of a solution) which is 2.5 according to Einstein [85], for well-dispersed hard spherical particles [83].

In 2007, Chen et al. [106] modified the Krieger-Dougherty equation by introducing φ_a, the volume fraction of aggregation, to address the particles' aggregation as shown in Equation 2.9.

$$\frac{\eta_{\mathrm{eff}}}{\eta_{\mathrm{bf}}} = \left(1 - \frac{\varphi_a}{\varphi_{\mathrm{m}}}\right)^{-[\eta]\varphi_{\mathrm{m}}} \qquad \text{Equation 2.9}$$

here $\varphi_a = \varphi\left(\frac{a_a}{a}\right)^{3-D}$, in which a_a and a are the radius of aggregate and the radius of the primary particle, respectively, and D is the fractal index indicating the extent of change in the packing fraction from the centre to the edge of the aggregate. It is typically 1.6-2.5 for diffusion-limited aggregation and 2.0-2.2 for rate-limited aggregation for spherical particles [107-109]

For spherical particles with D = 1.8 [110], [η] = 2.5 and φ_{m}= 0.605 [111], Equation 2.10.

$$\frac{\eta_{\mathrm{eff}}}{\eta_{\mathrm{bf}}} = \left(1 - \frac{\varphi}{0.605}\left(\frac{a_a}{a}\right)^{1.2}\right)^{-1.5125} \qquad \text{Equation 2.10}$$

Moving forward, Chapters 4 and 6 promise deeper insights into the impact of viscosity on nanofluids, enriching our understanding of these fascinating materials.

Table 2.2: Effects of Nanoparticle Type, Base Fluid, Concentration, Particle Size, and Shear Rate on Nanofluid Rheology: Literature Review.

Nanoparticle Type	Base Fluid	NP Con.	Temp. (ºC)	Particle size (nm)	Shear rate range (s^{-1})	Comment	Ref
SiO_2 (Spherical)	Water	0.45-4 vol%	20-50	12	-	• Decrease in viscosity with an increase in temperature, from 4.5 mPa.s at 20ºC to 2.7 mPa.s at 50ºC (4 vol%)	[90]
TiO_2 (Spherical) Pristine-MWCNT (Rod) Functionalised-MWCNTs (Rod) MWCNT-TiO_2 (Rod)	Water	0.125-0.5 wt%	25-70	21-45 nm Dia=40-60 nm length=5-15µm	0-300	• All samples displayed an increase in viscosity with an increase in concentration and a decrease in viscosity with an increase in temperature. • A shear-thickening behaviour was observed for TiO_2. • Shear-thinning was observed for both pristine-MWCNT and functionalised-MWCNT. • The acid treatment of functionalised MWCNT destroyed the graphene structure, which led to a reduction in viscosity. • Shear-thickening behaviour observed for MWCNT-TiO_2. Reduction in viscosity with an increase in TiO_2 concentration due to the prolonged treatment destroying graphene structure. • Pristine-MWCNT displayed the highest viscosity enhancement (~1300%) of all samples at 25ºC and a concentration of 0.5 wt%.	[95]

Table 2.2 continues Effects of Nanoparticle Type, Base Fluid, Concentration, Particle Size, and Shear Rate on Nanofluid Rheology: Literature Review.

Nanoparticle Type	Base Fluid	NP Con.	Temp. (ºC)	Particle size (nm)	Shear rate range (s^{-1})	Comment	Ref
MWCNTs (Rod)	Cationic Chitosan Surfactant (0.1-0.5 wt%) + Deionised water	0.5-3 wt%	-	20-30 (OD) 5-10 (ID) 10-30 μm (length)	1-200	• Addition of 0.1 wt% Chitosan to the deionised water increases the viscosity to about 5 mPa.s, while 0.2 wt% increased it to 10 mPa.s • Shear-thinning behaviour was observed with the addition of MWCNTs. • An increase in viscosity with concentration was observed, with the highest viscosity (180 mPa.s) at 3 wt% MWCNT and 0.2 wt% chitosan	[97]

Table 2.2 continues Effects of Nanoparticle Type, Base Fluid, Concentration, Particle Size, and Shear Rate on Nanofluid Rheology: Literature Review.

TiO_2 (Rod)	DIW	0.5-2.5 wt%	25-50	260 nm	1 -1000	• Shear-thinning behaviour was observed for all concentrations. • An increase in viscosity with an increase in concentration and a decrease in viscosity with an increase in temperature. • The highest enhancement (4.7 mPa.s) was observed at 25ºC, 2.5 wt%. • Higher viscosity than that of spherical nanoparticles.	[98]

2.6. Interfacial performance of nanofluids

The interfacial performance of a liquid is the accumulation of energy and imbalance force at the interface of two phases [112]. Interaction between two liquid phases can be analysed using the interfacial tension, the interface between a liquid and air is studied using surface tension, and the interaction of a liquid with a solid is assessed using the contact angle [113, 114]. The difference between the surface tension of two liquids can be defined as the interfacial tension, as shown in Equation 2.11.

$$\sigma_{l_1 a} - \sigma_{l_2 a} = \sigma_{l_1 l_2} \quad \text{Equation 2.11}$$

where σ_{la} is the liquid-air surface tension (mN/m), $1\ and\ 2$ represents the different liquids, and $\sigma_{l_1 l_2}$is the liquid-liquid interfacial tension (mN/m).

In oil recovery, the flooding fluid simultaneously interacts with both the liquids in the reservoir and the rock. Although the interfacial properties of the liquids and the rock within the reservoir cannot be altered, that of the flooding fluid can be manipulated. Hence, the primary purpose of this section is to review the methods of determining the interfacial performance and the parameters that impact the interfacial tension and wettability of nanofluids.

2.6.1. Interfacial performance measurement

A variety of techniques have been used to measure the interfacial performance of liquids and can be applied to nanofluids. The techniques can be grouped into direct measurements, analysis of the balance between capillary and gravity forces, and analysis of gravity-distorted drops [115].

Direct measurements involve the direct contact between a probe and the interface, which leads to an increase in the interfacial area, and an increase in the force pulling the probe due to capillary force [115]. The main techniques that are generally used in this group are the Wilhelmy plate and Du Nouy ring depicted in Figure 2.7. Perfect wettability (cos θ =1) is required for these methods. At the same time, the adsorption of organic compounds from laboratory or test solutions onto the plate/ring can be a significant source of experimental error in this technique.

The capillary effect which is in Figure 2.7 can be used to measure the interfacial tension due to the pressure difference that arises when a decrease in interface

occurs, leading to the increase in the pressure difference between the fluids, with higher pressure on the concave side of the interface [115].

Gravitational force measurement which is in Figure 2.7 is based on drop volume or weight measurements. Although the method is simple, it is sensitive to vibration, which can distort the results. The use of gravity-distorted drop methods for the measurement of interfacial tension is appealing to researchers as it does not require advanced instrumentation. The main method used in this group is the pendant drop method.

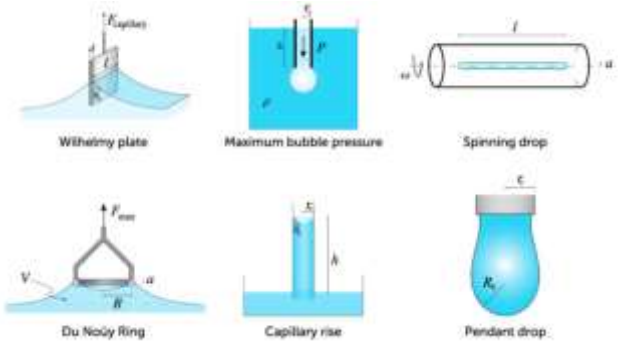

Figure 2.7: Techniques used for IFT and ST measurements. As illustrated in [116].

The pendant drop method requires precise equipment for good quality and reproducible results, which is why stainless steel or glass needles of less than 0.5 diameters are commonly used, as they are easy to clean [117].

The measurement of the contact angle is generally used to determine the wettability of a liquid onto a solid. It can be related to the interfacial energy via Equation 2.12.

$$\sigma_{oa} - \sigma_{wa} = \sigma_{ow} \cos\theta \qquad \text{Equation 2.12}$$

where σ_{os} is the surface tension between oil and air (mN/m), σ_{ws} is the surface tension between water and air (mN/m), σ_{ow} is the interfacial tension between oil and water (mN/m), theta is the contact angle at oil-water-solid interface measured through the water phase.

As shown above, several methods for determining the interfacial tension have been widely explored.

2.6.2. Effect of concentration on Interfacial properties

Chinnam et al. [114], examined the effect of concentration (0-6 vol%) and particle size (15-50 nm) on propylene glycol (60.0%) and water (40.0%) based nanofluids, with ZnO, TiO_2, SiO_2, and Al_2O_3 nanoparticles. It was observed that an increase in nanoparticle concentration generally resulted in a decrease in surface tension, as shown in Figure 2.8. Implies a reduction in the overall interfacial tension between the nanofluid and oil, with the interfacial tension reducing with concentration from about 20.9 mN/m for SiO_2 20 nm 1 vol% to 19.6 mN/m for 4 vol% at 50°C. A general reduction in interfacial tension with the addition of nanoparticles was observed, with an initial interfacial tension of 25.5 mN/m at the same base fluid temperature. At lower particle concentrations, that the particles have little to no effect on the surface tension due to the large distance between the particle and the liquid/gas interface.

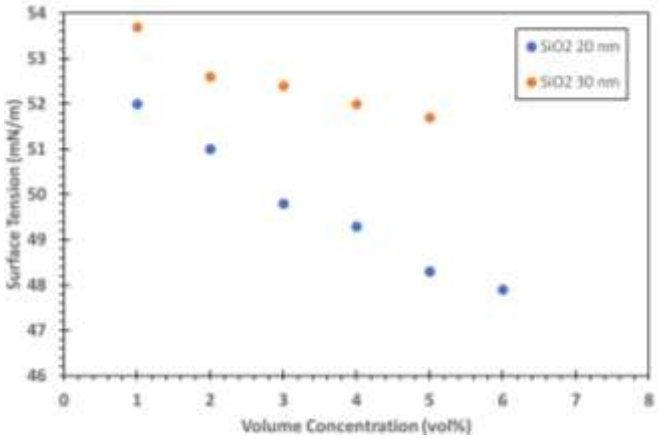

Figure 2.8: Surface tension of SiO_2 nanofluids at 50°C with an increase in concentration.

Golubovic et al. [118], on the other hand, observe little difference in the interfacial tension with the addition of Al_2O_3 (46 and 38 nm) to water. However, the contact angle test carried out by Golubovic et al. [118], showed a reduction from 90° with water, to about 47° with the presence of 0.00257 g/L Al_2O_3 and an additional decrease to 33° with the addition of 0.00646 g/L Al_2O_3, both 46 nm on to a heater wire, as shown in Figure 2.9. The impact of concentration on the wettability of the nanofluid indicates a concentration threshold beyond which the effect on the contact angle becomes negligible.

Then again, Harikrishnan et al. [105] observed an increase in interfacial tension with the addition of Bi_2O_3 (0.5 wt% and 20 nm) and CuO (0.5 wt% and 30 nm)

nanoparticles to water and glycerol and a reduction in surface contact angle with the addition to ethylene glycol. The results show that the base fluid plays a vital role in the interfacial performance of the nanofluid.

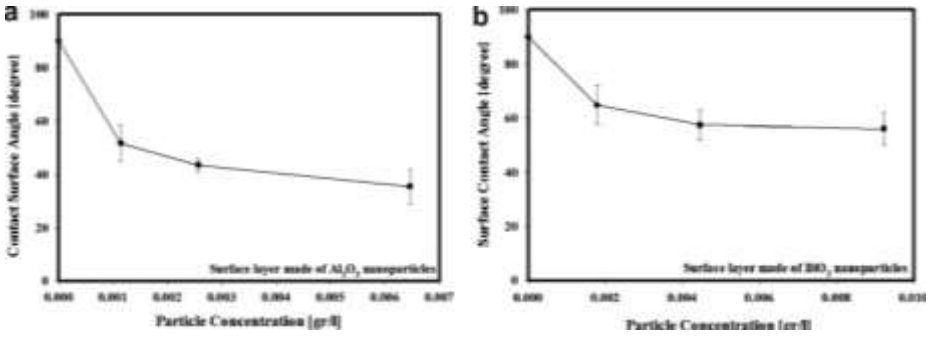

Figure 2.9: a) Contact angle with concentration of Al_2O_3 nanoparticles. b) Contact angle with concentration of BiO_2 nanoparticles.

The size of the nanoparticle also affects the interfacial behaviour of the nanofluid. Bhuiyan et al. [119] examined the effect of Al_2O_3 (13 and 50 nm), and SiO_2 (5-15 and 10-20 nm) nanoparticles dispersed in the water on the surface tension at 30°C. at a nanoparticle concentration of 0.25 vol % a reduction of surface tension from about 72.6 mNm^{-1} to 72.3 mNm^{-1} for Al_2O_3 50 and 13 nm respectively. SiO_2 had a reduction from about 72.2 mNm^{-1} to 71.1 mNm^{-1} for 10-20 and 5-15 nm respectively.

The observed reduction in surface tension can be attributed to several factors. Smaller nanoparticles tend to have a higher surface charge density compared to larger nanoparticles in the base fluids. This results in increased electrostatic repulsion forces between the nanoparticles and the liquid molecules, enhancing adsorption at the interface and thereby reducing surface tension. Additionally, smaller particles possess a larger surface area, leading to higher surface free energy, which further contributes to the decrease in surface tension of the nanofluids.

Overall, the study highlights how the size of nanoparticles influences their interaction with the liquid medium and subsequently affects the surface tension of nanofluids.

2.6.3. Effect of temperature on interfacial tension

The study conducted by Chinnam et al. [114]. investigated the impact of temperature on the interfacial tension of nanofluids composed of propylene glycol (60.0%) and water (40.0%) with ZnO and TiO_2 nanoparticles. Across the temperature range of 30 to 70°C, notable variations in surface tension were observed.

For instance, with TiO_2 nanoparticles at 1.5 vol% and 15 nm size, the surface tension decreased from approximately 54 mNm^{-1} at 30°C to about 48 mNm^{-1} at 67°C. Similarly, with ZnO nanoparticles at 4.0 vol% and 36 nm size, the surface tension decreased from around 53 mNm^{-1} at 30°C to about 49 mNm^{-1} at 65°C.

The decrease in surface tension with increasing temperature can be attributed to the rise in thermal energy within the system. This heightened thermal energy causes both nanoparticles and fluid molecules to exhibit more vigorous vibrations, thereby increasing Brownian motion. Consequently, the enhanced Brownian motion weakens the cohesive forces between molecules at the liquid surface, leading to a reduction in surface tension.

This finding underscores the significant influence of temperature on the interfacial properties of nanofluids and highlights the importance of considering temperature effects in the design and application of nanofluid-based systems.

This section has demonstrated how nanoparticles can effectively modify wettability, decrease interfacial tension, and enhance viscosity when introduced into a fluid. Moreover, it has underscored the critical factors influencing these characteristics, encompassing concentration, particle size, particle shape, base fluid composition, and temperature.

With this understanding, the subsequent step involves leveraging this knowledge to develop and formulate charcoal-based nanofluids for utilisation as flooding fluid in our research endeavours.

2.7. Biomass and Charcoals

Biomasses are complex organic or inorganic solid products that can be classified into woody, agricultural, algae, human and animal waste [120]. Biomass is mostly woody and is derived from trees and forestry wastes made up of stems, branches, leaves, and chips [121]. Agricultural biomass follows, comprising residues from crops and plants such as corn stover, corncobs, rice husks, and wheat straw [121]. The uses of agricultural plants and products for biofuels brings up the concern regarding food vs energy. Hence, this project will focus on the use of agricultural/forestry waste.

Biomass is formed of cells as shown in Figure 2.10 [122], which contain the elements that give them their properties. The cells are made up of three main polymers:

cellulose, hemicellulose, and lignin [123]. Cellulose, the main component, consists of polysaccharides as cellulose contains several sugar molecules bonded together, such as homogeneous β-1 and 4-glycosidic bonds [124]. Hemicellulose is the second-largest component in the plant cell wall. Hemicellulose is a group of complex polysaccharides, also known as heteropolysaccharides [124], Hemicellulose is a collection of sugar molecules such as glucose, mannose, and xylose [123]. Lignin is generally composed of three benzene propane monomers (coniferyl alcohol, sinapyl alcohol, and p-coumaryl alcohol) with a three-dimensional network polymer built through C-C bonds and ether linkage bonds [124]. Typically, cellulose comprises of 35-50 wt%, hemicellulose 20-35 wt%, and lignin 10-25 wt% as shown in Table 2.3 [125].

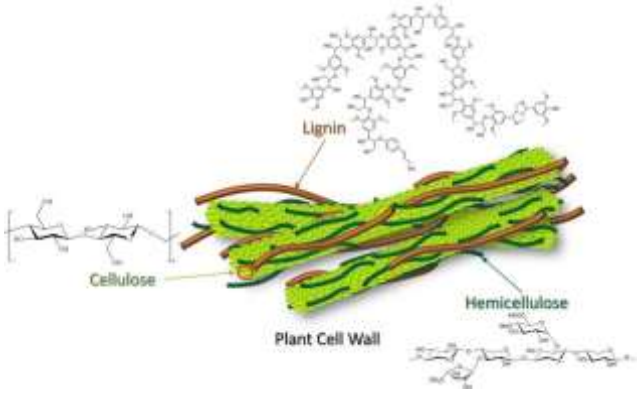

Figure 2.10: Structure of Biomass showing the cellulose, lignin and hemicellulose.

Table 2.3: Cellulose, Hemicellulose and Lignin composition of woody and agricultural biomass (dry basis) [125].

General Biomass Classification	Lignocellulose Biomass Type	Cellulose (wt %)	Hemicellulose (wt %)	Lignin (wt %)
Hardwood	Oak	40.4	35.9	24.1
Softwood	Pine	42.0-50.0	24.0-27.0	20.0
Agricultural Waste	Rice Husk	28.7-35.6	12.0-29.3	15.4-20.0
Agricultural Waste	Wheat Straw	35.0-39.0	23.0-30.0	12.0.16.0
Grasses	Switchgrass	35.0-40.0	25.0-30.0	15.0-20.0

Different biomasses have varying compositions; the composition of each material is different due to the structure of the hemicellulose, cellulose, lignin, and the

composition of inorganic and organic materials [126]. An experiment calculating the combustion properties of selected biomass was carried out by Jenkins et al. [126]. As shown in Table 2.4, dry matter in biomass is typically made of 30 to 40 wt% oxygen. Depending on the ash content of the biomass, carbon accounts for 30 to 60 wt%, and the number of inorganic ions such as Ca, K, Mg, Na, P, Cl, Si, and S is also dependent on the ash content. Inorganic ions such as Na, K, Ca, and Mg in the ash affect the alkalinity of the ash as they are known as alkali and alkaline earth minerals, which will affect the behaviour of the charcoal nanofluid produced as a flooding fluid. To determine the moisture, volatile matter, ash, and fixed carbon content, proximate analysis is carried out, while ultimate analysis is performed to determine the elemental compositions such as C, H, N, S, and O. For example in Table 2.4 it can be seen that the ash content of willow wood is lower at 1.7 wt% dry basis and that of rice hulls are higher at about 20.3 wt% dry basis.

Table 2.4: Proximate, Ultimate, and Elemental analysis of woody and agricultural biomass (dry basis wt %) [126].

	Wheat Straw	Rice Hulls	Rice Straw	Willow Wood
Proximate Analysis				
Fixed Carbon	17.71	16.22	15.86	16.07
Volatile Matter	75.27	63.52	65.47	82.22
Ash	7.02	20.26	18.67	1.71
Ultimate Analysis				
Carbon	44.92	38.83	38.24	49.90
Hydrogen	5.46	4.75	5.20	5.90
Oxygen (Diff)	41.77	35.47	36.26	41.60
Nitrogen	0.44	0.52	0.87	0.61
Sulphur	0.16	0.05	0.18	0.07
Chlorine	0.23	0.12	0.58	<0.01

Table 2.4 continues the Proximate, Ultimate, and Elemental analysis of woody and agricultural biomass (dry basis wt %) [126].

	Wheat Straw	Rice Hulls	Rice Straw	Willow Wood
Elemental Composition in Ash				
SiO_2	55.32	91.42	74.67	2.35
Al_2O_3	1.88	0.78	1.04	1.41
TiO_2	0.08	0.02	0.09	0.05
Fe_2O_3	0.73	0.14	0.85	0.73
CaO	6.14	3.21	3.01	41.20
MgO	1.06	<0.01	1.75	2.47
Na_2O	1.71	0.21	0.96	0.94
K_2O	25.60	3.71	12.30	15.00
SO_3	4.40	0.72	1.24	1.83
P_2O_5	1.26	0.43	1.41	7.40
CO_2/other	-	-	-	18.24
Undetermined	1.82	-0.64	2.68	8.38

Biomass can be processed into charcoal via combustion, gasification, and pyrolysis. Combustion is the burning of biomass in the air between 800 to 1000°C [127]. Although it is inexpensive, it is not very efficient when compared to pyrolysis as the emissions are harmful to the atmosphere. Gasification is the conversion of biomass to gaseous fuel at 700 to 900°C [128]. Pyrolysis is defined as the thermal degradation or decomposition of biomass in the absence of oxygen [128]. Pyrolysis is the only process that results in the biochar required for this research project.

Pyrolysis begins with the devolatilization of the biomass $((C_xH_yO_z)_n)$ by dehydration, decarboxylation, and dehydrogenation, resulting in the formation of carboxyl, carbonyl, and hydroxyl groups. The primary stage is swiftly followed by the secondary stage, where the cracking of heavy compounds into char and gases takes place [120]. The first half of the product corresponds to the gaseous products, and the

second is the liquid products while the third is the production of char (Carbon, C) [129].

The pyrolysis process is influenced by the nature of the feedstock, the temperature, the residence time, the heat transfer, the reactor design, the atmosphere, and the pressure. The influence of the heating rate, temperature, and residence time of the pyrolysis process, determines which type of pyrolysis is taking place, as shown in Table 2.5. The product yield depends on the type of pyrolysis. Generally, char production reduces with an increase in temperature and heating rate, which is why slow and intermediate pyrolysis results in a higher solid product [130]. To see the effect of residence time, temperature, and heating rate on the char characteristics as a flooding fluid, charcoals produced via different methods will be analysed towards EOR.

Table 2.5: Types of Pyrolysis.

	Slow	Intermediate	Fast
Temperature (°C)	550-950	500-650	850-1250
Heating rate (°C/s)	0.1-1.0	1.0-10	10-200
Residence time (s)	300-550	0.5-20	0.5-10
Liquid (dry wood basis wt %)	30	50	75
Solid (dry wood basis wt %)	35	25	12
Gas (dry wood basis wt %)	35	25	13
Ref	[131-134]	[134, 135]	[131-134]

For research purposes, the choice of biomass is crucial as it will affect the behaviour of the nanofluid. The ash content and composition of the charcoal will determine the mineral content, which in turn will affect the alkalinity of the charcoal. Results from the pilot and field-scale flooding using alkaline have shown the potential to reduce the fluid-oil interfacial tension [23, 49-53], while the silica content in the charcoal will be important as literature has demonstrated that silica can alter the wettability of the rock surface.

2.8. Conclusion

In conclusion, the pursuit of Enhanced Oil Recovery (EOR) techniques is crucial for optimising hydrocarbon extraction from reservoirs, particularly in challenging geological formations and mature fields. This literature review has provided a comprehensive overview of various EOR methods, nanofluids, and biomass-derived charcoals, elucidating their principles, applications, and associated challenges.

EOR methods can be broadly classified into thermal, gas injection, and chemical injection techniques. Thermal methods utilise heat to reduce oil viscosity, while gas injection involves injecting gases to enhance recovery rates. Chemical injection alters fluid properties to improve oil displacement efficiency. Despite their effectiveness, these methods face challenges such as environmental implications, gas retention, and cost-effectiveness, necessitating careful consideration of reservoir characteristics and operational factors.

Nanofluids, comprising nanoparticles dispersed in a base fluid, offer significant promise for enhancing oil recovery. Extensive research has explored various nanoparticles, including metal oxides, carbon-based materials, and cellulose nanoparticles, demonstrating their efficacy in improving oil displacement efficiency. Understanding factors such as nanoparticle concentration, size, surface chemistry, and base fluid composition is crucial for optimising nanofluid performance in practical applications.

Viscosity behaviour is a key consideration in nanofluid performance, influencing their flow characteristics and applicability in EOR. Theoretical models and experimental studies help predict and understand nanofluid viscosity behaviour, essential for optimising their formulation and performance.

Interfacial properties, such as interfacial tension, surface tension, and contact angle, play a critical role in nanofluid performance. Various techniques are employed to evaluate these properties, with factors like nanoparticle concentration, size, and temperature significantly influencing interfacial behaviour.

Biomass-derived charcoals, produced via pyrolysis, offer another avenue for enhancing oil recovery. Understanding biomass composition and pyrolysis parameters is crucial for producing charcoals with desired properties for EOR

applications. Charcoals with specific mineral compositions, such as silica, can alter interfacial tension and wettability, making them suitable candidates for EOR.

Overall, continued research and development efforts are essential for advancing EOR technologies and realising their full potential in the oil and gas industry. Collaboration between academia, industry, and regulatory bodies is vital for addressing challenges and optimising the performance and sustainability of EOR practices. Leveraging the insights gained from this review, future research endeavours can focus on developing innovative solutions to meet the evolving demands of the energy sector while ensuring responsible resource utilisation and environmental stewardship.

3. Chapter 3: Experimental Procedures and Methodologies Used in the Research

3.1. Introduction

Charcoal-based nanoparticles have emerged as a promising avenue for enhancing fluid properties in various industrial applications, particularly in enhanced oil recovery processes. The integration of nanoparticles derived from renewable biomass sources, such as wheat straw and rice husk, into fluid matrices offers the potential to modify wettability, reduce interfacial tension, and enhance viscosity, thereby optimising fluid displacement efficiency. This thesis delves into the synthesis, characterization, and experimental analysis of charcoal-based nanofluids, aiming to develop nanofluids from abundant and low-cost charcoals and investigate their suitability as stated in Section 1.2.

By understanding the relationship between nanoparticle properties, fluid behaviour, and environmental conditions, researchers can tailor nanofluid formulations to meet specific performance requirements in diverse applications. Through systematic investigation and experimentation, this study endeavours to unravel the underlying mechanisms governing the behaviour of charcoal-based nanofluids and their efficacy in reservoir engineering applications.

3.2. Varieties and characteristics of charcoals examined in the research

The charcoals studied in this work were prepared from wheat straw and rice husk via pyrolysis as shown in Table 3.1. The wheat straw char (WSCa) was produced using an Auger reactor with a residence time of 10 minutes at 400°C. The rice husk chars (RHCa and RHCb) were produced via both fixed bed pyrolysis reactor and Auger reactor with a residence time of 30 and 10 minutes at 450 and 400°C, respectively. WSCb, Beechwood and Miscanthus were all produced via fast pyrolysis in a fluidised bed at about 500°C. The biomass samples were used in their received form for pyrolysis. A commercial active carbon (AC) (Sigma Aldrich, LOT: MKBQ9520V) was selected to be studied as a reference.

Table 3.1: Characteristics of charcoal types by year of production, pyrolysis type, temperature, and residence time.

Sample	Year	Pyrolysis	Temp (°C)	Residence time
Wheat Straw Char a (WSCa)	2018	Auger reactor	400	10 minutes
Wheat Straw Char b (WSCb)	2014	Fluidised bed	500	<2 seconds
Rice Husk Char a (RHCa)	2014	Fixed batch	450	30 minutes
Rice Husk Char b (RHCb)	2019	Auger reactor	400	10 minutes
Beech Wood	2014	Fluidised bed	500	<2 seconds
Miscanthus	2014	Fluidised bed	525	< 2 seconds
Active Carbon (AC)	-	-	-	-

3.3. Core flooding

For the cores, kiln-dried sand (Quartz) was obtained from Wickes.

Crude oil supplied by Shell Trading International Limited with <0.5% Sulphur CAS no: 8002-05-9 was used, with a viscosity of 3.0 mPa.s 50°C and a density of ~ 820 kg/m^3 at 50°C.

Artificial brine with a viscosity of ~0.47 mPa.s at 50°C was used to simulate oil reservoir conditions. Artificial brine made up of the compounds in Table 3.2 was adapted from the experiment by Ali Levent et al. [136].

Table 3.2: Composition of artificial brine for experimental analysis.

Compound	Quantity (g)	Ion	Total Salt (%)
NaCl	24.5	Cl^-	55.1
$MgCl_2$	5.2	Br^-	0.2
$CaCl_2$	1.2	SO_4^{2-}	7.7
KCl	0.7	HCO_3^-	0.4

Table 3.2 continues the Composition of artificial brine for experimental analysis.

Compound	Quantity (g)	Ion	Total Salt (%)
$SrCl_2$	0.03	Mg^{2+}	3.7
Na_2SO_4	4.1	Ca^{2+}	1.2
$NaHCO_3$	0.2	Sr^{2+}	0.04
KBr	0.1	K^+	1.1
		Na^+	30.6

3.4. Nanofluid preparation methodology: techniques and procedures for synthesising nanoparticle suspensions

3.4.1. Dry milling methodology: procedures and techniques for particle size reduction in the absence of liquids

A planetary micro mill Pulverisette 7 with 0.3 mm zirconium beads, was used for the dry milling of the samples. Initial experiments to determine the most efficient ratio of beads to sample were carried out using three different ratios of milling beads to samples, at a speed of 600 rpm over a set amount of time. The ratios of milling beads to samples were: 1:2, 1:1 and 1:0.5.

The ceramic milling bowls were weighed before and after the addition of both the beads and the samples. The change in sample size was recorded with time for all three ratios; this was repeated three times.

3.4.2. Wet milling methodology: techniques and procedures for particle size reduction in the presence of liquids

DYNO®-MILL ECM-AP 05, DYNO®-MILL Research Lab, and planetary micro mill pulverisette 7 were used for the wet milling. For all three mills, a mixture of 5-2 wt% of the sample was made using distilled water as the base fluid.

DYNO®-MILL ECM-AP 05 was designed for wet milling at a capacity of 1 L. It consists of an accelerator to circulate the beads at a chosen speed of 1800 rpm, with 250 mL Zirconia beads of size 0.3 mm. Both the temperature and the pressure in the system were monitored via a thermocouple and a pressure sensor. A temperature of 25°C, which was kept constant with the aid of a water-cooling system at a rate of 250-400 L/h was used. Initially, the mill was filled with the 250 mL beads, before the

mixture was then charged into the mill via the inlet pipe. The size and zeta potential of the fluid was monitored with time, and the concentration of the sample was changed by the addition of distilled water following sample collection.

DYNO®-MILL research Lab was designed for wet milling at a capacity of 0.15 L. Just like the DYNO®-MILL ECM-AP 05, it consists of an accelerator to circulate the beads at a speed of 3500 rpm and the temperature was controlled at 25^{o}C via the circulation of water. The mill was filled with 55 mL zirconium beads of 0.3 mm and then 100 mL of the sample. As the sample got thicker, a portion was taken, and deionised water was added to change the concentration.

The planetary micro mill pulverisette 7 has two milling bowls of 12 mL each. The samples (8 mL) were first milled with 8 g of zirconium beads of 0.3 mm at a speed of 800 rpm for a given time. When no further size reduction was observed, 0.1-0.2 mm zirconium beads at the same speed for a given time were used.

3.5. Characterization Methodology including techniques and Approaches for Analysing Properties.

3.5.1. Proximate analysis

Proximate analysis is the determination of the contents of moisture, volatile matter, fixed carbon, and ash in a sample. Before analysis, the chars were grounded with mortar and pestle and sieved to under 40 mesh. This analysis was performed with thermogravimetric analysis (TGA), in which a sample is exposed to a pre-determined temperature program, under a selected atmosphere (inert or oxidising). The weight of the sample is continuously measured and plotted (in absolute values or percentages) against the elapsed time or the programmed temperature.

A Mettler Toledo TGA/DSC2 (Thermogravimetry Analysis/Differential Scanning Calorimetry) with STAR^{e} software was applied to carry out the proximate analysis. Each run used approximately 3 mg of the sample with a size under 40 mesh. The sample was heated in pure nitrogen (40 ml/min) from 25 to 50°C at a heating rate of 15 °C/min and kept at isothermal conditions for 30 minutes before being further heated to 105°C at a heating rate of 5 °C/min, and kept at isothermal conditions for 10 minutes to remove all remaining moisture content. It was then further heated from 105 to 900°C at a heating rate of 10 °C/min. The experiment follows ASTM standards,

E1757-19 [137] for the preparation of the charcoal sample, E871-82 [138] for the determination of moisture (M) content, and E872-82 [139] for the volatile matter (VM).

To obtain the ash content (A) in the samples, the samples were exposed to an oxidising atmosphere with an oxygen flow rate of 30 ml/min, mixed with a nitrogen flow rate of 10 mL/min. A protective nitrogen flow of 30 mL/min from 25 to 50°C at a heating rate of 15 °C/min and retained at isothermal conditions for 5 minutes before being further heated to 105°C at a heating rate of 10 °C/min and retained at isothermal conditions for 5 minutes. It was then further heated from 105 to 900°C at a heating rate of 10 °C/min and maintained at isothermal conditions for 5 minutes. The procedure was based on D1102-84 [140], while the fixed carbon (FC) contents were obtained using Equation 3.1.

$$FC(wt\%) = 100 - M(wt\%) - VM(wt\%) - A(wt\%) \quad \text{Equation 3.1}$$

were FC is the fixed carbon content (%), M is the moisture content (%), VM is the volatile matter content (%) and A is the ash content (%).

All the reported data are the average of three measurements with an error of about 0.3%, and the values were obtained in weight percentage, on a wet basis and converted to dry bases (db) using Equation 3.2. A blank measurement was performed to subtract the buoyancy effect.

$$Dry\ basis\ (wt\%) = As\ recived\ (wt\ \%) \times \frac{100}{100 - M\ (wt\ \%)} \quad \text{Equation 3.2}$$

3.5.2. Ultimate analysis

The determination of the main elemental constituents of the samples (carbon, hydrogen, nitrogen, sulphur, and oxygen, obtained by difference), was measured for the samples. The ultimate analysis was carried out using a CHNS/O Flash 2000 Organic Elemental Analyser (Thermo Fisher Scientific). A sample of 2-3 mg along with ~5 mg of vanadium pentoxide (oxidant, to assist complete sample conversion) was combusted and the released gas was analysed for CO_2, H_2O, NO_2 and SO_2 by the gas chromatography for the content of C, H, and N. The difference of C, H, N, and ash content from 100% is assigned as oxygen content. Sulphanilamide was used as the standard for the analyses. All the reported data are the average of three measurements.

3.5.3. Fourier Transform Infra-Red (FT-IR)

The Fourier Transform Infra-Red (FT-IR) spectrometer was used to analyse the charcoal chemical bonds and functionalities. A PerkinElmer FT-IR Spectrometer Frontier and Spectrum software were used. The scanned wavelength was from 4000 to 400 cm^{-1}, a blank scan was carried out before each scan to minimise the background noise. Each scan was carried out at a step of 4 cm^{-1} for 16 scans in triplicates.

3.5.4. Optical microscope

A Motic BA310 Digital Biological Microscope with an objective lens of 4×, 10×, 40×, and 100× was used for the examination of charcoal-based fluids at varied pH values. A drop of the diluted fluid at a controlled pH value was placed on a glass slide. The slides were gently shaken to form a thin layer of sample film for observation. The scale bar was calibrated using the microbar provided by Motic.

3.5.5. Scanning Electron Microscope (SEM)

An Environmental Scanning Electron Microscope (Thermo Quattro S) was used to observe the charcoal nanoparticles. A nanofluid sample prepared was extensively diluted and a drop of the diluted sample was carefully placed on a copper grit for evaporation overnight and then loaded for observation.

3.5.6. pH at Point of Zero Charge (PZC)

To characterise the charcoal surface charging conditions, the pH point of zero charge (pH_{pzc}) was determined for each sample. Three different methods were trailed before a final one was picked.

In method 1, the charcoal sample of 0.1 g was dispersed into a vial that contained solutions with varying pH from 1 to 12. Once the sample was added the pH of the solution was measured and this was taken to be the initial pH. The mixture was left for 24 hours at a constant temperature before the pH was measured again to determine the final pH.

For method 2, 0.1 g of the charcoal samples were placed in a vile then the pH was adjusted to vary from 1 to 12, this was then recorded as the initial pH. The mixture

was also left for 24 hours at a constant temperature before the final pH was measured.

The pH_{pzc} of a material is the pH value at which the material surface is neutral, thus having a zero charge. A solid addition method adapted from [141] was used to determine the point of zero charge of the charcoal samples. NaOH (0.1 M) and HCl (0.1 M) aqueous solutions were used to prepare six starting solutions of 12 mL, each having an initial pH value of 1.0, 3.0, 5.0, 7.0, 9.0, or 11.0, respectively. Charcoal samples of 0.1 g were dispersed into each solution. The mixtures were stirred in a water bath of 25°C for 24 hrs. The pH value of each mixture was then recorded as the final pH value. The final pH values were plotted against the initial ones to determine the point of zero charge, which is the pH where the initial and final pH are equalised. All the measurements were repeated three times. A Jenway 3540 pH and conductivity meter was used in the pH measurement. The pH meter was calibrated using buffer solutions of pH 4.0, 7.0, and 9.2 daily before the measurement.

3.5.7. Particle size and zeta potential measurement

The charcoal particle size and size distribution in the milled fluid were analysed using a Brookhaven Zeta Plus. To avoid any agglomeration, and to measure the primary size of the charcoal particles, the milled fluids were extensively diluted and ultrasonicated after adjusting pH away from their $pH_{pzc.}$ Each sample was repeated at least three times and averages of repetitive measurements were reported.

3.5.8. Viscosity measurement

The viscosity was measured using a Brookfield DV-II Ultra cone or plate (CPA-42) rheometer. The viscosity measurement was carried out either at a given shear rate of 384 s^{-1} (100 rpm) or in the shear rate ranging from 10 to 200 s^{-1} at a given temperature, which was controlled by a Thermos Haake C25P bath with an accuracy of ±0.1°C. The rheometer was calibrated by the viscosity of water at 25°C. Each fluid sample was ultra-sonicated for 1 hr at 25°C directly before the measurement. Each sample was measured at least three times ensuring that the reported data had an accuracy within ± 0.1 mPa.s.

3.5.9. Surface tension and contact angle analysis.

The surface tension and contact angle were measured using a Biolin Scientific Optical Tensiometer Theta Lite with Attention Software (Version 4.0.3).

The selected chars were dispersed in deionised water and sonicated in an ultrasonic bath for an hour to reduce agglomeration. The char concentration in the deionised water was kept constant at 2 wt%. After which, 0.5 mL of the solution was dispersed in 0.5 mL pH-controlled solutions made up of NaOH and HCl, making up a concentration of 1 wt%.

The surface tension was measured at room temperature using a pendant drop shape analysis. Static contact angles were measured in air, using the dispersed nanoparticles in deionised water at room temperature, the concentration and pH of each sample were controlled. The substrate used waswax-coatedd glass slides.

3.5.10. Permeability

The analysis of the permeability of the core was carried out after the porosity was determined. A vessel filled with water was placed on a lab jack and connected to the saturated core, the height was adjusted to allow little to no of hydraulic pressure. The quantity of water collected was measured every 10 minutes and used to calculate the flow rate. Equation 3.3 which describes Darcy's law was used to calculate the permeability.

$$k = v\frac{\mu \Delta x}{\Delta P} \quad \text{Equation 3.3}$$

where v is the fluid velocity through the porous medium (m/s); k is the permeability (m^2); μ is the dynamic viscosity of the fluid (Pa·s); Δx is the thickness of the bed of the porous medium (m) and ΔP is the applied pressure difference (Pa).

3.6. Core packing and flooding methodology: procedures for assembling core samples and conducting fluid flow experiments

3.6.1. Sieving analysis

The rig consists of 3 storage tanks with a capacity of 200 mL, a cylindrical pipe with dimensions 300 by 20 mm and a volume of 94 mL made from copper.

Before packing, the moisture content of the sand was measured to be about 0.1%. The sand is collected via cone and quartering method, to ensure the samples are representative.

The collected samples from the cone and quartering are placed through the top of the sieve and are allowed to fill the compartments without any interference. Once the sample has been placed, the sieve is vibrated by hand for about 30 seconds, to ensure that particles have been settled throughout the compartments and that particles are falling into the available empty spaces. The sieve was vibrated for 5 minutes and then each mesh compartment was taken out individually and the material collected where weighed.

3.6.2. Core packing

One of the parameters that was considered while packing the core was the void space. Void space is often characterized by porosity, which is dependent on the particle shape and size. The particle shape that is present within each particle size will differ, therefore the arrangement of packing can significantly change. Parameters such as the pore volume pore size and pore uniformity play an important role in the sweeping of the fluids within the core, which is why a method to get repeatable data was developed.

To determine the pore volume, the weight of the core before and after packing with sand was recorded. Once the core was packed with sand, it was submerged in water for 24 hours to allow full saturation. After 24 hours, the weight of the saturated pore was measured, and the weight of the core and sand was taken away from that of the saturated core to determine the amount of water within the pores. This was taken as the pore volume. The bulk volume is the volume of the core which is 94.2 mL. Equation 3.4 was used to calculate the porosity.

$$Porosity\ \emptyset = \frac{V_p}{V_B} \quad \text{Equation 3.4}$$

$$V_p = Pore\ Volume\ (m^3) V_B = Bulk\ Volume\ (m^3)$$

3.6.3. Oil loading and water flooding of the core

The oil loading and flooding were carried out on a homemade flooding rig, where the fluids were pumped (a Longer L100-1E peristaltic pump) into a horizontal temperature-controlled core. The temperature is controlled at 50°C via the hot water

circulation through a jacket on the core (a HAAKE C25P Refrigerated Bath with Phoenix II Controller). The packed wet core was first rinsed using the artificial brine. At the outlet of the core, a back pressure reducer (Flomasta pressure reducing valve 1) was installed and set at 2 full turns. About 50 mL of the artificial brine was fed into the core to fully replace the deionised water and then the back pressure reducer was closed, and the rig was left on standby for 24 hours. The core was then ready for crude oil loading.

The pump was switched to the crude oil tanks, which are maintained at 50°C using an IKA IKAMAG Works RCT S 19 Hot Plate Stirrer (UGK86) for oil loading by replacing the artificial brine trapped in the pore of the packed core. The pumping rate was controlled constantly at 1.8 mL/min and the back pressure reducer was set at 2 full runs. While the crude oil pumping was going on, the effluent was collected in 25 mL measure cylinders and the volume of effluent brine and crude oil was recorded with the oil feeding time. The crude oil feeding stopped when more than 25 mL of crude oil was continuously collected with no brine observed in the effluent. The core was left on standby for 24 hours to allow saturation into the pores. The recorded volumes of the brine and crude oil were used to produce the crude oil loading curves.

For water flooding, the pump was switched to a deionised water tank. The water flooding procedure and conditions used were the same as that used in the crude oil loading. While the deionised water was pumped in and crude oil in the effluent was monitored for the stop of water flooding. When at least 25 mL of water was collected without observable crude oil in it, the water flooding was completed. The core was ready for enhanced oil recovery.

3.6.4. Charcoal-based nanofluid flooding

Sectional flooding is applied to test the performance of the charcoal-based nanofluid in the enhanced oil recovery. Sectional flooding means to send a volume of another fluid equivalent to a sectional volume of the core to change the oil/water/reservoir wall condition and then continue the water flooding for oil recovery. In this study, the charcoal nanofluid equivalent to 20% of the pore volume in a specific core was pumped into the core at the end of the water flooding at a flow rate of 1.8 ml/min. After that, water flooding was continued. During the operation, both crude oil and

black nanofluid in the effluent were monitored to examine the flow pattern of the charcoal-based nanofluids and their performance in enhanced oil recovery.

4. Chapter 4: A Theoretical Study of Viscosity Enhancement of Nanoparticles

4.1. Introduction

Much progress has been made in the development of the theoretical framework describing the relationship between the viscosity changes with the nanoparticle volume fraction, but further progress is needed for the description of the viscosity change with respect to the properties of the added solid nanoparticles and their interaction to the base liquid and each other in the base liquid, especially when the nanoparticle population becomes large (e.g. for small particle size and large volume fraction) and the interaction of the nanoparticle to the base liquid and other particles is strong.

To make further progress, literature around the relative viscosity data of nanofluids using various reported theoretical models will be analysed, which will show that a better interpretation of the literature data is afforded by the adaptation of Chen's equation via introducing a new parameter denoted as the Dispersion Factor (DF) to describe relative viscosities of nanofluids dependent on nanoparticle volume fraction.

4.2. Viscosity enhancement of metal oxide nanoparticles: Experimental data and modelling

Nanoparticles with metal oxides are a group of widely studied viscosity enhancers for their applications in processing engineering. Some experimentally measured relative viscosity data from representative studies of different-sized TiO_2 [89, 99, 101, 102, 142, 143], γ-Al_2O_3 [99, 100, 103, 104, 143-145], and SiO_2 [104, 144] nanoparticles dispersed in water have been selected, and have compared the experimentally measured (data points) and calculated (lines) relative viscosity vs. nanoparticle volume content for each type of metal oxide as shown in Figures 4.1 to 4.3, respectively.

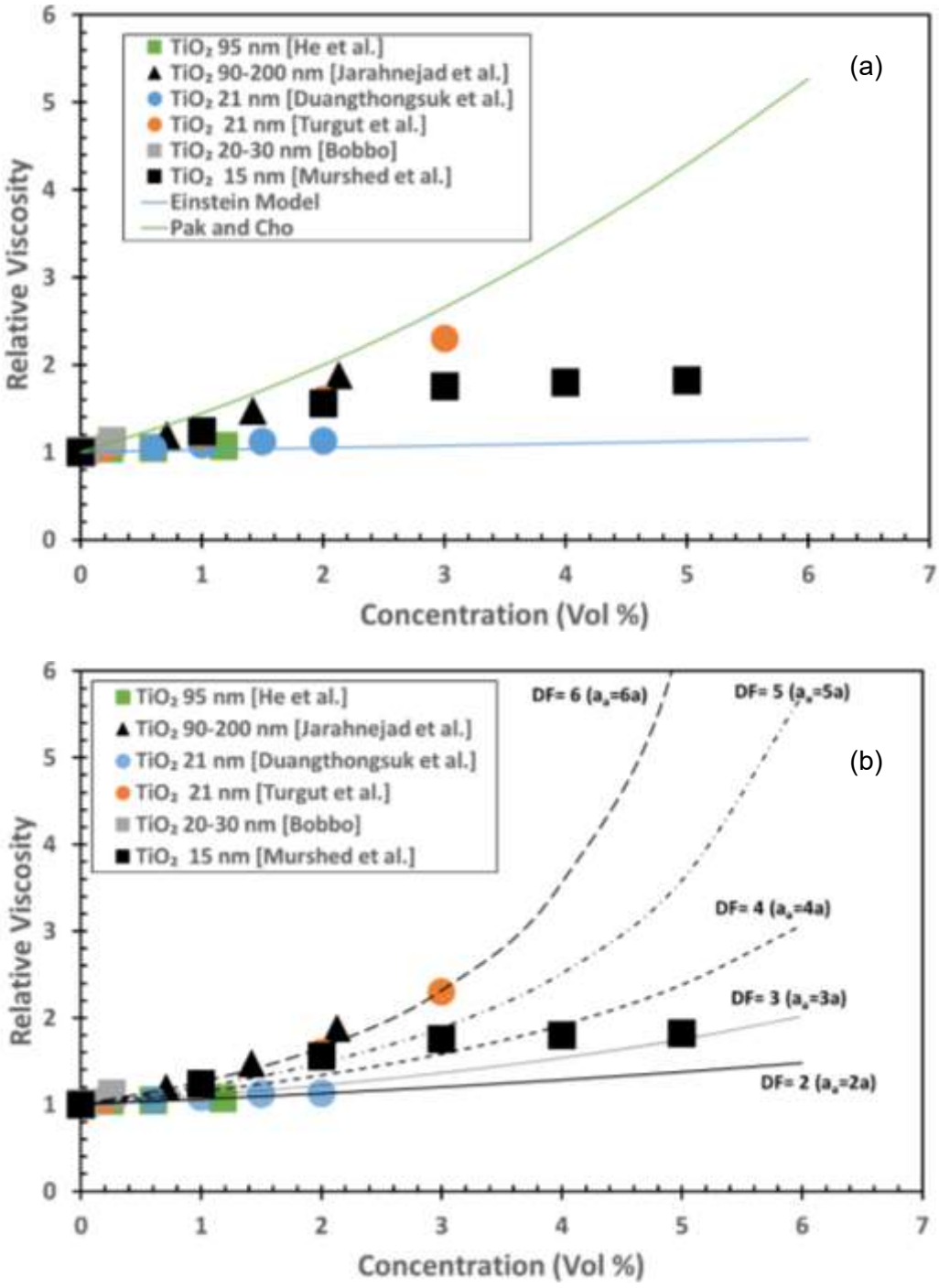

Figure 4.1: The experimental relative viscosity data (data points) for different TiO_2 nanofluids vs. their concentration (in vol%) compared to the calculated lines based on (a) the Einstein model and the Pak and Cho equation, and (b) Chen equation that includes the Dispersion Factor (DF) parameter.

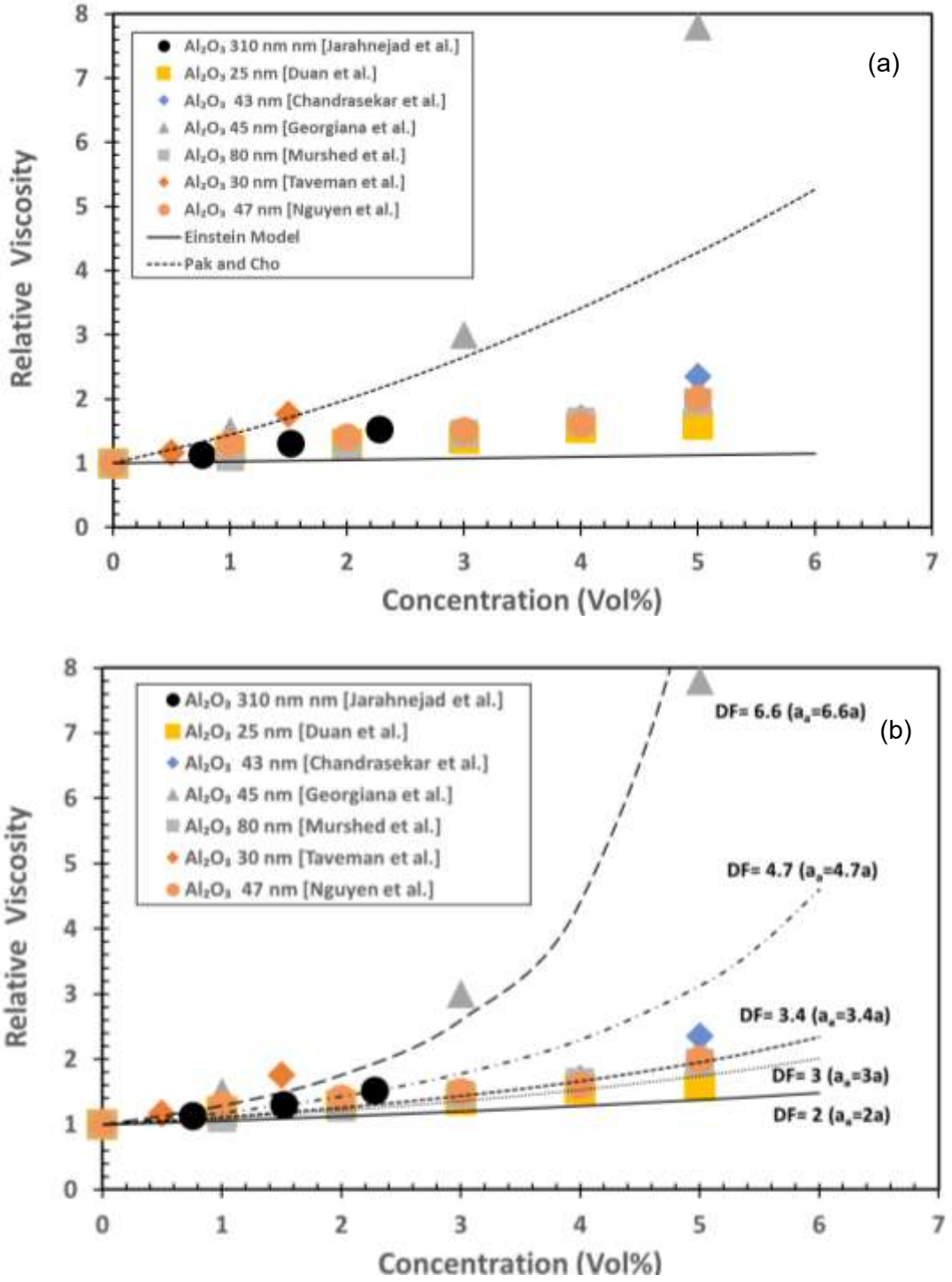

Figure 4.2: The experimental relative viscosity data (data points) for different γ-Al_2O_3 nanofluids vs. their concentration (in vol%) compared to the calculated lines based on (a) the Einstein model and the Pak and Cho equation, and (b) the adapted Chen equation that includes the Dispersion Factor (DF) parameter.

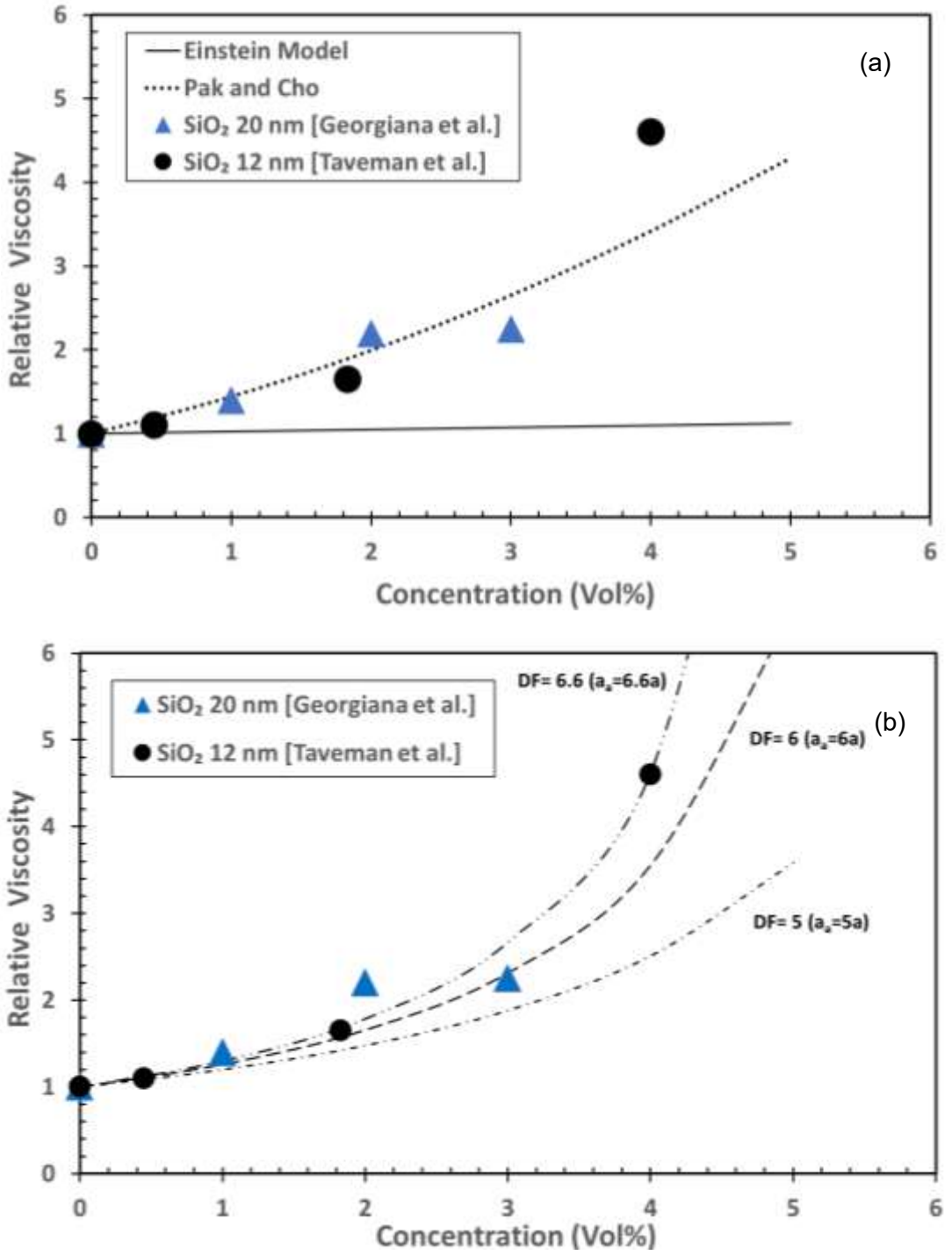

Figure 4.3: The experimental relative viscosity data (data points) for different SiO_2 nanofluids vs. their concentration (in vol%) compared to the calculated lines based on (a) the Einstein model and the Pak and Cho equation, and (b) the adapted Chen equation that includes the Dispersion Factor (DF).

To allow a strict comparison, all the data selected were measured at a temperature between 20 to 25°C. Figures 4.1 to 4.3 comprise a double triad of data, i.e. three different groups of literature data points for TiO_2, γ-Al_2O_3, and SiO_2 nanofluids, with lines resulting from the data being subjected to the various reported theoretical and empirical equations (Figures 4.1a, 4.2a, 4.3a) and to Chen's equation (Figures 4.1b, 4.2b, 4.3b).

If we examine the data points, then it becomes clear that in general, the relative viscosity increases with the nanoparticle content, but the increment does not vary with particle size consistently. The relative viscosity ratio also varies with particle composition, which in turn affects the particle surface properties and its interaction with the base liquid. The calculated lines derived from the Einstein and Pak and Cho equations, included in Figures 4.1a, 4.2a and 4.3a, represent the low and high boundaries of the experimental data in the studied concentration range, respectively. The lines calculated by the equations of Brinkman and Batchelor are remarkably close to that of the Einstein equation; in fact, they virtually overlap at the scale used, thus can be considered as similar in the discussion (*vide infra*), hence only the Einstein line has been included in the figures. Figures 4.1a, 4.2a and 4.3a show that when the nanoparticle volume content is less than 1 vol.%, the calculated relative viscosity given by the Einstein equation is close to the experimental data, which is consistent with the Einstein equation being valid for spherical particles at a content less than 1 vol.%. Consequently, when the nanoparticle volume content is above 1 vol.%, all data points, even the low boundary of experimental values, lie significantly above the Einstein line.

The relative viscosity varying with nanoparticle volume content calculated using the Pak and Cho equation shows a line at the high boundary of the experimental data (Figures 4.1a, 4.2a and 4.3a). The Pak and Cho equation has a similar form to that of the Batchelor equation, but the constants were empirically derived from experimental data of γ-Al_2O_3 and TiO_2 nanoparticle aqueous suspensions in the concentration range of 1- 3 vol.%. The Pak and Cho line fits better with the high boundary of the experimental data of Al_2O_3 (Figure 4.2a) and SiO_2, (Figure 4.3a), while it lies slightly higher than the data points for TiO_2 (Figure 4.1a). While this supports the experimental findings that γ-Al_2O_3 nanoparticles provide better viscosity enhancement than TiO_2 [99, 102, 104, 144], the theory is unable to satisfactorily

model the difference in data for these different metal oxides. It is particularly noteworthy that the data points located between the Einstein and Pak and Cho lines in Figures 4.1a, 4.2a and 4.3a could not be described or predicted by any of these reported equations.

4.3. A new parameter of Dispersion Factor (DF)

The present analysis and discussion of literature data show the limitation of the relative viscosity equations of Einstein (1906), Brinkman (1952), Batchelor (1977) and Pak and Cho (1998) in modelling the experimental data. The origin of this discrepancy lies in the fact that these equations relate the relative viscosity only to nanoparticle content, but do not reflect particle size, shape and/or chemical composition nor the interaction between particles or particles to the base liquid. The important implication is therefore, that these equations cannot realistically distinguish the viscosity enhancement resulting from a difference in particle size, shape and/or chemical composition nor can they consider the interaction between nanoparticles or interactions between a nanoparticle to the base liquid. Further complications arise when nanoparticles aggregate, or agglomerate in the suspension; in such situations, the modelling becomes even more challenging.

Particle dispersion or aggregation/agglomeration is a major occurrence in suspension preparation. It is for this reason that Chen et. al. (2007) modified the Krieger-Dougherty equation, as shown in Equation 2.10 [87], by including a factor called agglomerate ratio (the ratio of agglomerate radius to that of the nanoparticle) to reflect the effect of particle agglomeration on the relative viscosity. We have used and expanded this approach by assigning different numerical values to the agglomerate ratio, which resulted in the various calculated lines showing the variation of the relative viscosity with nanoparticle volume content that is drawn in Figures 4.1b, 4.2b and 4.3b. The experimental data can thus be described by a line with an agglomerate ratio in the range of 2 to 6.6.

It may be tedious or even premature to assign a particular Diffusion Factor (DF) value to a set of data originating from a particular study as the number of recorded data points is rather limited. To shed further light on this, more comprehensive experimental studies are required (and may become available in the future). However, at this stage, a focus on the general patterns can be offered.

In a general sense, the results could be interpreted by considering that the relative viscosity increases with the agglomerate ratio at a given nanoparticle volume content; and the larger the aggregation, the larger the viscosity enhancement would be. Intriguingly, this conflicts with the general understanding that 1) the smaller particle size corresponds to a higher particle population for a given nanoparticle concentration thus resulting in a shorter distance between the nanoparticles and 2) the high nanoparticle surface area to its volume ratio boosts the interaction between the nanoparticle surface and the base liquid via the large interaction surface area. The consequence is that the van der Waals forces between the nanoparticles, as well as those between the nanoparticle and the base fluid, become larger when the nanoparticle is smaller, which leads to a large viscosity increase if the nanoparticles are dispersed well apart from one another in the base liquid.

Chen et.al. (2007) defined the agglomerate ratio as the quotient of agglomerate radius to nanoparticle radius, hence in the Chen equation the agglomerate ratio is strictly related to a radius or size ratio, rather than being correlated with the nanoparticle size itself or the chemical composition of the nanoparticle.

4.4. Conclusion

The analysis suggests that the term agglomerate ratio can instead be represented by a parameter that has a pure numerical value. This treatment will enlarge the applicable scope of the model by including the effect of actual nanoparticle sizes and chemical compositions via the interaction between nanoparticles and the nanoparticles to the base liquid. To reflect the more comprehensive nature of this new ratio, this research would like to suggest the new parameter Dispersion Factor (DF) that is to be included in Equation 2.10, thus yielding Equation 4.1.

$$\frac{\eta_{\mathrm{eff}}}{\eta_{\mathrm{bf}}} = \left(1 - \frac{\varphi}{0.605}(DF)^{1.2}\right)^{-1.5125} \qquad \text{Equation 4.1}$$

In this equation, the DF is represented by a pure numerical value, which comprehensively reflects the effect of the nanoparticles in the base liquid and their interactions with the base liquid and themselves on the relative viscosity. The significance is that the value of DF can be determined from the experimental data, and its value captures crucial information in the following manner:

If the modelling of experimental data gives a larger DF value, it means that there is 1) a smaller size and larger aspect ratio of nanoparticles; 2) a stronger interaction of particles to the base liquid and among themselves, or more complicatedly 3) the formation of secondary functional entities formed from the nanoparticles as, e.g., aggregates. The larger the aspect ratio of the secondary functional entities, the more significant their effect on the relative viscosity.

When the nanoparticle sizes are comparable and the nanoparticles are suspended in the same base liquid, the DF value difference will reflect the relative interaction strength of the nanoparticles to the base liquid, as shown by the modelling of the data in Figures 4.1b, 4.2b and 4.3b. The magnitude of the Dispersion Factor, therefore, can be used to evaluate the dispersion condition of nanoparticles in the base liquid or the interaction strength of the nanoparticle surface to the base fluid.

5. Chapter 5: Properties of the Selected Charcoals

5.1. Introduction

The charcoals used in this research are made via the pyrolysis of biomass as discussed in Chapter 2. From the literature review in Chapter 2, it was noted that different types of biomasses have varying compositions, ash contents and organic contents. A representative sample selection is needed to better understand the effect of the different compositions and porosities on the behaviour of the nanofluid during EOR. Four different biomasses, namely, rice husk, wheat straw, beech wood and miscanthus were selected for their abundant availability as the by-product of food or energy crop productions. These biomasses are converted into biofuel through pyrolysis and their charcoals remain as by-products. Six charcoal samples of these four biomasses were sourced from EBRI and Carbon Future for the selection. Among these charcoals were processed by slow, intermediate or fast pyrolysis at varying temperatures and pyrolysis reactors. As a reference, an active carbon sample from Sigma-Aldrich is included. The charcoal samples were analysed for their proximate and elemental compositions, surface chemical functional groups (FTIR) and their interaction with water (pH at point of zero charge).

5.2. Proximate and ultimate analysis

A preliminary analysis is carried out on six charcoal samples as displayed in Table 3.1: a wheat straw char sample produced via slow pyrolysis in an Auger reactor at a temperature of 400°C and a residence time of 10 minutes (WSCa); a wheat straw char sample produced via fast pyrolysis in a fluidised bed at a temperature of 500°C and a residence time of <2 seconds (WSCb); a rice husk char sample produced via slow pyrolysis in a fixed batch reactor at a temperature of 450°C and a residence time of 30 minutes (RHCa); a rice husk char sample produced via slow pyrolysis in an auger reactor at a temperature of 400°C and a residence time of 10 minutes (RHCb); a beech wood char sample produced via fast pyrolysis in a fluidised bed at a temperature of 500°C and a residence time of <2 seconds; and a miscanthus char sample produced via fast pyrolysis in a fluidised bed at a temperature of 500°C and a residence time of <2 seconds. The proximate analysis of the selected charcoal samples is listed in Table 5.1.

Table 5.1: Proximate analysis in wt% dry basis (db) and wt % dry ash-free (daf).

Sample	Pyrolysis Temperature (°C)	Pyrolysis Reactor	Fixed Carbon (wt %)		Volatile Matter (wt %)		Ash (wt %)
			db	daf	db	daf	db
WSCa	400	Auger	50.4	56.7	38.5	43.3	11.2
WSCb	500	Fluidised bed	54.2	61.0	34.6	39.0	11.2
RHCa	400	Auger	40.9	57.2	30.6	42.8	28.5
RHCb	450	Fixed bed	42.7	64.3	23.7	35.7	33.6
Beechwood	500	Fluidised bed	58.4	61.3	36.8	38.7	4.8
Miscanthus	525	Fluidised bed	49.7	60.1	32.9	39.9	17.4
Active Carbon (AC)	-	-	57.7	63.8	32.7	36.2	9.6

The ash in all charcoal samples presented varying quantities. Both wheat straw charcoals were processed at two variable conditions, WSCa in an Auger reactor at 400°C and WSCb in a fluidised bed reactor at 500°C. The ash content in both samples was similar. The RHC, WSC and Miscanthus samples all are rich in ash, of which the RHCb contains the highest amount at 33.6 wt.%, WSC at 11.2 wt%, AC at 9.6 wt%, and RHCa at 28.5 wt% db, when compared to results by [146] at a similar temperature, and a residence time of 10 min, the ash content is comparable with a value of 28.7 wt% dry basis.

The ultimate analysis of the charcoals shown in Table 5.2, gives a breakdown of the carbon, hydrogen, oxygen, nitrogen, and sulphur content following pyrolysis.

Rice husk contains ~20 wt% of silica [147, 148] and wheat straw contains ~7 wt% of silica [149] and ~1.2 wt% of K, Mg and Ca, of which potassium is most dominant with ~1 wt% [150]. Carbon is the richest element as organic matter, which is, on a dry basis, 74.3 wt% for WSCa, coinciding with results by Vieiral et al. [146] (73.1 wt% daf) at the same pyrolysis conditions. 52.6 wt% for RHCb and 55.9 wt% for AC. The

AC has 31.42 wt% oxygen on n dry basis, while the oxygen contents for WSC and RHC are close at 9.59 wt% and 9.62 wt%, respectively.

Table 5.2: Ultimate analysis wt% dry-basis (db) and dry ash-free (daf) basis.

Sample	Ash (wt %)	Carbon (wt %)		Hydrogen (wt %)		Oxygen (Diff) (wt %)		Nitrogen (wt %)		Sulphur (wt %)	
	db	db	daf	db	daf	db	daf	db	daf	db	daf
WSCa	11.2	74.3	83.7	3.9	4.4	13.6	15.3	1.0	1.2	0.0	0.0
WSCb	11.2	74.1	83.4	3.9	4.4	14.2	14.9	1.0	1.1	0.0	0.0
RHCa	28.5	53.8	75.3	3.4	4.7	16.5	23.1	1.0	1.4	0.0	0.0
RHCb	33.6	52.6	79.2	3.4	5.1	12.4	12.8	0.8	1.2	0.0	0.0
Beechwood	4.8	74.8	78.6	3.3	3.5	21.2	22.3	0.5	0.5	0.0	0.0
Miscanthus	17.4	64.0	79.8	3.0	3.6	18.8	22.7	0.6	0.7	0.1	0.1
Active Carbon (AC)	9.6	55.9	61.8	2.7	3.0	34.5	38.2	0.5	0.5	0.0	0.0

Following the proximate and ultimate analysis, the most significant difference is the ash content in the charcoals. The ash content of the charcoal is predicted to be crucial to the behaviour of the nanofluid as an EOR flooding fluid, as a result of the presence of inorganic ions such as Ca, K, Mg, Na, P, Cl, Si, and S in the ash, hereby, affecting the pH of the charcoal, resulting in a natural alkaline pH. The effect of each of the ions on the behaviour of the charcoal as a flooding fluid in this research is unknown as of now. However, having the information on the proximate and ultimate analysis will aid in understanding the performance of the flooding fluids.

5.3. Chemical functional groups

The charcoals, as well as AC, are analysed by FTIR spectroscopy for their chemical functional groups. Their IR spectra are displayed in Figure 5.1. The IR spectra of RHC and WSC have strong absorption bands at ~795 and ~1080 cm^{-1}, which can be assigned to stretching and bending vibrations of Si-O [151-153], respectively. This is consistent with the fact that RHC and WSC are rich in silica [147-149]. The vibrational

bands of silica cannot be found in the IR spectrum of AC, suggesting that no silica is present in the AC.

The IR spectra of the samples all have a wide band at ~3350 cm^{-1}, and significant bands in the range of ~1600-1575 cm^{-1} and 1500–1400 cm^{-1}, which can be assigned to the O–H vibrations of carboxylic or phenolic groups, and skeletal C–C stretch vibration in aromatic rings, respectively. These bands are stronger in the WSC and AC IR spectra than in the RHC IR spectrum, reflecting the higher carbon-based organic content in WSC and AC compared to RHC. The IR spectrum of WSC, as well as that of AC, shows absorption bands at 1319 cm^{-1} assigned to C-O stretching vibrations, and at 875 cm^{-1} assigned to C=C bending vibrations. However, in addition, the AC IR spectrum shows absorption bands in the IR fingerprint zone at 1171 cm^{-1}, 988 cm^{-1} (C=C bending), 870 cm^{-1}, 751 cm^{-1} (C-H bending) and 495 cm^{-1}. The presence of these various aromatic carbon and oxygen-containing functional groups in conjunction with the elemental composition and ash components being different for all three samples is of importance for the present study as these factors are thought to be responsible for the perceived differences in surface chemistry interactions to the base liquid in the fluid.

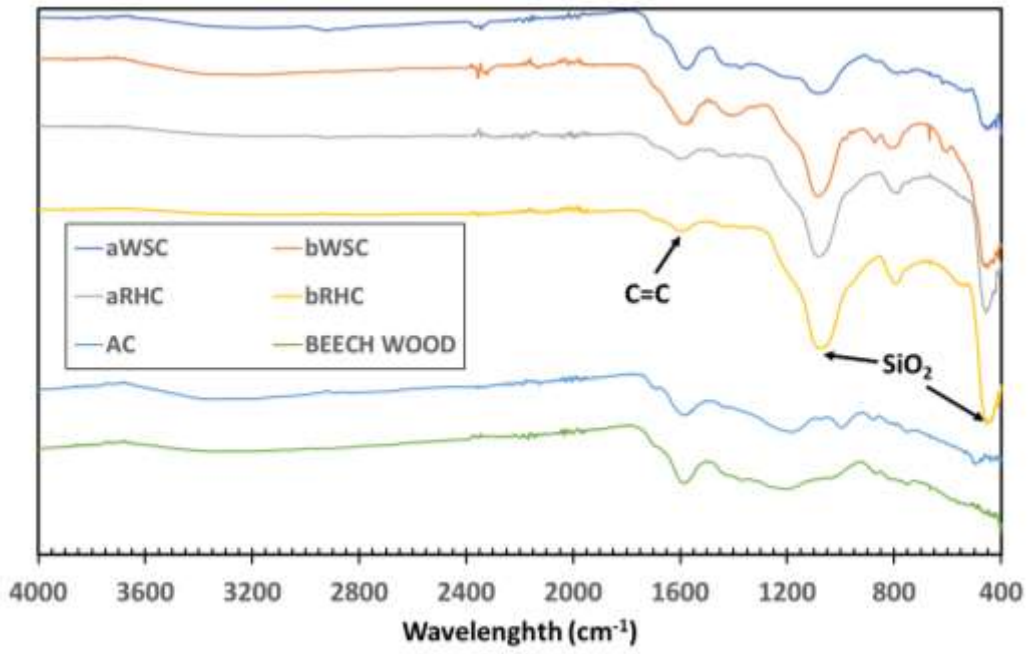

Figure 5.1: FTIR Spectra of Hardwood charcoal, Beechwood charcoal, Miscanthus charcoal, WSCa, and WSCb, RHCa, RHCb.

In conclusion, the FTIR analysis gives a better understanding and knowledge of the chemical structure and functional groups under different pyrolysis conditions and feedstock. It shows the presence of SiO_2 in both RHCs and WSCs, which has been linked to wettability [154].

5.4. pH at Point of Zero Charge (pH_{pzc})

Following the charcoal characterisation using the proximate, ultimate, and FT-IR analysis, the point of zero charges (PZC) analysis was carried out to give the pH at which electrostatic attraction leads to adsorption.

Three different methods were used to find the pH_{pzc}. The pH meter was calibrated before using with buffer solutions (pH 2.0, 4.0, 7.0, and 9.2).

The methodology establishment was carried out, using three different methods, In the case of methods 1 and 2, the reaction between the charcoal and the NaOH started before the assessment of the initial pH measurement. The adsorption of the NaOH onto the surface of the charcoal is accelerated at the beginning, which is why for methods 1 and 2, the time between the addition of the NaOH and the measurement of the pH led to an operational error. In method 3, the pre-mixing and pre-measuring of the pH of NaOH and KCl eliminated the time delay leading to a more reliable result. Therefore, method 3 was chosen to analyse the pH_{pzc} of all future samples.

The pH point of zero charge (pH_{pzc}), was determined for each sample for its surface charging condition in water by method 3. Figure 5.2 shows the final pH values RHCb, WSCa and AC as a function of the various initial pH values.

The data for WSCa and RHCb show similarly shaped curves with pH_{pzc} values located at pH 7.4 for WSCa and pH 6.6 for RHCb, implying that the surface charge switches from positive to negative at these respective pH values. The WSCa surface shows a slightly alkaline characteristic, which can be attributed to its richness in potassium-containing compounds as evidenced by > 1 wt% of potassium in raw wheat straw [150]. This pH_{pzc} of pH 7.4 determined for WSCa is remarkably close to the pH_{pzc} value of pH 7.8 for another wheat straw char studied by [141]. The RHCb surface is slightly acidic with a pH_{pzc} value of 6.6. This pH_{pzc} value should be related to the high ash content of RHCb at 33.6 wt% (on a dry sample basis), which is

dominated by silica. Both charcoals show a significant surface buffer effect in the range of pH 4.0 – 9.2, which is evidenced by the final pH value being levelled in this range (Figure 5.2). Subsequently, the final pH gradually increases from pH 9.2 to pH 12.0.

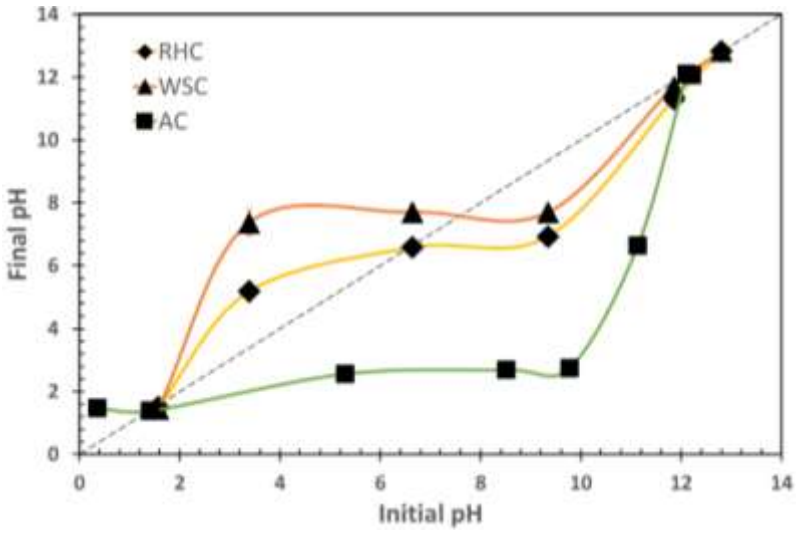

Figure 5.2: The final pH value versus corresponding initial pH values for aqueous solutions containing RHCb, WSCa or AC. The dotted line represents y=x for finding an accurate pH_{pzc} value.

On the other hand, the AC surface is strongly acidic with its pH_{pzc} at pH 1.4. After this pH_{pzc} value, a two-stage surface buffer effect shows in the range of ~pH 2.0-5.0 and ~pH 5.0 to 9.5, and then the final pH value starts to increase considerably, gradually reaching pH 12.0. The pH_{pzc} values are summarised in Table 5.3, together with the ash content and BET measurement data of specific surface areas and micropore volumes that are determined by N_2 gas adsorption.

Table 5.3: pH_{pzc} and specific surface area and micropore volume of the charcoals studied.

Sample	pH_{pzc}	BET Surface Area (m^2/g)	Micropore Volume (cm^3/g)
WSCa	7.4	11	0.027
RHCb	6.6	22	< 0.001
AC	1.4	1600	2.000

Both WSCa and RHCb have small specific surface areas at 11 and 22 m^2/g, respectively, which is rather minor compared to that of AC at 1600 m^2/g. The small

specific surface areas of WSCa and RHCb correspond to their low specific micropore volumes, e.g., 0.027 cm^3/g for the WSCa and negligible for RHCb. In contrast, the large specific surface area of 1600 m^2/g of AC is associated with a micropore volume of 2.000 cm^3/g, which is the volume of pores with an opening smaller than 2 nm. Compared to the commercially widely used highly microporous AC, the specific surface area and micropore volume are exceedingly small for WSCa and RHCb. The difference allows the study of the effect of a variation in the porosity of the nanoparticles on the viscosity of the nanofluid.

Following the characterisation of the charcoal samples, RHCb and WSCa samples have been chosen for preliminary analysis due to their SiO_2 content and pH_{pzc}.

Following the characterisation of the charcoals different samples and pyrolysis conditions result in varying surface chemistry, carbon content, ash content and organic matter contents.

Wheat straw and rice husk are produced agricultural wastes of food production that are exceedingly investigated for their waste valorisation. Wheat straw, and especially rice husk, is composed of a significant amount of minerals. Rice husk contains ~20 wt% of silica [147, 148] and wheat straw contains ~7 wt% of silica [149]. These minerals remain as ash in the charcoal after pyrolysis.

From the analysis carried out, it is evident that rice husk char (RHC) has the highest ash content and a more prominent silica bond. Through literature review, the ability of silica to improve the recovery rate when used as an EOR fluid has been demonstrated [24, 69], which is why RHCb has been selected to be researched further towards its use in an EOR fluid. To better understand the effect of factors such as ash content and the abundance of Wheat straw in the United Kingdom, WSCa was selected for further study alongside RHCb.

Moving forward, RHCb and WSCa will be referred to as RHC and WSC, respectively. The following chapters will look at the characteristics of both samples towards being an EOR fluid alongside active carbon (AC) which will be used as a reference.

5.5. Conclusion

In conclusion, the characterisation of charcoals derived from different sources and under varying pyrolysis conditions has highlighted significant differences in surface

chemistry, carbon content, ash content, and organic matter content. Of particular interest are rice husk and wheat straw, agricultural waste materials rich in minerals such as silica. Rice husk, with its notably high silica content, emerges as a promising candidate for further investigation as an Enhanced Oil Recovery (EOR) fluid, given the documented benefits of silica in improving recovery rates. Wheat straw, abundant in the United Kingdom, also warrants further study alongside rice husk for its potential application in EOR fluid development.

In subsequent chapters, the focus will shift to a detailed examination of the characteristics of rice husk char (RHC) and wheat straw char (WSC) concerning their suitability as EOR fluids. These investigations will be conducted alongside active carbon (AC) as a reference material. By elucidating the properties and behaviours of these charcoals, this research aims to contribute valuable insights to the development of effective EOR strategies and the valorisation of agricultural waste materials.

6. Chapter 6: Preparation and Characterisation of charcoal-Based Nanofluids

6.1. Nanofluid Preparation

The nanofluid used in this research was prepared by milling as described in Chapter 3. A ball mill is a type of grinder used in grinding (reducing the size of the particle) or mixing materials like ores, chemicals, ceramic raw materials, and paints. DYNO®-MILL ECM-AP 05, DYNO®-MILL Research Lab, and a Pulverisette 7 were used in this research. Ball mills rotate around a horizontal axis, partially filled with the material to be grounded, plus the grinding medium which can include ceramic balls, flint pebbles, and stainless-steel balls. An internal cascading effect reduces the material to a fine powder. A ball mill can be used in both dry and wet states.

The key properties of ball milling are size, density, hardness, and composition. The smaller the medium particles (zirconium oxide), the smaller the particle size of the final product (charcoal). However, the grinding media particles should be substantially larger than the largest pieces of material to be grounded. The medium should be denser than the material being grounded and hard enough to grind the material.

Dry milling uses particle-on-particle contact to reduce the size of the materials, with one of the particles being harder than the other. In this case, the zirconium oxide beads are used to mill the charcoal as described above. Wet milling on the other hand involves dispersing the particle (charcoal) in a liquid (deionised water) and using a solid (zirconium oxide beads).

A planetary micro Pulverisette 7 mill was used with zirconium milling balls of 0.3 mm at a speed of 600 rpm. The reduction in particle size over time during the dry milling of WSCa, WSCb, and AC is shown in Figure 6.1.

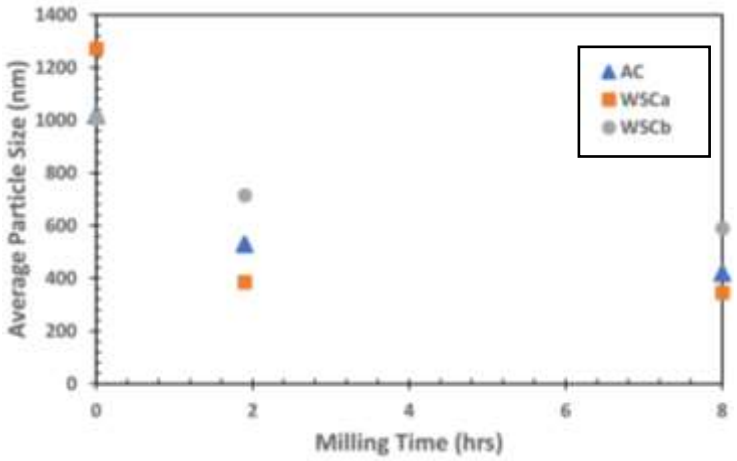

Figure 6.1: Particle size reduction with time for different ratios (Deionised water: Charcoal): AC (1:2), WSCa (1:1) and WSCb (1:0.5) samples.

It is worth noting that the char-to-ball ratio differs for each of the samples. The chars have a range of hardness and porosity making them difficult to compare. However, looking at them individually, it is prominent that at 1.9 hr the highest size reduction of 30% was observed for WSCa, with a minimal reduction in size after 6 hrs of further milling. The milling efficiency was reduced; this could be due to the size of the milling balls. At this point, wet milling was introduced.

The RHCb sample was mixed with distilled water to make a 2 L solution at an initial concentration of 2 wt%. A DYNO®-MILL ECM-AP 05 was used at a speed of 1800 rpm, a temperature of 25°C, and 250 mL of 0.1 mm zirconia balls were used. The concentration of the sample was changed by the addition of distilled water following sample collection. The mill was then properly cleaned and prepped for the next sample after each run.

The nanofluids prepared by wet bead milling were imaged by both optical and electronic microscopes. The images in Figure 6.2 show that when the nanofluids are dried for electronic microscopic imaging, the charcoal nanoparticles are agglomerated together as dried flocs, small or large depending on the sample and its preparation. Under the optical microscope, the agglomeration of charcoal nanoparticles has been observed as shown in the inserts in Figure 6.2 as re-dispersible by adjusting the pH value of the nanofluids. At an alkaline condition, small particles, smaller than 1 μm dispersed in water have been observed for the three nanofluids, which approaches the limit of optical microscopes.

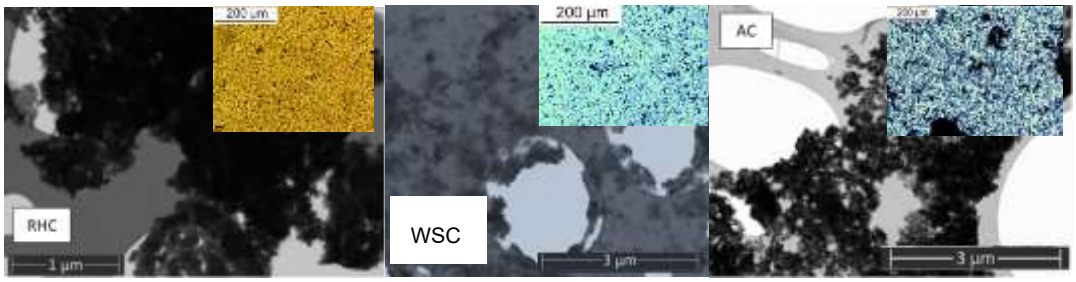

Figure 6.2: Electronic and optical microscopic images of the nanofluids prepared from WSC, RHC, and AC, respectively. The optical microscopic images are the inset.

6.2. Effect of pH values on particle size

The particle size and size distributions are measured by DLS at pH 2.0, 7.0 and 11.0 for each of the nanofluids and the results are shown in Figure 6.3. The particle size distribution curves are normalised at 100, at particle distribution peaks (the most frequently occurred particle size) to facilitate comparison of the data collected for each nanofluid. The data show that using this methodology, the charcoal particles reduced to the nanosized range have monomodal size distributions, centred around a distinct particle size distribution peak. The detected particle distribution peak size and half peak width of the particle size distribution peak are tabulated in Table 6.1. Both the peak size and half peak width vary with the pH values, and the pattern is different for each charcoal sample.

For the WSC nanofluid, the centre of the particle size distribution peak is detected at 1292 nm, 96 nm, and 92 nm for pH 2.0, 7.0 and 11.0, respectively. Interestingly, the detected WSC nanoparticles are distinctively large and widely distributed at pH 2.0, which is indicated by both the peak size and half peak width being more than ten times that detected at pH 7.0 and pH 11.0. While the pH value increases from pH 7.0 to pH 11.0, the determined particle size distribution remains about identical, both in size and size distribution. For the RHC nanofluid, the centre of the particle size distribution peak is detected at 408 nm, 154 nm, and 168 nm for pH 2.0, 7.0 and 11.0, respectively. Also, for the RHC nanofluid, the detected particles appear to be more than doubled in size at pH 2.0. compared to their appearance at pH 7.0 and pH 11.0. While the pH value increases from pH 7.0 to pH 11.0, the centre of the particle size distribution peak is close at 154 nm and 168 nm, with a half-width of the particle distribution peak of 80 nm and 87 nm, respectively. For the AC nanofluid, the centre of the particle size distribution peak is detected at 256 nm, 210 nm, and 254 nm at

pH 2.0, 7.0 and 11.0, respectively. Hence, the particle sizes are close to one another, albeit the half peak width decreases from 362 nm, and 154 nm to 143 nm when going from pH 2.0 to pH 7.0 to pH 11.0, respectively.

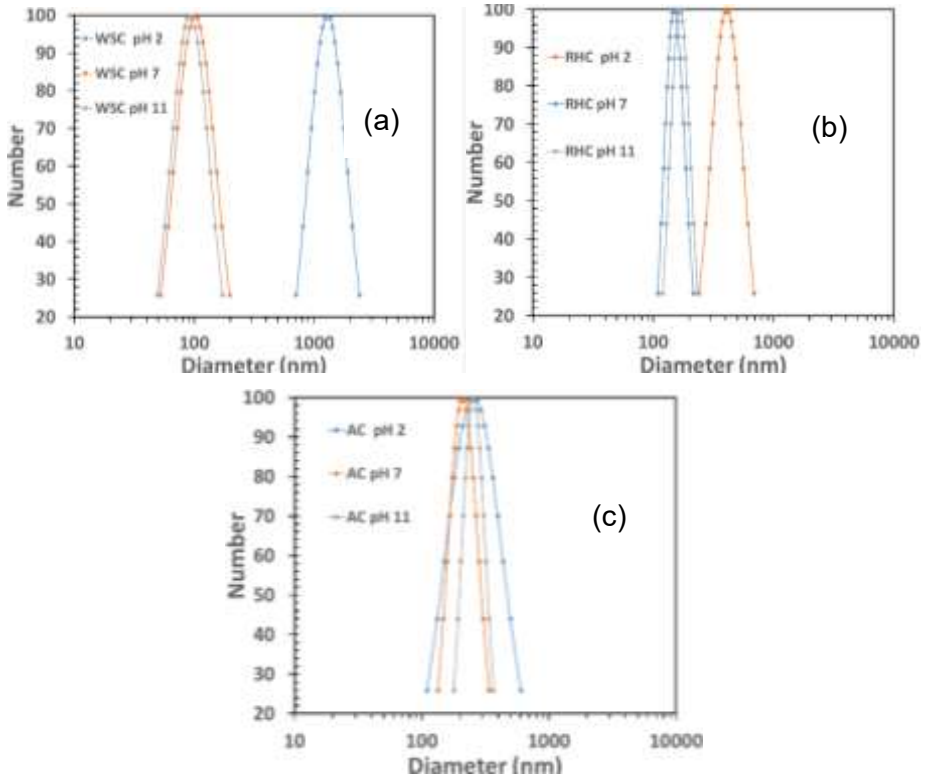

Figure 6.3: Effect of pH values on the normalised particle number size distribution of a) WSC, b) RHC and c) AC determined by Dynamic Light Scattering (DLS).

Table 6.1: The particle distribution peak size (Peak), half peak width (HPW) and ζ-potentials of the charcoal-based nanofluids.

Sample	pH 2.0			pH 7.0			pH 11.0		
	Peak, nm	HPW, nm	ζ-potential, mV	Peak, nm	HPW, nm	ζ-potential, mV	Peak, nm	HPW, nm	ζ-potential, mV
WSC	1292	1271	66	96	108	-115	92	92	-98
RHC	408	336	31	154	80	-110	168	87	-34
AC	256	362	9	210	154	-21	254	143	-30

The curves in Figure 6.4 a and b summarise the variation of the centre of the particle size distribution peak and half peak width with pH value.

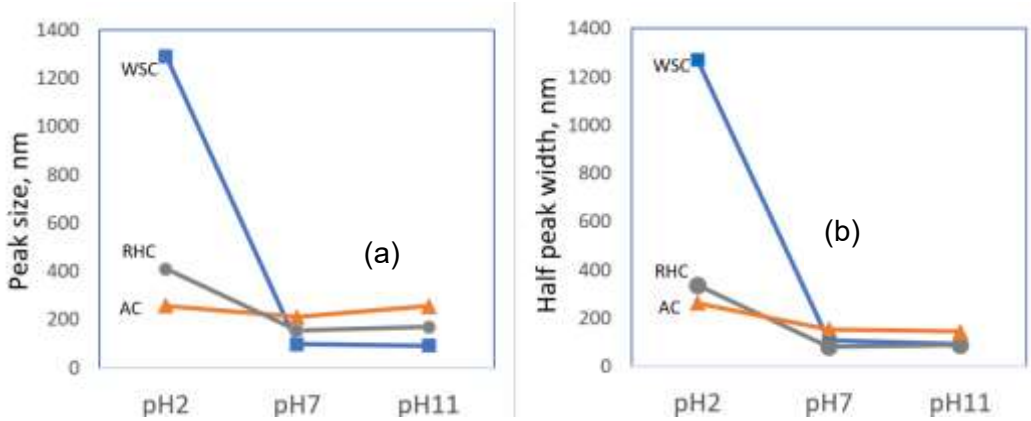

Figure 6.4: The centre of the particle size distribution peak (a) and half peak width (b) at selected pH values determined by Dynamic Light Scattering (DLS).

The above size measurement study at different pH values shows that the large particle sizes detected at pH 2.0 are nanoparticle clusters rather than individual nanoparticles for WSC (1292 nm) and RHC (408 nm) nanofluids even just after the sample for the measurement has been ultrasonicated for one hour. The AC (256 nm) nanofluid at pH 2.0 does include the nanoparticles in a similarly low size range as in the AC samples at pH 7.0 and pH 11.0, but at pH 2.0 the detected particle size distribution is more than twice as wide as that of the samples at pH 7.0 and pH 11.0. These observations align well with the fact that the PH_{pzc} values of WSC (pH 7.4) and RHC (pH 6.6) are higher than pH 2.0, which is a pH value that is distinctively away from their surface neutralisation buffer pH range, while the pH 2.0 is somewhat higher than the PH_{pzc} of AC (pH 1.4), which is starting to enter the surface neutralisation buffer pH range. Therefore, the detected nanoparticle size difference between pH 2.0 and pH 7.0 is much larger for WSC and RHC and is relatively small for AC nanofluids.

These nanoparticle size variations with pH values can be related further to their zeta-potential values, which are also shown in Table 6.1. The zeta potential indicates the charging intensity of the hydrated layer of nanoparticle surface in the fluid. The data in Table 6.1 shows that at pH 2.0, the nanoparticles have positive zeta-potentials of 66 mV for the WSC nanofluid, 31 mV for the RHC nanofluid and 9 mV for the AC nanofluid. Upon a pH increase to pH 7.0, their zeta-potentials become negative, with values of -115 mV for the WSC nanofluid, -110 mV for the RHC nanofluid and -21 mV for the AC nanofluid. At pH 11.0, the zeta-potentials decrease to -98 mV for the WSC nanofluid and -34 mV for the RHC nanofluid at pH 11.0 and increase further to -30 mV for the AC nanofluid. The zeta-potential variation trends with the pH value are

consistent with that of the particle size detected by DLS: the higher the absolute zeta potential value of the hydrated nanoparticles, the smaller the particle size and the narrower the particle size distribution that is detected by the laser beam, suggesting that the nanoparticles separate better when the absolute value of the zeta potential is high, which means that the electrostatic repulsion is high, and so, the particles effectively repel one another thus promoting particle separation.

To enhance the recovery of oil from an oil reservoir, two things can be done: 1) change the surface chemistry of the reservoir by flooding with an EOR fluid that can change the wettability of the rock surface; 2) Change the flow pattern within the reservoir by flooding with an EOR fluid that can improve the sweeping and reduce finger formation within the reservoir.

To test for the wettability of the nanofluid a contact angle analysis is carried out using the methodology described in Chapter 3. This will determine if the dispersion of charcoal into the base fluid (water) altered the interaction with the substrate. The potential for the nanofluid to change the sweeping within the reservoir was analysed by measuring the viscosity change with different nanoparticle types and concentrations and varying nanofluid pH.

6.3. Effect of nanoparticles on surface tension and contact angle

One of the methods of increasing the amount of oil that can be recovered from an oil reservoir is to change the wettability of the rock or/and reduce the surface tension as mentioned in Chapter 2.6.

The surface tension of RHC, WSC, AC, and fresh deionised water was measured at room temperature using the Pendent drop method. The surface tension of deionised water was measured to be about 67.3 mN/m, with the addition of WSC a reduction in surface tension of about 1% (66.6 mN/m) was observed, while with the addition of RHC and AC an increase of about 0.4 and 7.0% (67.0 and 71.9 mN/m), respectively was observed with an error of ±0.3 mN/m.

A variety of surfaces were tested for the measurement of contact angle using the sessile drop method. Glass slides were first selected for the contact angle measurement. Spreading wetting was observed when the liquid came in contact with the solid surface, this was due to the hydrophilic nature of the glass. This was

followed by the use of polypropylene as it is hydrophobic. However, this was not suitable as the surface was not smooth. 12 Glass slides were coated with wax to make them hydrophobic, and the effect was a more adhesion wetting behaviour. The hydrophobic nature plus the ability to control the smoothness of the surface made the treated glass the best solid substrate for contact angle measurement in this study.

The same nanofluids used to measure the surface tension were used to measure the contact angle at room temperature. A reduction in contact angle was observed for all nanofluids when compared to deionised water. The contact angle of deionised water was measured to be about 110.6°. With the addition of char to make up 0.5 wt% solution, the contact angle reduced to about 87.0° for WSC, 108.1° for AC, and 93.2° for RHC. The contact angle is a sign of the hydrophilic/hydrophobic nature of the nanofluid as well as an index of the wettability. If the nanofluid is water-wet/hydrophilic, a contact angle of $\Theta<90°$ will be observed. If the nanofluid is oil-wet/hydrophobic, a contact angle of $\Theta>90°$ will be observed. Therefore a decrease in contact angle means an increase in wettability, which is what is required for an increase in oil recovery. The only variable controlled closely in this experiment was that of the concentration.

Overall, these findings emphasise the potential of charcoal-based nanofluids in modifying rock wettability and reducing surface tension, thus offering promising avenues for enhancing oil recovery from reservoirs. Further exploration of the effects of nanoparticle concentration and other variables on wettability alteration could provide valuable insights for optimising oil recovery strategies.

Table 6.2: The surface tension of deionised water, AC, RHC and WSC at 2 wt% and room temperature/ The contact angle of deionised water, AC, RHC and WSC at 2 wt% and room temperature.

Sample	Contact Angle (°)	Surface Tension (mN/m)
Deionised Water	110.6	67.3
AC	108.1	71.9
RHC	93.2	67.6
WSC	87.0	66.6

6.4. Effect of pH value on the surface tension

An analysis looking at the effect of pH on the surface tension of 2 wt% AC, RHC, and WSC at room temperature, showed that there is a decrease in surface tension with an increase in pH. A reduction in surface tension of about 2.0, 5.0, and 20% for AC, RHC, and WSC, respectively was measured with an increase in pH from 2.0 to 11,0, as shown in Figure 6.5.

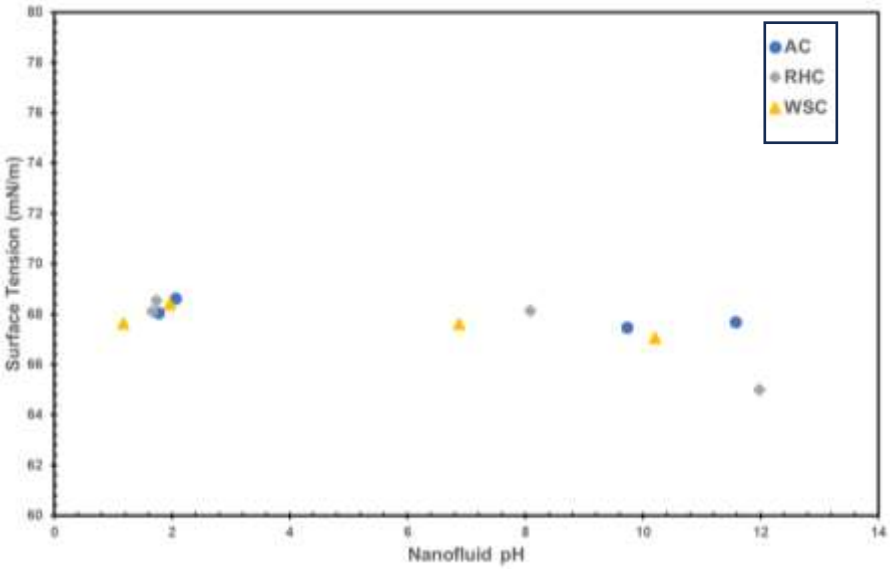

Figure 6.5: The effect of pH on the surface tension of AC, RHC and WSC at 2 wt% and room temperature.

6.4.1. Effect of pH value on the contact angle

Figure 6.6 shows that the contact angle of the nanofluids decreased with an increase in pH, this indicates that as the pH reduces the wetting of the substrate moves towards water-wet. For AC at about pH 1.0, 2.0, 9.0 and 11.0, the contact angles were 89.8°, 93.5°, 69.6° and 37.2°, respectively. RHC at about pH 1.0, 2.0, 9.0 and 11.0 had contact angles of 79.1°, 88,1°, 63.4° and 31.0°, respectively. Finally, at about pH 1.0, 2.0, 7.0, and 10.0 the contact angles that were measured for WSC were 83.2°, 82.2°, 77.8° and 55.2°, respectively.

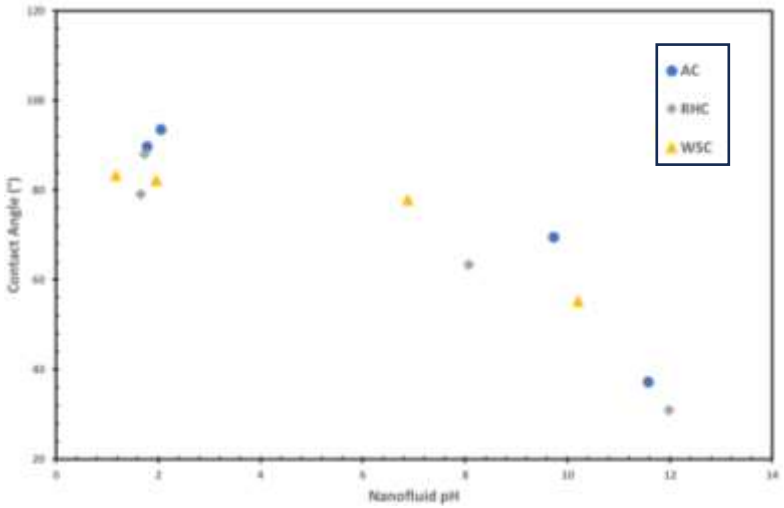

Figure 6.6: The effect of pH on the contact angle of AC, RHC and WSC at 2 wt% and room temperature.

Understanding the behaviour of the nanofluid when the surface charge is neutral, that is at the Point of Zero Charge (PZC) is also crucial, as this gives insights into the nanofluid stability, surg=face modification potentials, rheological properties and surface interactions. As shown in Table 6.3, the surface tension at the PZC is similar for all three samples at about 68 mN/m at the PH_{pzc} with an error of ±0.8 mN/m, while the contact angle shows slight differences.

Table 6.3: Surface tension and contact angle of 2 wt% RHC, WSC, and AC at PHpzc.

Char Type	PH_{pzc}	Surface Tension (mN/m)	Contact Angle (°)
RHC	6.6	67.4	72.0
WSC	7.4	67.7	68.0
AC	1.4	68.1	89.8

6.5. Viscosity of charcoal-based fluids

6.5.1. Effect of pH value on the viscosity

At first, the effect of pH value on the viscosity is studied for the viscosity enhancement of the charcoal-based fluids. Their viscosity changes with pH values are shown in Figure 6.7. The nanoparticle concentrations are 1.3 wt% for the WSC, 0.5 wt% for the RHC, and 0.6 wt% for the AC nanofluids.

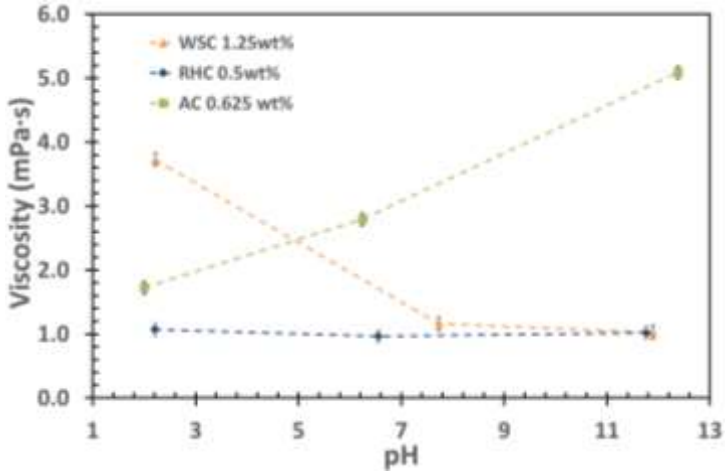

Figure 6.7: The effect of pH values of the nanofluids on their viscosities. The viscosity was measured at 100 rpm and 22°C.

Different trends are observed for the variation of the viscosities of the three nanofluids as a function of pH. For the WSC fluid (1.25 wt%), the highest viscosity value has been found at pH 2.0, which is 3.72 mPa.s. The viscosity significantly decreases to 1.16 mPa.s with a pH value increase to pH 6.0, and then its value slightly further decreases to 1.03 mPa.s at pH 12.0 (Figure 6.7). The viscosity decreases in tandem with the particle size distribution detected by DLS at different pH values, e.g., the centre of the particle size distribution peak being 1292 nm at pH 2.0, 96 nm at pH 7.0 and 92 nm at pH 11.0. The RHC nanofluid (0.5 wt.%) appears to show a small variation in viscosity from 1.09 mPa.s at pH 2.0, 0.96 mPa.s at pH 6.8 to 1.02 mPa.s at pH 12.0. This slight viscosity variation follows the detected particle sizes as well, i.e., 408 nm at pH 2.0, 154 nm at pH 7.0 and 168 nm at pH 11.0.

For the interpretation of the recorded data, it is worth considering that it is well-known that DLS detects moving particles by their scattering of the laser beam. A particle in contact with other particles is measured as one large particle. In a general sense for one given sample, the larger size of the detected particles can be indicative of stronger interactions between the nanoparticles. For the WSC and RHC fluids, the particle sizes detected at pH 2.0 are several times larger than these at pH 7.0 and pH 11.0 (Figure 6.9), suggesting that the larger particle sizes and wider particle size distribution detected by DLS for the same sample at different pH value conditions, is related to stronger interactions between the nanoparticles. This judgment agrees with the absolute value variation of the zeta potential. Both these features observed in the

DLS measurements for the WSC and RHC nanofluids indicate that a stronger interaction between nanoparticles leads to a higher viscosity increment.

The viscosity of the AC nanofluid (0.63 wt%) increases nearly linearly from 1.8 mPa.s at pH 2.0 to 5.2 mPa.s at pH 12.0, while DLS measurements detected similar particle sizes, but increasingly narrower size distributions (see Figure 6.5c) with increasing pH, suggesting increasingly weakening of interactions between the nanoparticles. In this context, it is worth noting that the behaviour of AC is related to it being distinctly different from WSC and RHC for its large specific surface area of 1600 m^2/g and micropore volume of 2 cm^3/g. The large specific surface area results from the richness in micropores, which is less than 2 nm. The micropores are in the size range comparable to the empty channels of carbon nanotubes for the study of pore effects.

6.5.2. Effect of nanoparticle type and content on the viscosity of nanofluids

The three nanofluids of WSC, RHC and AC were examined for the effect of particle concentration on viscosity at pH 7.0. The viscosity measurement was carried out at continuously varied shear rates from 10 to 400 s^{-1}. The effect of shear rate on the viscosity of each nanofluid at different concentrations is depicted in Figure 6.8.

The experimental data in Figure 6.8 shows that at the concentrations examined for all three nanofluids show viscosity enhancement compared to that of the base liquid, deionised water, at the same temperature. Their viscosities show the highest value at the starting shear rate of 10 s^{-1} and then decrease with the shear rate to 100~150 s^{-1}, depending on the nanoparticle concentration. After this shear-thinning range at low shear rate, the viscosity of the nanofluids then tends to be levelled.

The viscosity enhancement increases with the nanoparticle content, but the viscosity increment varies with the particular charcoals in the order: AC > WSC > RHC. At 100 rpm (shear rate 384 s^{-1}), a condition that is commonly used to represent the viscosity of fluids, the viscosities are 2.6 mPa.s for the 1.3 wt% AC and 1.2 mPa.s for the 1.3 wt% WSC, which are 2.9 and 1.4 times that of water, respectively, and the viscosity for the 1.0 wt% RHC nanofluid 1.04 mPa.s, which is 1.2 times of that of water.

The viscosity of the three charcoal-based nanofluids was measured at 100 rpm (shear rate 384 s^{-1}) at pH 6.0 and 22^{o}C for the relationship study of the relative viscosities, the ratio of the effective dynamic viscosity of the nanofluid (η_{eff}) and the

dynamic viscosity of the base liquid (η_{bf}), to the nanoparticle volume fraction, as shown in Figure 6.9a. In the figure, the calculated lines of the modified Chen's equation [98], Equation 2.10 [155], are also included with the best agreement for the Dispersion Factor (DF) being DF=7.0 for the WSC nanofluids, and DF=4.5 for the RHC nanofluids.

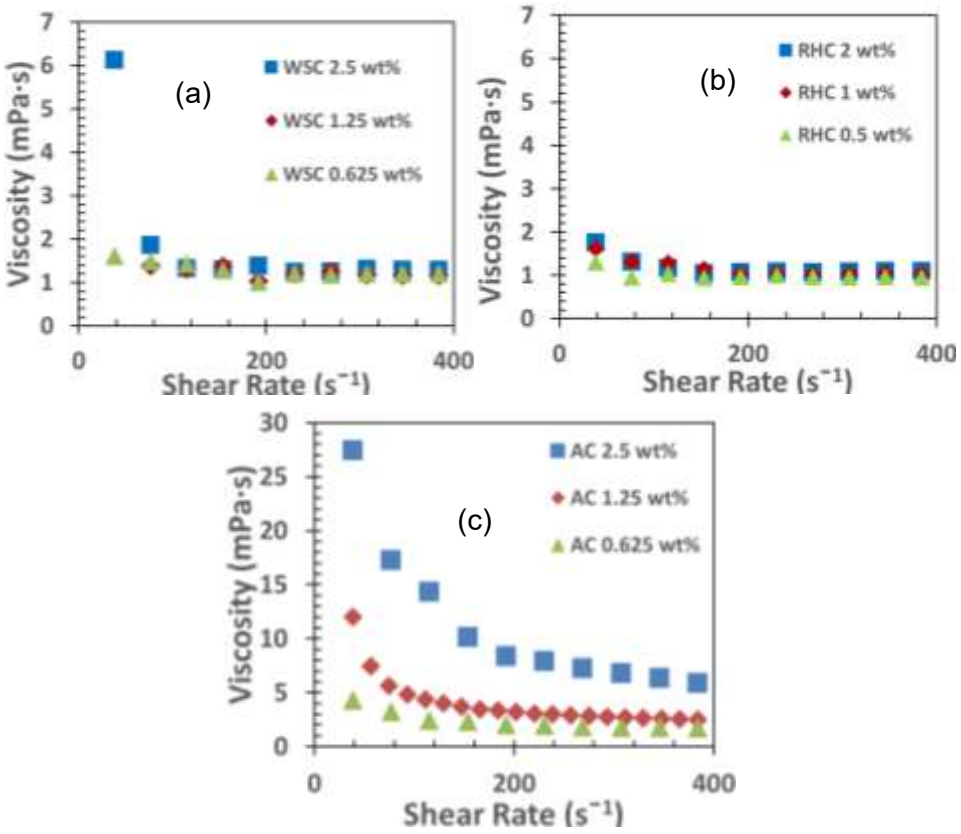

Figure 6.8: The effect of shear rates and nanoparticle concentrations on the viscosity of nanofluids: a) WSC, b) RHC and c) AC. The viscosity measurements were carried out at pH 6.0 and a temperature of 22°C.

The calculation used the assumption that the nanoparticles were spherical, and the ϕ is the nanoparticle volume fraction. The modelling shows a least mean square error of 0.066 for the WSC nanofluids and 0.011 for the RHC nanofluids, which are much smaller than the relative viscosity values of the nanofluids that are larger than 1. It is worth noting that the WSC nanoparticles (92 nm at pH 7.0) having DF =7.0 provide better viscosity enhancement than the best viscosity enhancement achieved by metal oxides with DF=6.6 for silica nanofluids (20 nm) and DF=6.2 for alumina nanofluids (45 nm) [155]. The RHC nanofluids (154 nm at pH 7.0) having DF=4.5 show a

medium viscosity enhancement of metal oxides, comparable to that of the nanofluid of 200-300 nm alumina nanoparticles [155]. The relative viscosity data analysis of the WSC and RHC nanofluids using the modified Chen equation suggests that the nanoparticle size determines the number of interactions between particle and particle as well as between particle and the base liquid, with the nanoparticle surface chemical composition determining the strength of these interactions. It must be emphasised that the combined effect of the interaction number and strength is reflected in the relative viscosity and further in the modelled DF value. The DF is thus an extremely useful and valuable parameter for characterising the effectiveness of the viscosity enhancement that is achieved by using a particular nanofluid. The higher the DF value, the more significant the viscosity increment appears at a given nanofluid concentration.

The relative viscosities of the AC nanofluids varying with the nanoparticle volume fraction are shown in Figure 6.9b. Instead of following the modified Chen equation, the relative viscosity shows an excellent linear relationship to the volume fraction of the AC nanoparticles as shown by Equation 6.1 which is obtained by linear regression of the data.

$$\frac{\eta_{\mathrm{eff}}}{\eta_{\mathrm{bf}}} = 1 + 413.97\varphi, R^2 = 0.9904 \qquad \text{Equation 6.1}$$

where η_{eff} is the effective dynamic viscosity of the suspension (mPa·s); η_{bf} is the base liquid dynamic viscosity (mPa·s) at the same temperature; and φ is the volume fraction of the hard spherical particles suspended in the fluid.

Significantly, by Comparing Equation 6.1 to the Park and Cho expression (Park and Cho, 1998), the viscosity increment of the AC nanoparticles is approximately 10 times higher than that of alumina and titanium oxide nanoparticles.

Among the three nanofluids, the AC nanofluid shows the largest particle size (particle distribution peak size at 210 nm compared to 96 nm for WSC and 154 nm for RHC nanofluids at pH 7.0) and exhibits the most significant viscosity enhancement. This outstandingly high viscosity enhancement of the AC nanofluid can be related to both its richness in oxygen content and polar/hydrophilic functional groups, as shown by the ultimate and FTIR analysis, and more apparently in micropores that are in the

range of the hollow structure of carbon nanotubes (~2 nm). Similar to active carbon, carbon nanotubes dispersed in water normally have a hydrophilic surface [156].

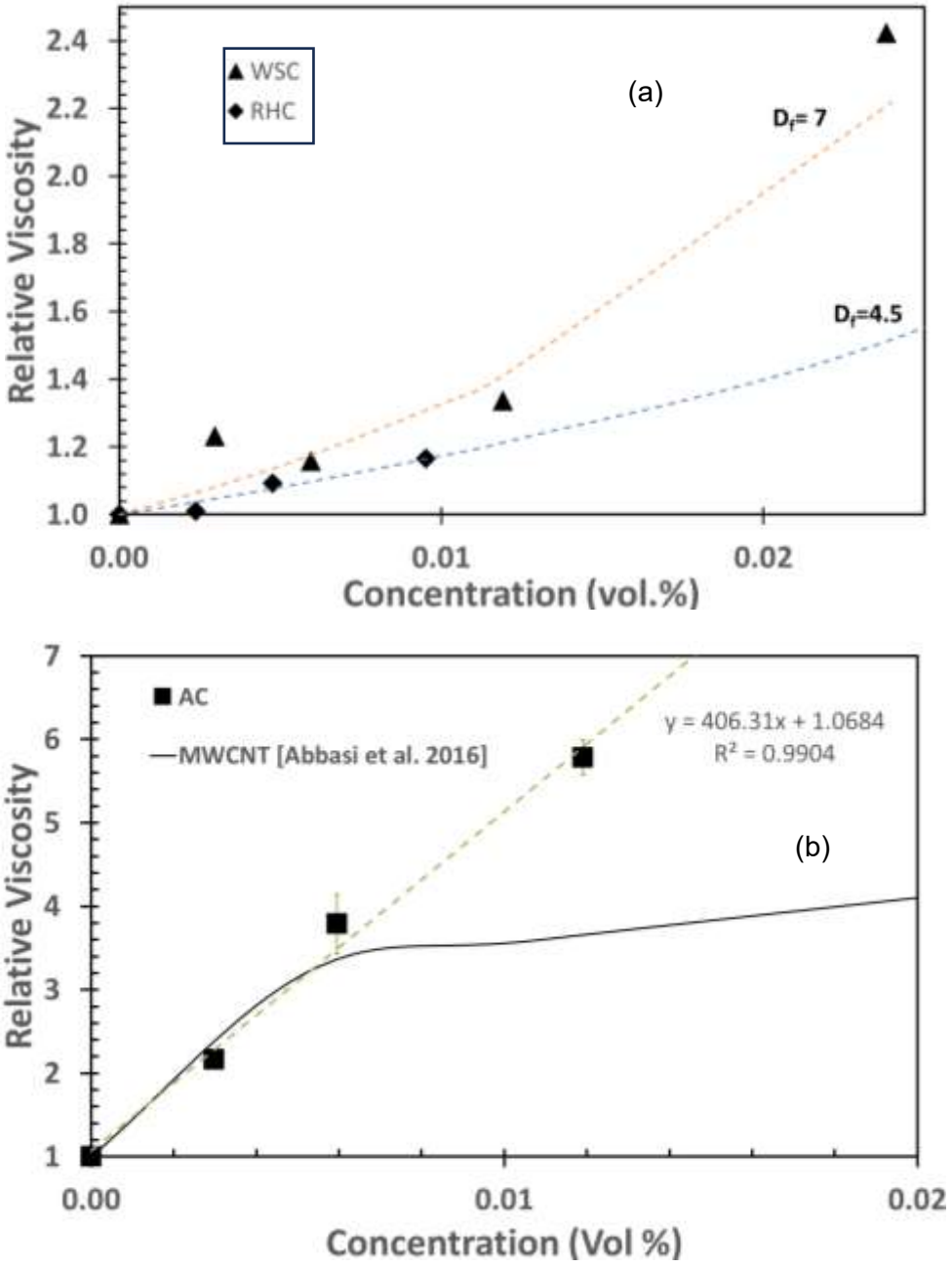

Figure 6.9: Relative viscosity of nanofluids versus nanoparticle volumetric fraction: (a) experimental data of the WSC and RHC nanofluids compared to the calculated values using the modified Chen equation (the dotted lines) and (b) the AC nanofluids (the solid square with the regression line) compared to that of carbon nanotube nanofluids (the solid black line). The viscosity was measured at pH 6.0, 100 rpm and 22ºC.

To afford further analysis, the viscosity increment of the AC nanoparticles is compared to that of multiwall carbon nanotube (MWCNT) nanofluids in Figure 6.9b, showing very much identical viscosity enhancement for both AC and MWCNT, when the volume content of MWCNTs is below 0.6 vol.% [95], which is much higher than that usually achieved with metal oxide (e.g., TiO_2, γ-Al_2O_3 and SiO_2) nanoparticles [155]. However, [69] found rather high viscosities for some silica nanofluids. They studied the viscosity of nanofluids of porous silica nanoparticles (22 nm with a specific area of 370 m^2/g). The nanofluids of 0.01, 0.05, 0.1 or 0.5 wt% in the brine of 3 wt% of NaCl showed viscosities of 1.009, 1.067, 1.160 and 1.347 mPa.s, respectively. These viscosities are significantly higher than that reported for other silica nanofluids reported [104, 144]. The outstanding viscosity enhancement is believed to have resulted from a so-called pore effect; this is another indication of the importance of the porosity of the nanoparticles constituting the nanofluid in generating high relative viscosity values.

Returning to Figure 6.9b, it is important to underline that when the nanoparticle volume content is higher than 0.6 vol.%, the MWCNT fluids do not show significant further relative viscosity increase while the AC fluids show a proportional further viscosity increase following Equation 4.1. An analysis of these various experimental results suggests that the highly porous structure of both the MWCNT and AC nanoparticles and their nanoparticles' free movement in the fluid are critical for the generation of the observed significant viscosity enhancement. The AC nanoparticles are nanosized in three dimensions (3D nanomaterial) while MWCNT is considered to be a 2D nanomaterial for the carbon nanotube's length, which can be a few magnitudes larger than its diameter of ~2 nm. The high aspect ratio of MWCNT facilitates entanglement of individual MWCNT entities which would limit further viscosity enhancement at a MWCNT concentration higher than 0.6 vol%. At a higher concentration, the 3D nanosized AC particles can move more freely in the nanofluid than is possible for equally concentrated MWCNT in the nanofluids, so that AC's viscosity increment continues to occur when the AC concentration is over 0.6 vol.%. The consequence is that nanofluids of the highly porous AC nanoparticles show a similar viscosity increment to MWCNTs due to their similarly high porosity when the content is less than 0.6 vol.%. However, the situation changes in favour of AC at a higher concentration as the 3D nanosized AC particles can move more freely in the

nanofluid than is possible for MWCNT, so that AC's viscosity increment continues to go on up to a much higher concentration, which reaches up to 1.2 vol.% as shown in Figure 6.13b, the highest volume fraction measured in this study. The reason and origin of the upward trend of the relative viscosity appears to be clear, though more work needs to be carried out to examine the upper limit that can be reached. Both the porosity and shape (reflected in aspect ratio) of nanoparticles are critical factors for their role in enhancing viscosity. Similarly, the larger amount of micropores included in WSC than RHC may be the reason that the WSC nanoparticles enhance viscosity better than RHC and nonporous metal oxide nanoparticles. However, the nanofluid of the more porous AC shows a striking viscosity enhancement.

6.6. Conclusion

The selected nanoparticles were dispersed into deionised water and milled to reduce their size. The effect of pH on the size distribution showed that both the peak size and half peak width vary with the pH values, and the pattern is different for each charcoal sample. For the WSC nanofluid, the centre of the particle size distribution peak is detected at 1292 nm, 96 nm, and 92 nm for pH 2.0, pH 7.0 and pH 11.0, respectively. For the RHC nanofluid, the centre of the particle size distribution peak is detected at 408 nm, 154 nm, and 168 nm for pH 2.0, pH 7.0 and pH 11.0, respectively. For the AC nanofluid, the centre of the particle size distribution peak is detected at 256 nm, 210 nm, and 254 nm at pH 2.0, pH 7.0 and pH 11.0, respectively. It was determined that the size increase around pH 2.0 is cluster formation rather than individual nanoparticles for wheat straw char and rice husk char. This falls in line with their pH_{pzc} pH 7.4 and pH 6.6, respectively. Although the active carbon has similar nanoparticle size at all three pH values, a larger particle size distribution was detected at pH 2.0, the larger particle size distribution was due to pH_{pzc} of 1.4 for active carbon. The variation in nanoparticle size was also related to the zeta potential for all three samples. At pH 2.0 wheat straw char, rice husk char and active carbon have a positive zeta potential of 66, 31 and 9 mV, respectively. With a pH increase to pH 7.0, their zeta-potentials become negative, with values of -115 mV for the WSC nanofluid, -110 mV for the RHC nanofluid and -21 mV for the AC nanofluid. At pH 11.0, the zeta-potentials decrease to -98 mV for the WSC nanofluid and -34 mV for the RHC nanofluid at pH 11.0 and increase further to -30 mV for the AC nanofluid.

It has been known for a long time that adding a small number of nanoparticles to a base liquid causes a viscosity increase. This viscosity increase is explained via the relative viscosity by the equations of [85-87].

In this research, concentration-dependent relative viscosity data for TiO_2, γ-Al_2O_3 and SiO_2 nanofluids have been selected from the open literature, and the data has been subjected to the various reported theoretical and empirical equations. However, it appeared that the experimentally measured values of metal oxide nanofluids tend to be significantly higher than the calculated ones in the particle volume content range studied (< 5%). Though the Pak and Cho equation [88], an empirical equation, reproduces the higher-end values of the experimental measurements to some extent, it is however rather unsuccessful in modelling the large number of experimental data whose values are lower than the higher-end values towards that estimated by, e.g., the Einstein equation. The new theoretical treatment using the adaptation of Chen's equation [106] with the newly defined Dispersion Factor (DF) yielded a much better agreement with the wide range of experimental data. The DF value comprehensively includes the number and magnitude of the interactions between the nanoparticles themselves and with the base liquid and thus reflects the strength of these interactions. It enables to guide relevant practical work towards the directed obtaining of nanofluids with a desired, predetermined behaviour just by measuring viscosity enhancement, e.g., to examine the dispersity of nanoparticles in a working condition of the fluid rather than by the more elaborate method of using TEM in a dry state or DLS in an extensively diluted state.

By assigning the DF with a series of numerical values from 1 upwards, the literature data can be represented by the lines calculated with a DF value using the modified Chen equation. The DF values comprehend the effect of particle size/shape, and chemical composition via the interactions of particle surface (including pores) to the base liquid and particle to particle on the viscosity of the nanofluid. A larger DF value represents a stronger influence of the nanoparticles on the viscosity increment.

The DF is therefore a significant parameter describing the combined particle interactions and particle aggregations in nanofluids. Importantly, its value can be experimentally determined, which also means that it can be experimentally tailored and tuned to suit an application for which the nanofluid will be designed.

The DF analysis using the adapted Chen equation with the DF [155] shows that the WSC nanoparticles (with a size distribution peak located at 96 nm) have a DF value of 7.0, which corresponds to a zeta-potential of -117 mV and strong interactions to the base liquid. The RHC nanoparticles (with a size distribution peak located at 154 nm) have a DF value of 4.5, corresponding to a zeta potential of -115 mV. The DF values comprehensively reflect the effect of nanoparticle population (particle sizes) and interaction strength of the nanoparticle surface to the base liquid on the one hand and nanoparticle-to-nanoparticle interactions on the other hand. The study shows that charcoal-based nanofluids give rise to better viscosity increments (DF=7.0 for the WSC nanofluids) than that of metal oxide nanoparticles reported in the literature (DF=6.6 for silica nanofluids) [155].

The AC nanoparticles show a much more significant viscosity increment than the WSC and RHC nanoparticles, and the increment is comparable to that of carbon nanotubes at a concentration of <0.6 vol.%. As the nanoparticle concentration is higher than 0.6 vol.%, the AC nanoparticles show continuously proportional viscosity enhancement following a linear equation for its 3D nano size. The proportional viscosity enhancement of the AC nanofluid is about 10 times higher than that of γ-alumina or titanium oxide nanoparticles. This shows that charcoal nanoparticles can provide better viscosity enhancement than metal oxide nanoparticles, and the viscosity enhancement can be adjusted by pH values.

7. Chapter 7: Enhanced Oil Recovery of the Charcoal-Based Nanofluids

7.1. Introduction

Enhanced oil recovery (EOR) techniques play a pivotal role in maximising hydrocarbon extraction from reservoirs as highlighted in Chapter 2, particularly in mature and unconventional fields where conventional methods prove inadequate. In recent years, nanotechnology, such as the the use of SiO_2 [26], TiO [27] and Al_2O_3 [70] nanoparticles dispersed in base fluids such as water [28] and surfactants [24] has emerged as a promising avenue for revolutionising EOR strategies, offering innovative solutions to enhance oil recovery rates and optimise production efficiencies. Among the diverse array of nanomaterials explored for EOR applications, carbon-based nanofluids have garnered significant attention due to their unique physicochemical properties and versatile functionalities.

Carbon-based nanofluids, including carbon nanotubes (CNTs), graphene oxide (GO), and multi-walled carbon nanotubes (MWCNTs), have been extensively investigated for their potential in augmenting oil recovery processes. These nanomaterials possess exceptional mechanical strength, high surface area, and surface chemistry, making them ideal candidates for altering fluid-rock interactions, reducing interfacial tension, and improving fluid mobility within reservoirs.

A growing body of research has revealed the efficacy of carbon-based nanofluids in enhancing oil recovery mechanisms through a multifaceted approach. Studies such as those by Soleimani et al. [157] and Pandey et al. [158] have delved into the preparation, characterization, and application of carbon nanotube-based nanofluids, highlighting their potential for reducing interfacial tension and modifying reservoir wettability to facilitate enhanced oil displacement.

Furthermore, investigations by Jafarbeigi et al. [159] and Gómez-Delgado et al. [160] have explored the role of functionalised graphene oxide nanoparticles in wettability alteration and oil recovery enhancement, shedding light on the intricate interplay between nanofluid properties and reservoir behaviour.

Building upon these foundational studies, this chapter will focus on the performance of WSC and RHC nanofluids prepared and characterised in Chapter 6, in sectional flooding for enhanced oil recovery.

To mimic industrial operations, cylindrical packed columns are used to mimic the porous reservoirs, the cores that are carefully prepared and loaded with brine and crude oil (as original oil in place (OOIP)) for water flooding. After water flooding, sectional nanofluid flooding is carried out and then followed by water flooding again to examine the performance of the nanofluid in enhancing oil recovery (EOR).

7.2. The core and flooding rig design

Oil reservoirs are complex large non-uniform systems that consist of fluids (oil, gas, brine) and rocks, and the fluids co-exist in the non-uniform porous rock formation. To prepare cores to present such a complex and large system for meaningful experimental data of enhanced oil recovery, the core diameter and length need to be carefully considered to avoid short-cut at the wall (boundary effect), and to ensure that the flow pattern of the flooding fluid in the core are out of the influence zone of entry effect.

The boundary effect, in the context of fluid flow through porous media, pertains to the influence of the particle size of the packing material on the flow dynamics. This effect becomes particularly significant when the size of the particles approaches the size of the channel through which the fluid is flowing. Ergun's equation, from a particle-centric perspective, suggests that maintaining a sufficient diameter ratio between the column (or channel) and the packing particles is crucial for minimizing this boundary effect [161]. Specifically, when the diameter ratio of the column to the particle exceeds a certain threshold, typically cited as 10, the impact of the boundary layer on fluid flow diminishes.

In this study, the selected packing material comprises sand particles with an average diameter of 250 μm. To adhere to the diameter ratio requirement proposed by Ergun's equation and effectively mitigate the boundary effect, the diameter of the column must exceed 2.5 mm. Consequently, a column with an inner diameter of 20 mm was chosen for this investigation. This diameter exceeds the minimum diameter ratio requirement by a considerable margin, being 40 times larger than the critical threshold. By adopting such a substantially larger column diameter relative to the

packing particle size, the boundary effect is effectively minimized, ensuring that fluid flow through the porous medium remains largely unaffected by the proximity of the channel walls.

The entrance effect occurs when the fluid is pumped into a column, at first the velocity profile is flat, but as it moves downstream the wall effect kicks in within the the column. The velocity profile in the tube will be developed and gradually remains unchanged. The length required for the flow to become fully developed is known as the entrance length [161], which has to do with the Reynolds number of the flow and the column diameter. The superficial velocity is calculated to be 9.55 $x10^{-5}$ m/s. Assuming 60% of the core is occupied by sand meaning the pore volume is about 40%, the cross-sectional of flow area will be 1.26 $x10^{-4}$ m/s resulting in a pore velocity of 2.39 x 10^{-4} m/s.

Considering the boundary and entrance effects, a cylindrical pipe with dimensions 300 mm by 20 mm and a volume of 94 mL made out of copper was used as the core, the diameter is over 10 times greater than that of the sand diameter which would reduce the boundary effect. The copper pipe is capable of withstanding the pressure exerted on it when packed. Copper has a corrosion resistance, although not as good as stainless steel but the ease of obtaining the pipe is a lot easier and the surface hardness of the copper helps resist wear. Copper has a high heat conductivity compared to stainless steel but both materials can be used, however, for this experiment, a copper pipe will be used as it is readily available and cut to size. A sintered disc was placed on either end of the pipe to act as a plugs and to allow material to enter through its pores. The core holder was placed horizontally to ensure that the gravitational force would not affect the flow of fluid along the pipe. The length of 300 mm is 15 times that of the diameter which considers the entry length. The flooding rig was designed to consist of 3 storage tanks, one for each fluid that would be flooded (oil, water and nanofluid). As shown in Figure 7.1.

The core was conditioned to a temperature of 50°C and the temperature was kept constant during the flooding process, with an injection rate of 1.8 mL/min for the injection of brine, oil and nanofluid into the cores. This was done to mimic an oil reservoir.

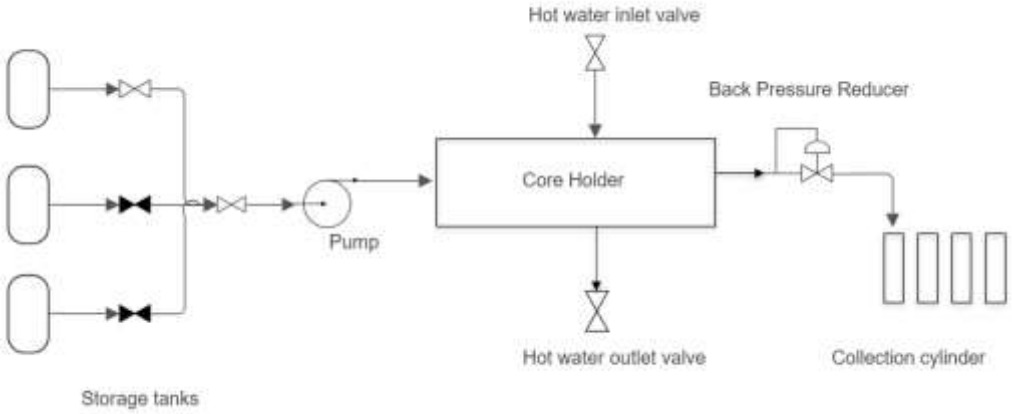

Figure 7.1: A schematic drawing of the flooding rig.

Crude oils are complex mixtures of hydrocarbons and chemicals like paraffins, naphthenes, asphaltenes and resins. Both paraffins and asphaltenes have a high molecular weight, leading to the wax appearance (Cloud Point) of crude oil at low temperatures. The appearance of the crude oil was observed from 20 – 50°C, it was noted that the clouding point of the crude oil used in this research was 45°C. The temperature of an oil reservoir varies from location to depth; they can be as low as 50°C to 260°C [162]. In this study, a temperature of 50°C was used. The fluids were pumped in a peristaltic pump at an injection rate of 1.8 mL/min and a back pressure reducer was used to keep the pressure constant throughout the core.

7.3. Core packing

Sandstone-dominated reservoirs account for about 60.0% of the oil reservoirs found in the world [163]. In this study, sand with quartz (silica) as the major component was selected to pack the Ø20x300 mm core to mimic this type of core for flooding tests. The selection of the sand determines the reservoir wall as a water-wet surface, while the pore size and porosity of the core are determined by the size and size distribution of the selected sand. The sand samples were collected using the cone and quartering method, the method of collection was to make sure every sample taken was representative.

Table 7.1 presents the results of the sieving analysis conducted on the sand utilised in the study. The analysis reveals that the size distribution of the sand particles predominantly falls within the range of 150 to 500 µm, with a notable concentration

observed around the 250 μm mark. This concentration represents a peak in the distribution, indicating that a significant portion of the sand particles possesses a diameter close to 250 μm. Such insights into the particle size distribution are crucial for understanding the characteristics of the packing material and its influence on fluid flow dynamics within the porous medium.

Table 7.1: Particle size distribution of the selected sand.

Mesh Size	US Mesh Opening (μm)	Mass (g)	Mass (%)	Cumulative Mass (%)
>20	>841	0.2	<0.1	0.0
20-30	500	0.7	0.1	0.2
30-40	400	6.00	1.2	1.4
40-60	250	297.6	59.5	69.9
60-80	177	167.7	33.5	94.4
80-100	149	21.5	4.3	98.7
100-120	125	6.4	1.3	100.0
	Total Mass	500.0	100.0	

The packing of the sand into the cores needs to achieve a desired porosity that is in the range of real sandstone oil reservoirs, which is about 15-35% [164], and to be carried out in a way for repeatable and reliable results. The factors that need to be considered for particle packing include the particle size, size distribution, shape, density and nature of the material and surface. The sand selected has a wide particle size distribution in micrometres and irregular particle shapes. A representative packing of uniform spherical particles gives a porosity of ~36%. To reach a packing porosity lower than 36%, dense parking is required. To achieve a dense packing, the interlocking of the particles needs to be controlled or ideally, avoided. This is achieved by controlling the uniformity of the sand particles and adding a small amount of the sand each time into the column after which the column is vibrated.

Table 7.2 delineates the experimental findings that establish a method for achieving a densely packed bed within the core samples. Specifically, it was determined that striking the core at a height of 4.0 mm, repeated 100 times within a 60-second

timeframe, yielded the desired packing density. This standardised method was systematically applied to all core samples investigated in this study. By employing this consistent and controlled approach across all experiments, researchers can ensure uniformity in core packing, thereby enhancing the reliability and reproducibility of the experimental results obtained.

Table 7.2: Process of determining sand packing methodology.

	Core #1	Core #2	Core #3	Core #4
Weight of core (g)	168.9	168.7	167.6	168.8
Weight of core + sand (g)	296.3	295.5	296.0	296.8
Height of hit (mm)	2.0	2.0	4.0	4.0
Time (sec)	60.0	30.0	60.0	30.0
Number of hits	100.0	100.0	100.0	100.0
Density of bed (g/mm^{-3})	0.89	0.91	0.94	0.93

A total of 23 cores were packed for this research, with the first 4 cores being test cores and not mentioned in the results below. The porosity of the 23 cores was calculated by the sand weight and real density of the sand as dry porosity and measured by the water replacement method as described in Chapter 3 and summarized in Table 7.3.

The measured porosities are all within the range expected for a sandstone reservoir at about 40% with the lowest porosity for the calculated being core #13 (33.1%) and the highest being core #18 (43.7%), for the measured core the lowest was core #6 (32.9%) while the highest was cores are # 10 and 11 (42.1%). Taking this into consideration the mean of both the calculated and measured porosity was calculated, the calculated porosity was 37.6%, while the measured porosity was 37.2%, respectively. A difference of 0.3 % was observed. Finally, the standard deviation (SD) was analysed, the calculated porosity has an SD of 2.7 while the measured porosity was 2.5. This shows that both calculated and measured porosities are comparable.

Permeability serves as a crucial parameter for assessing the reservoir's capacity to transmit fluids, acting as the constant in Darcy’s Law, as described by Equation 3.3. This law relates the flux of fluid flow to the pressure drop across a unit length and unit viscosity of the fluid, under conditions devoid of gravitational or hydraulic forces. In essence, permeability hinges on the interplay between porosity and the porous

medium's interaction with the fluid under minimal hydraulic pressure. Notably, oil reservoirs exhibit both primary and secondary permeability. Primary permeability originates from sediment rock deposition processes, whereas secondary permeability arises from alterations in the rock matrix due to phenomena such as compaction, fracturing, and dissolution. Understanding these permeability dynamics is essential for comprehending fluid flow behaviours within reservoirs and optimising hydrocarbon recovery strategies.

Table 7.3: Measured and calculated porosities of the cores# 5-23 packed with sand.

Core#	Calculated Porosity (ø)	Measured Porosity (ø)
6	36.5	32.9
7	36.4	34.9
8	37.7	33.8
9	37.0	40.6
10	37.1	42.1
11	37.1	42.1
12	36.6	34.9
13	33.1	38.4
14	36.5	38.4
15	42.2	39.7
16	33.9	36.4
17	37.3	34.9
18	42.7	35.7
19	34.0	36.8
20	37.0	37.2
21	41.2	37.5
22	41.2	38.0
23	41.2	36.9

In this study, the permeability of the packed core is measured by first loading deionised water into the horizontally arranged core, as shown in Figure 7.1. The height at which the effect of hydraulic pressure starts to become negligible is determined as shown in Figure 7.2.

Figure 7.2 illustrates the impact of hydraulic pressure, represented here by height, on the permeability of the packed core. Notably, heights above 7 cm exhibit a significant influence of hydraulic pressure on permeability, with a recorded permeability of approximately 2.3 x 10^4 mD at a height of ~18 cm. Conversely, at a height of 0.8 cm, the calculated permeability stands at approximately 978 mD. Even at this relatively lower height, the effect of hydraulic pressure, albeit minimal, still influences fluid flow into the core. However, measuring permeability accurately below a height of 0.8 cm poses challenges. The permeability of Core #7 provides valuable insights into the behaviour of the oil displacement process within the core, crucial for understanding enhanced oil recovery mechanisms and optimising production strategies. Consequently, for core #7, the permeability is inferred to be < 978 mD. This value aligns with the typical permeability range observed in oil reservoirs, which spans from about 0.1 to 1000 mD in real-world scenarios [165].

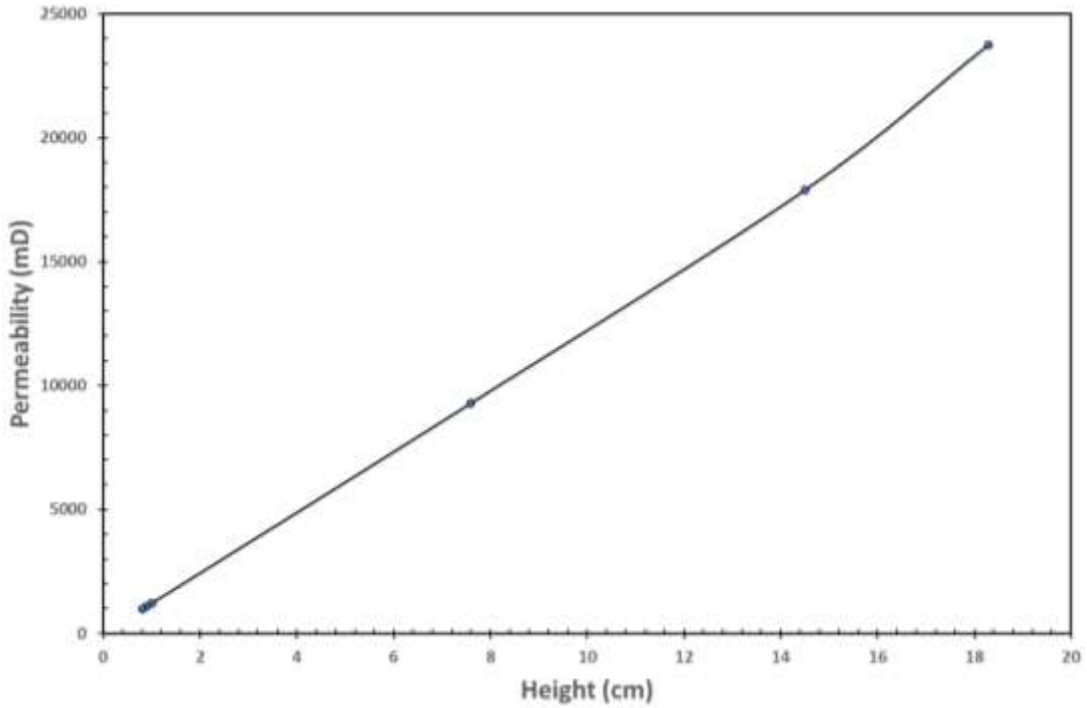

Figure 7.2: Effect of hydraulic pressure (represented by height) on the permeability of core #7.

Table 7.4: The pore volume, porosity, and permeability of the packed cores

Core #	Pore volume, ml	Porosity, (%)
5	31.2	35.0
6	31.0	32.9
7	32.9	34.9
8	31.8	33.8
9	38.2	40.6
10	39.7	42.1
11	39.7	42.1
12	34.8	36.9
13	38.3	40.7
14	38.4	40.7
15	39.7	42.1
16	36.4	38.6
17	34.9	37.0
18	35.7	37.8
19	36.8	39.0
20	35.1	37.2
21	35.3	37.5
22	35.8	38.0
23	34.8	36.9

7.4. Crude Oil loading

The packed core undergoes oil loading following the injection of the synthesized brine, as detailed in Chapter 3, aimed at wetting the sand surface and saturating the core pores. Oil injection occurs at a constant flow rate of 1.8 ml/min. Upon oil injection, displacement of the brine within the core commences, with the brine being initially observed in the measuring cylinder after approximately 3 minutes of oil

injection, as illustrated in the insert in Figure 7.3. Subsequently, a transition occurs, with both oil and brine being collected for about 5 minutes, followed by an exclusive collection of oil after approximately 7-14 minutes, as depicted in the insert in Figure 7.3. This process signifies the penetration of oil into the core and the displacement of brine, marking a critical phase in the oil loading procedure.

This operational procedure is designed to simulate real-world reservoir conditions by preparing the core with scattered brine and oil, mimicking the natural distribution found in reservoirs. Effluent is collected and metered using a measurement cylinder to quantify the volumes of both brine and oil flowing out of the core. These collected volumes are then plotted against the volume ratio of the injected oil volume to the pore volume of the core (PV), yielding what is commonly referred to as the oil loading curve. Core #7 has been singled out as a representative core due to its significant oil-in-place post-oil loading, registering at 27 mL, which corresponds to approximately 82% of the pore volume. The oil-loading curve of Core #7 provides valuable insights into the behaviour of the oil displacement process within the core, crucial for understanding enhanced oil recovery mechanisms and optimising production strategies. Figure 7.3 illustrates the oil-loading curve of Core #7, highlighting its pivotal role in the study.

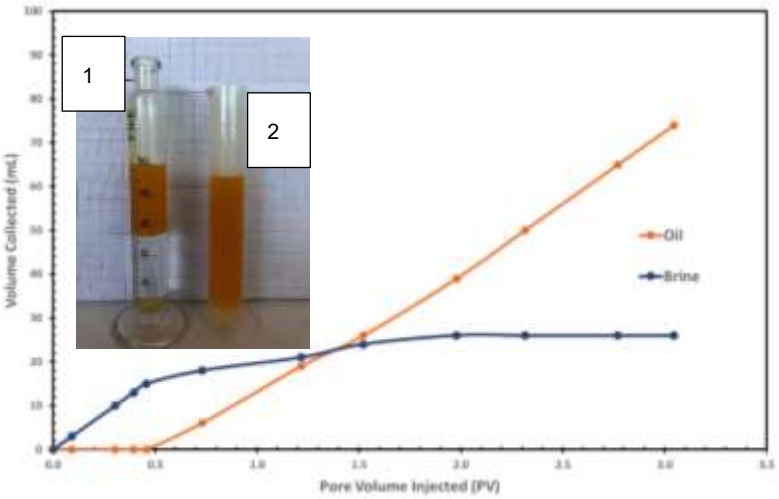

Figure 7.3: The oil loading curve of the Core #7: Pore volume= 32.9 mL. The inset shows the total brine and oil collected, starting with measuring cylinder 1 where the brine and oil collected can be seen. Measuring cylinder 2 shows the remaining oil collected.

When oil is injected to replace the saturated brine, the brine comes out first by the time about 0.45 PV of oil is injected and then the first drop of oil appears. The injection time of the first drop of oil observed is recorded as the oil breakthrough time, which is 14 minutes for the oil loading of Core #7. After that, the brine and oil flow out as a mixture by the oil injection of 2 PV, of which the brine's composition is constantly higher at 0.45-1.5 PV than at 1.5-2 PV. At the end of the oil injection of 2 PV, the volume of the brine collected is 27 ml. To double-check the amount of brine collected, the samples were collected cumulatively into a thin long measuring cylinder, which is equivalent to the volume of oil that has been loaded into the core. In this case, core #7 has the original oil in place (OOIP) of 27 ml, or about 79.0% of the pore volume, with a pore volume and porosity of Core #7 being 32.9 ml and 34.9%, respectively. The inset in Figure 7.3 shows the collected effluent for the oil loading of Core #7.

The oil-loading curves of Core #5-23, i.e. in a total of 19 cores, are shown in Appendix A. It can be seen that the injected oil breaks through at ~0.45 PV and reaches saturation before 2 PV. The saturated oil volumes are around 27 ml to 13 ml, which means the OOIP in the cores is larger than 56.0% (Group A) or lower than 54.0% (Group B). Looking at the oil breakthrough time in minutes recorded, one can find that Group A showed a longer oil breakthrough time with an average of 14 ± 2 minutes, while Group B showed a shorter oil breakthrough time with an average of 9 ± 1 minutes.

In the experimental setup with constant injection rates, the oil breakthrough time serves as a reflection of the movement pattern of injected oil against the brine within the core. Due to inherent mobility differences between brine and oil, the advancing front line of injected oil within the core does not exhibit a plug-flow behaviour, as depicted in Figure 7.4a. Instead, it tends to form viscous fingers, as illustrated in Figure 7.4b. The extended oil breakthrough time observed in Group A indicates that the injected oil requires more time than Group B to develop viscous fingers and reach the output point. The only variables not accurately controlled during the oil-loading runs are the sand-packing and the porous structure within the core. These factors likely contribute to the disparity in oil breakthrough time and Original Oil in Place (OOIP). The presence of additional or larger pore channels within the packed core may facilitate the quicker formation of oil shortcuts or fingers, leading to a shorter oil

breakthrough time. Conversely, a longer oil breakthrough time suggests a more uniform pore structure within the core.

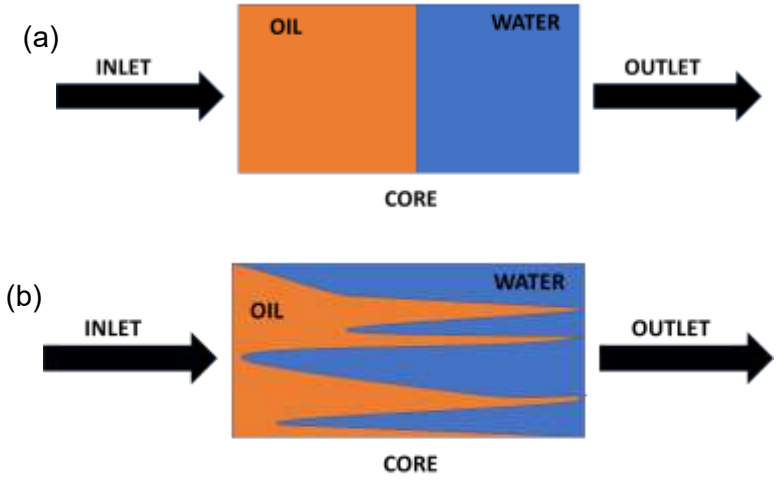

Figure 7.4: Flow pattern of the loading oil in the core a) plug flow; b) viscous finger formation.

The experimental results of the oil breakthrough time and OOIP of the 19 cores are summarised in Table 7.5 together with their corresponding porosities.

Table 7.5: Porosities, Oil break-through time and OOIPs of the oil-loaded cores.

Core #	Pore volume, ml	Porosity (%)	Oil break-through time, min	OOIP, ml	Group
5	31.2	35.0	7	13.0	B
6	31.0	32.9	9	17.0	B
7	32.9	34.9	14	27.0	A
8	31.8	33.8	14	26.0	A
9	38.2	40.6	14	26.0	A
10	39.7	42.1	13	26.0	A
11	39.7	42.1	12	22.5	A
12	34.8	36.9	9	18.0	B
13	38.3	40.7	14	27.0	A
14	38.4	40.7	14	26.0	A

Table 7.5 continues Porosities, Oil break-through time and OOIPs of the oil-loaded cores.

Core #	Pore volume, ml	Porosity (%)	Oil break-through time, min	OOIP, ml	Group
15	39.7	42.1	15	27.0	A
16	36.4	38.6	15	27.0	A
17	34.9	37.0	14	26.5	A
18	36.8	37.8	15	27.0	A
19	35.3	39.0	14	18.0	A
20	32.9	37.2	9	26.0	B
21	31.8	37.5	9	26.0	B
22	34.8	38.0	9	18.0	B
23	38.3	36.9	9	27.0	B

7.5. Water flooding of the oil-loaded cores

Water flooding is the second stage of oil recovery, where water is injected into the oil reservoir from the injection well to increase the pressure towards the production well. In this study, the water flooding combines the first stage of oil recovery, and was carried out after the crude oil was saturated in the packed core under conditions of the water flow rate at 1.8 mL/min, the back pressure reducer (BPR) set at 2 turns, and 50°C. The amount of oil collected is recorded over time to determine the oil remaining in place after secondary flooding.

After heating the core to 50°C and allowing it to stabilize for 24 hours to ensure a uniform temperature throughout, deionized water was injected into the saturated core at a predetermined speed. Within approximately one minute of water injection, the first drop of oil was collected, as depicted in the inset of Figure 7.5a, with measuring cylinder 1 being the first to collect the effluent. The orange fluid visible at the top represents the collected oil, while the clear fluid at the bottom denotes the collected brine. For core #7, the collection of only oil continued for about 8 minutes, after which a mixture of oil and water was observed. Over time, the amount of oil collected decreased while that of water increased until no more oil was detected. Figure 7.5a illustrates the water flooding curve alongside effluent images of Core #7. The effluent

image reveals that the majority of the oil is recovered within the first 25 mL of water injected into the core, resulting in a total recovery of approximately 48.0% of the original oil in place, equivalent to 27 mL. Consequently, about 14 mL, or approximately 52.0% of the original oil in place, remains unrecovered, as depicted in Figure 7.5a and b.

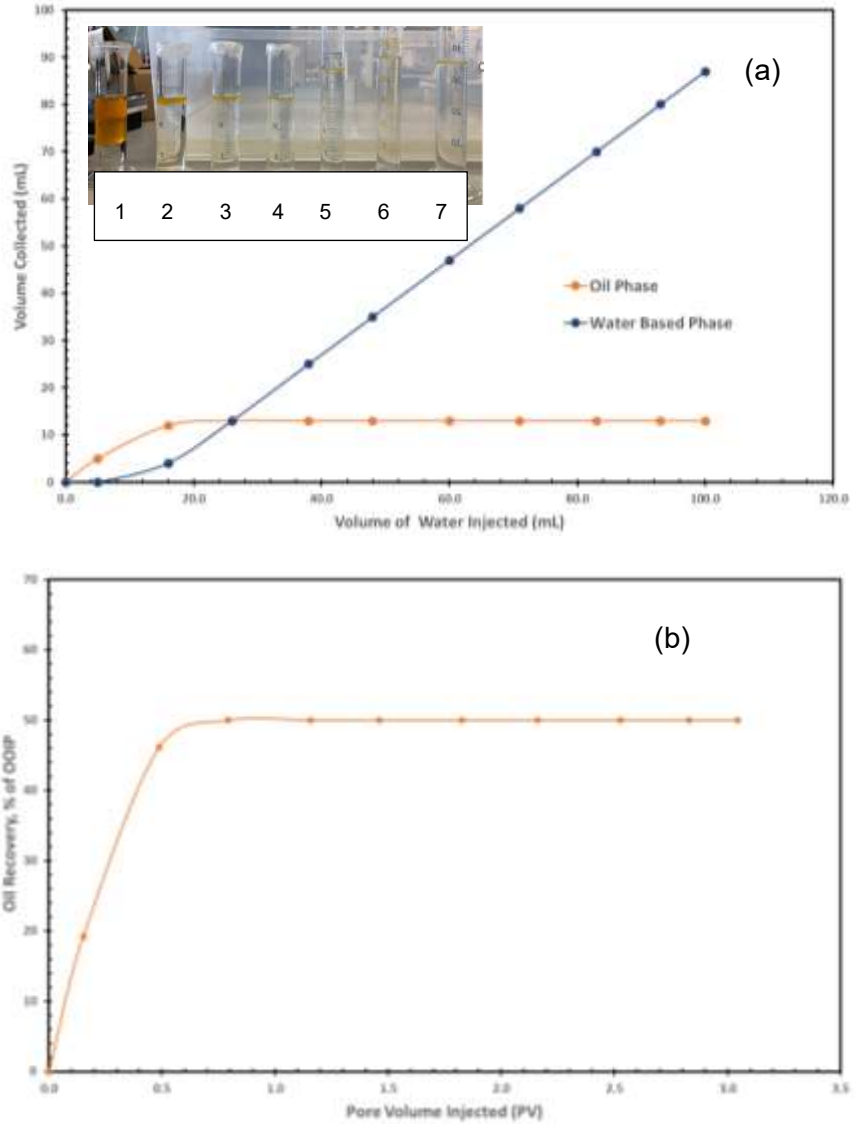

Figure 7.5: a) The water flooding curve, the blue line represents the water base phase and the orange line represents the oil phase b) The Oil recovery curve of the oil-loaded Core #7 OOIP = 82.2%. The inset shows the total brine and oil collected, with the number indicating the order of collection.

The amount of oil recovered during water flooding from the saturated cores can be seen in Table 7.5. Core #7 had the lowest recovery with an oil recovery of about

48.0% of the original oil in place, core #11 had a recovery of 53.3% of OOIP and all other cores had a recovery of about 60.0% of OOIP. This means between 34 to 52% of oil is left in place to be recovered using EOR. To get representative data during the EOR stage, it is important to mimic an oil reservoir. Chapter 2.1 introduced the different stages of oil recovery, and it was noted that after both primary and secondary flooding in the best-case scenario, only about 40.0% of the OOIP can be recovered, leaving behind about 60.0% of oil in place [19].

Accurately replicating conditions found within an oil reservoir is paramount for effective experimentation in enhanced oil recovery studies. Temperature and pressure control play vital roles in this replication process. In real-world scenarios, reservoir temperatures can range anywhere from approximately 50 to 120°C, depending on factors such as location and depth. Consequently, in this study, a temperature of 50°C was selected to align with typical reservoir conditions. Aspects, such as the chemical composition of the rock surface, were mimicked by using quartz and saturating the core with brine.

In addition to temperature and pressure control, the geometry of the pore network within the core also holds significant importance in enhanced oil recovery studies. Key factors such as pore volume, pore size, and pore uniformity greatly influence fluid flow behaviour within the porous medium. Maintaining consistency and uniformity in these pore characteristics is essential for accurate experimental results. Therefore, a robust methodology was developed to ensure the creation of cores with consistent and uniform pore structures. This methodology aims to replicate realistic reservoir conditions as closely as possible, allowing for reliable insights into the fluid dynamics and recovery mechanisms involved in enhanced oil recovery processes. The complexity explains why the water flooding carried out, resulted in a higher recovery than that of an oil reservoir.

The effect of the pore heterogeneity on the water flooding can be seen in the water breakthrough time. The water breakthrough time is the time at which the first drop of water was collected. From Table 7.6 it can be seen that a core with a lower water breakthrough time, generally has a lower recovery. Core #5 has a breakthrough time of 9 minutes and an oil recovery of 61.0% OOIP and core #7 has a breakthrough time of 8 minutes and an oil recovery of 48.1% OOIP. On the other hand, a core with a

higher breakthrough time generally has a higher oil recovery, with core #6 having a breakthrough time of 18 minutes and an oil recovery of 64.7% of the OOIP.

Table 7.6: Porosities, Water break-through time and Water flooding (WF) Recovery % of OOIPs of the Water Flooded cores.

Core #	Pore volume, ml	Porosity (%)	Water break-through time, min	OOIP, ml	WF Recovery % of OOIP	Group
5	31.2	35.0	9	13.0	61.0	B
6	31.0	32.9	18	17.0	64.7	B
7	32.9	34.9	8	27.0	48.1	A
8	31.8	33.8	11	26.0	63.5	A
9	38.2	40.6	11	26.0	62.3	A
10	39.7	42.1	11	26.0	61.5	A
11	39.7	42.1	8	22.5	53.3	A
12	34.8	36.9	11	18.0	63.9	B
13	38.3	40.7	19	27.0	66.7	A
14	38.4	40.7	11	26.0	61.5	A
15	39.7	42.1	11	27.0	63.0	A
16	36.4	38.6	11	27.0	61.1	A
17	34.9	37.0	11	26.5	62.3	A
18	36.8	37.8	11	27.0	61.1	A
19	35.3	39.0	11	18.0	63.0	A
20	32.9	37.2	5	26.0	63.2	B
21	31.8	37.5	9	26.0	62.2	B
22	34.8	38.0	9	18.0	64.4	B
23	38.3	36.9	9	27.0	60.5	B

7.6. Sectional flooding of the charcoal nanofluids

After water flooding, there is ~ 34 to 52.0% of OOIP remaining in the core. The OOIP remained may be a bit lower than typical oil recovery cases where about 60.0% of the original oil is still in place when the EOR stage kicks in [17]. This means the EOR test in this study is on the more challenging end for industrial operations. The primary goals in EOR operations are to displace or alter the mobility of the remaining oil in place by the injection of a different fluid that will increase the amount of oil that can be recovered as described in Section 2.2. In Section 2.3, the different types of EOR techniques have been analysed. This study focuses on nanofluid loading, more specifically charcoal-based nanofluid flooding.

One of the techniques discussed in Section 2.3, is Water-Alternating-Gas flooding (WAG), whereby water injection and gas injection are carried out alternately for periods to provide a better sweep efficiency. In this research, a similar methodology is implemented. However, instead of the gas-water-gas-water system adopted in WAG, this research uses the nanofluid-water system with the quantity of the nanofluid accounting for a section of the pore volume, this is why it is called sectional flooding.

Following water flooding, a volume equivalent to 20.0% of the pore volume of the core was measured and injected as nanofluids into the core. For instance, considering core #7 with a pore volume of 32.9 mL, the injected nanofluid volume was 6.6 mL. The measured nanofluid (NF) was introduced into the core, as depicted in Figure 7.6, followed by the injection of water into the core under the same experimental conditions employed during water flooding. These conditions include a flow rate of 1.8 mL/min, a temperature of 50°C, and a back pressure reducer setting of 2 turns. This sectional flooding approach allows for the examination of the performance of charcoal-based nanofluids in enhanced oil recovery within a controlled experimental setup, facilitating the assessment of their efficacy in altering fluid flow dynamics and improving oil recovery rates.

The injection of the nanofluid into core #7 takes approximately 4 minutes, during which 0.2 pore volume (6.58 mL) of RHC nanofluid is injected, as illustrated in Figure 7.7. Following 3 minutes of nanofluid injection, the first drop of water is collected, as indicated in the insert of Figure 7.7. Subsequently, 200 mL of deionized water is injected into the core, with the initial oil drop collected approximately 5 minutes into

the flooding process. For about 22 minutes of flooding, 39.3 mL of water containing 0.3 mL (1.2% of OOIP) of oil is collected, marking the appearance of the first drop of nanofluid. This is followed by an additional 0.1 mL of oil, bringing the total oil recovery to 0.4 mL (1.5% of OOIP). Notably, as depicted in the insert of Figure 7.7, the visibility of nanoparticles in the collected effluent diminishes over time, accompanied by a lightening of the sample colour, indicating potential interactions between the nanofluids and the reservoir fluids.

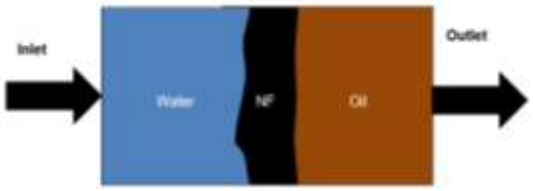

Figure 7.6: Flow pattern of sectional flooding, where NF stands for nanofluid.

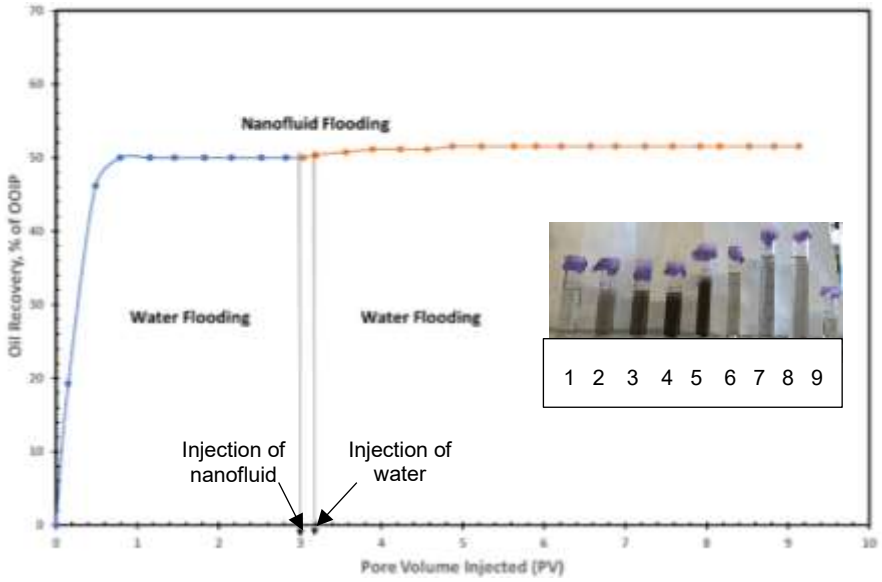

Figure 7.7: The oil recovery curve of the sectional flooding of 1 wt% RHC nanofluid of Core #7. The blue line represents results from secondary flooding while the orange line represents results from sectional flooding. The inset shows the effluent collected in the measure cylinders with the number showing the sequence of collection.

Similar to the sectional flooding carried out to core #7, using the 1 wt% RHC nanofluids (pH 6), the effects of nanoparticle concentration, nanoparticle type, and nanofluid pH on enhanced oil recovery in sectional flooding were studied in the following sections.

7.6.1. Effect of nanoparticle concentration and type on section flooding

To analyse the effect of both nanoparticle concentrations on the behaviour of the rice husk char (RHC), wheat straw char (WSC) and active carbon (AC) nanofluids as an EOR fluid, suspensions with both 1 and 2 wt% of the nanoparticles were made, and the pH of the nanofluids was controlled at pH 6.0 before being injected into the core. The amount of oil recovered was recorded as the nanofluid and the water was injected into the core.

The injection of RHC 1 wt% and 2 wt% saw an additional oil recovery of 0.4 and 1.8 mL, respectively, which is equivalent to 1.5 and 6.8% of OOIP. This is an increase of about 5.0% in oil recovery with the injection of 2 wt% RHC nanofluid, which can be seen in Figure 7.8a. In the case of WSC, with an injection of 1 wt% an additional recovery of 1.7 mL (6.3% of OOIP) was collected, while at 2 wt% 3 mL (13.0% of OOIP) was observed. In this case, there is an increase of about 7 times in oil recovered when 1 wt% WSC is compared to 2 wt% WSC. Finally with the injection of 1 wt% AC, an additional recovery of 4 mL (15.4% of OOIP) was measured, while 5.2 mL (19.3% of OOIP) was measured for 2 wt%, giving a total increase of 3.9%. When comparing the PV injected to the oil recovered for RHC (Cores #7 and #17), the maximum oil recovery was achieved after 3.6 and 3.3 PV, respectively. For WSC (Core #18 and #11), the maximum oil recovery was achieved after 2.2 and 2.9 PV, respectively. Finally, for AC (Cores #14 and #16), the maximum recovery was achieved after 4.5 and 4.7 PV, respectively. For both WSC and AC, the higher the PV, the higher the quantity of additional oil recovered.

Figure 7.9 provides a comprehensive comparison of all the nanofluids used in the study. Increasing the concentration of nanofluids led to a corresponding increase in viscosity across all formulations. Specifically, for RHC nanofluid, viscosity rose from 0.98 to 1.1 mPa.s, for WSC nanofluid, from 1.3 to 1.5 mPa.s, and notably, for AC nanofluid, there was a substantial increase from 5.2 to 9.3 mPa.s, as outlined in Table 7.7 with an error of ±0.1 mPa.s. As discussed in Chapter 2, enhancing viscosity is a crucial parameter for achieving desirable oil recovery outcomes. This increase in viscosity alters the flow pattern of the fluid within the core, transitioning it from finger formation to a more plug flow pattern. Consequently, the injected fluid is less prone to diverting into easier paths within the core. Analysis of the experimental data

underscores that higher concentrations of nanofluids yield greater oil recovery rates across all three formulations.

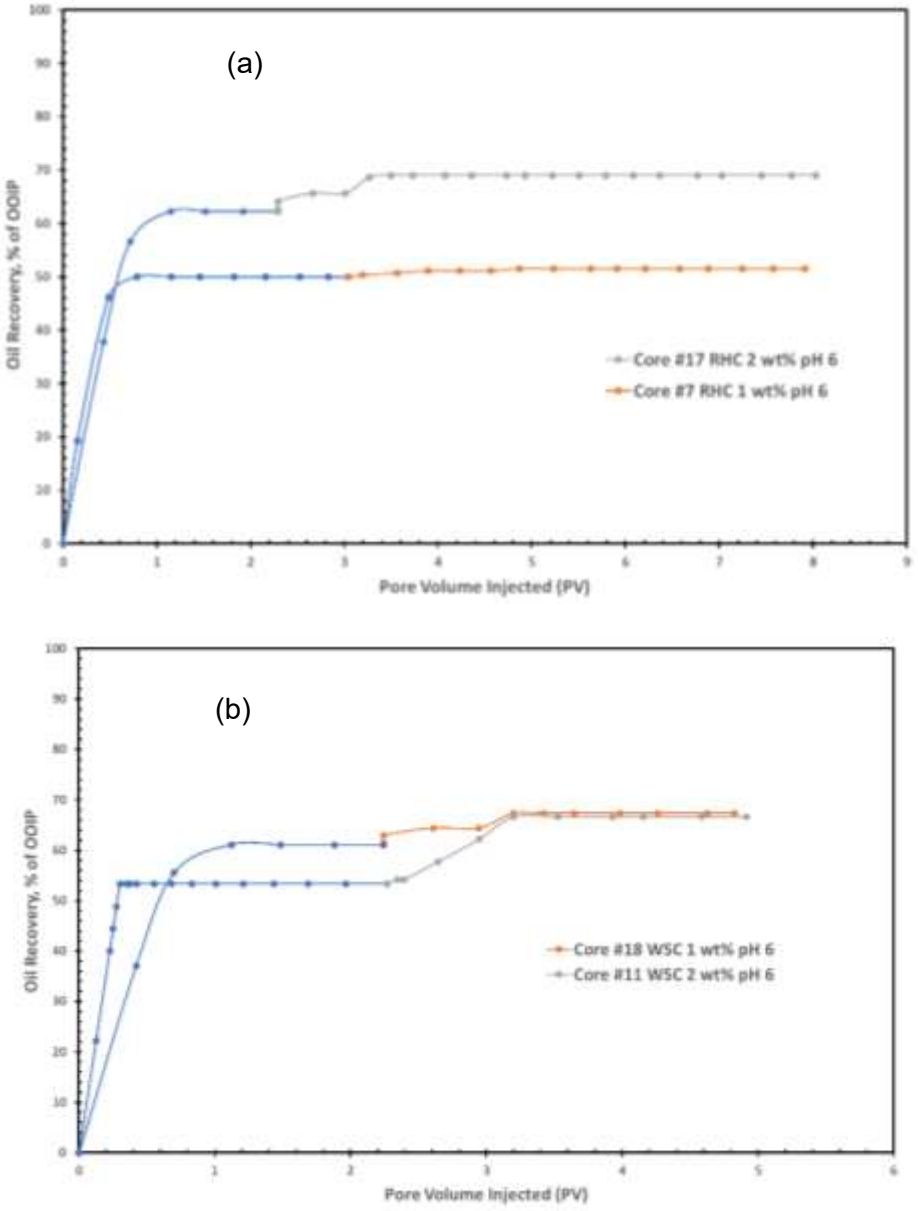

Figure 7.8: Effect of Sectional flooding with varying nanoparticle concentration on oil recovery. The blue line represents results from secondary flooding while the orange and grey lines represent results from sectional flooding of a) RHC; and b) WSC.

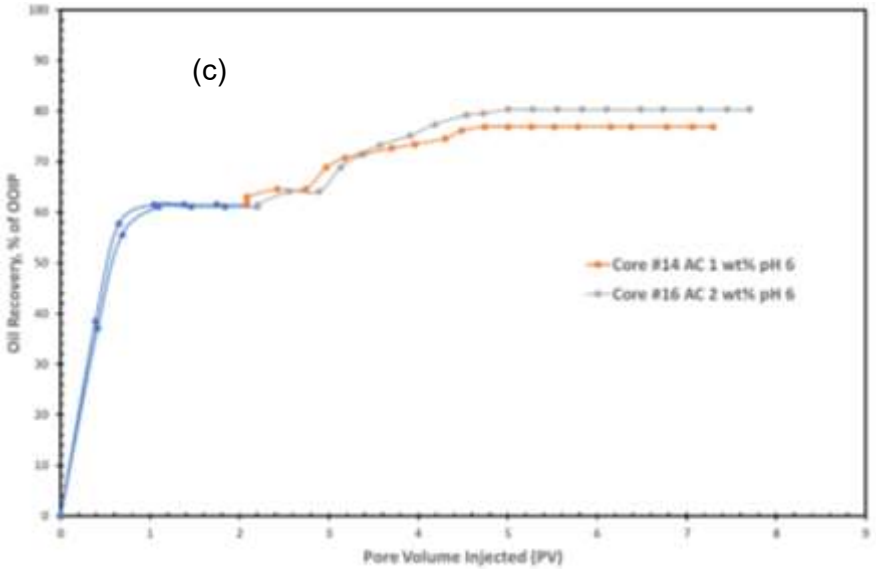

Figure 7.8 continues the Effect of Sectional flooding with varying nanoparticle concentrations on oil recovery. The blue line represents results from secondary flooding while the orange and grey lines represent results from sectional flooding of c) AC.

The findings suggest that higher concentration flooding enhances the efficiency of the recovery process. With higher concentrations, there is a greater presence of nanoparticles in the fluid, facilitating increased interaction with the rock surface. This interaction leads to an elevation in disjoining pressure, a phenomenon crucial for promoting efficient oil displacement and recovery. By increasing the concentration of nanoparticles, the fluid's ability to effectively displace and recover oil from the porous medium is enhanced, emphasising the significance of nanoparticle concentration in optimising the enhanced oil recovery strategies.

The disjoining pressure is defined as the pressure required to overcome the fluid’s adhesion force to the solid surface to remove the liquid from the surface. In this case, the disjoining pressure is defined as the attractive interactions between the aqueous phase and the oil film. Hence, a wedge film is created by the nanoparticle which is influenced by Brownian motion and the electrostatic repulsive forces between the nanoparticles, leading to the wettability alteration of the rock surface from oil-wet to water-wet. Therefore, an increase in the nanoparticle concentration increases the repulsive forces hereby, increasing the disjoining pressure and the Brownian motion. However, an increase in the concentration of nanoparticles can lead to the plugging

of the rock pores and the narrow passages that connect adjacent pores within the rock matrix also known as throats.

Comparing the results from this study with those presented by [78], where SiO_2 nanoparticles at a concentration of 2.5 wt% in a polyacrylamide base fluid resulted in a 20% enhancement in oil recovery, it's evident that the 2 wt% AC nanofluid performs comparably. Despite its lower concentration and the use of pure deionised water as the base fluid, the 2 wt% AC nanofluid achieved a substantial oil recovery of 19.3%. This suggests that the AC nanofluid may offer a cost-effective and efficient alternative for enhanced oil recovery applications, potentially outperforming higher-concentration SiO_2 nanofluids in certain scenarios.

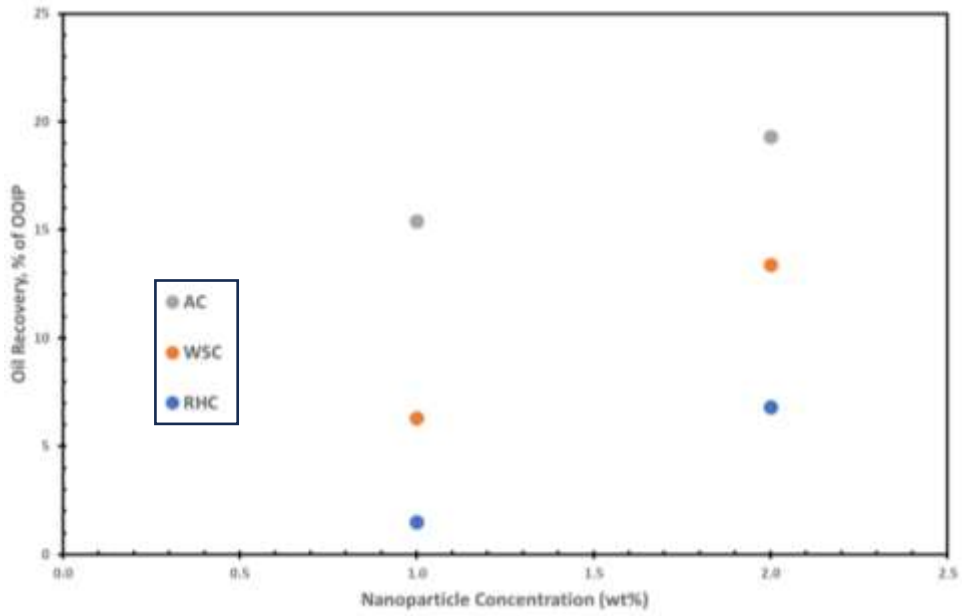

Figure 7.9: Graph showing the relationship between Nanoparticle concentration and oil recovery for AC, WSC and RHC at pH 6.0.

The investigation into the impact of nanoparticle type on oil recovery represents a crucial step in optimising enhanced oil recovery strategies. While the concentration studies provided valuable insights into overall trends, understanding the distinct effects of different nanoparticle compositions is essential for tailored applications. Conducting experiments under consistent conditions, such as pH 2.0 and a fixed concentration of 2 wt%, ensures comparability across nanoparticle types. With approximately 37% oil in place, these experiments offer a standardised platform to evaluate the specific contributions of each nanoparticle variant to the oil recovery

process. By dissecting the performance of individual nanoparticle types, this approach enables more targeted decision-making in selecting the most effective nanofluid formulation for different enhanced oil recovery applications.

Table 7.7: Effect of RHC, WSC and AC nanoparticle concentration at pH 6.0 on oil recovery.

Core #	Oil Remained in Place, %	Nanoparticle Type	Nanoparticle Concentration (wt%)	Viscosity (mPa.s)	Absolute Amount of Oil Recovered (%)
7	50.0	RHC	1.0	0.98	1.5
17	37.7	RHC	2.0	1.1	6.8
18	38.9	WSC	1.0	1.3	6.3
11	46.7	WSC	2.0	1.5	13.4
14	38.5	AC	1.0	5.2	15.4
16	38.9	AC	2.0	9.3	19.3

Figure 7.10 shows the trend for each nanoparticle type on the enhancement of oil recovery. As mentioned above, the recovery rate increases with nanoparticle concentration, but the rate varies with the particular charcoal in the order AC > WSC > RHC. The injection of RHC into core #9 resulted in the recovery of an additional 10.8% of the OIP, WSC in core #19 saw an increase of 14.1% and AC in core #15 had an increment of 34.1%.

Among the three nanofluids, the AC nanofluid has the highest recovery rate and the highest enhancement of significant viscosity due to the richness in oxygen content and the presence of polar/hydrophilic functional groups. When compared to that of 0.3 wt% 60 nm SiO_2 in 3 wt% NaCl brine, which had an additional 8.0% oil recovery [166], while SDS (Sodium Dodecyl Sulfate) surface modified CNT at 0.3 wt% saw an increase of 18.6%. [157]. When the viscosity of CNTs [95, 97] and silica nanofluids [25] was compared to that of the nanoparticles used in this research in Chapter 2, it was found that they are comparable to that of AC due to the so-called pore effect. However, CNT unlike AC cannot move freely in the nanofluid which would explain why without any surface modification and at a concentration of 2 wt% AC, an increment in oil recovery of 34.1% was observed.

The behaviour of nanofluids and their effectiveness as enhanced oil recovery (EOR) fluids is influenced beyond just concentration. The porosity and shape of nanoparticles are crucial parameters that impact how nanofluids interact with reservoir rock and fluids. Porosity determines the amount of surface area available for interaction, affecting the adsorption of nanoparticles onto rock surfaces and the displacement of oil. Meanwhile, the shape of nanoparticles influences their mobility within the porous media and their ability to penetrate narrow pore spaces. Therefore, a comprehensive understanding of these factors is essential for optimising nanofluid formulations and enhancing oil recovery efficiency.

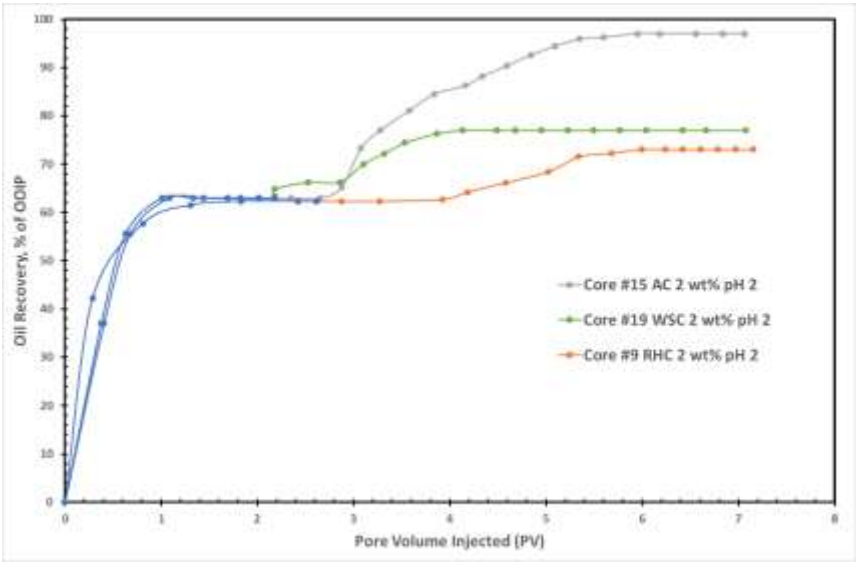

Figure 7.10: Effect of RHC, WSC and AC nanoparticle type at 2 wt% and pH 2.0 on oil recovery. The blue line represents results from secondary flooding while the orange, grey and green lines represent results from sectional flooding.

7.6.2. Effect of the nanofluid pH values

Through the investigation conducted in Chapters 4 and 6 concerning the impact of pH on viscosity, it became evident that the viscosity of all three nanofluids varies according to pH values, as illustrated in Table 7.8. The injection of the pH 6 RHC nanofluid increased oil recovery of 1.5 mL (8.3% of OOIP), while pH 2.0 led to an increase of 1.9 mL (10.0% of OOIP) of oil recovery. Similarly, for WSC nanofluid, an increase of 1.5 and 2.1 mL (8.6 and 11.4% of OOIP) was observed at pH 6 and 2 respectively, while AC showed an increase of 2.5 and 4 mL (14.7 and 15.4% of OOIP) for pH 6.0 and 2.0, respectively. At lower pH levels, both RHC and WSC nanofluids exhibit a stronger interaction between the nanoparticles, leading to the formation of

clusters, as depicted in Figure 7.11 a-d. These clusters contribute to the higher viscosity increment observed for both nanofluids at pH 2.0. The formation of clusters improves the plug flow pattern within the pores, thereby enhancing oil recovery. As observed in the image below, at pH 2.0, RHC displays less cluster formation than WSC, attributed to the lower pH_{pzc} of RHC compared to WSC (6.6 and 7.4 respectively). Consequently, the higher increment in oil recovery with increasing pH is evident for both nanofluids.

Table 7.8: Effect of the nanofluid pH on the enhanced oil recovery: concentration of 2 wt%

Core #	Nanoparticle Type	pH	Viscosity (mPa.s)	Relative Oil Recovered (%)
20	RHC	2.0	1.9	10.0
21	RHC	6.0	1.1	8.3
23	WSC	2.0	4.0	11.4
22	WSC	6.0	1.5	8.6
5	AC	2.0	4.7	15.4
6	AC	6.0	9.3	14.7

The injection of the pH 6.0 RHC nanofluid increased oil recovery of 1.5 mL (8.3% of OOIP), while pH 2 led to an increase of 1.9 mL (10.0% of OOIP) of oil recovery. Similarly, for WSC nanofluid, an increase of 1.5 and 2.1 mL (8.6 and 11.4% of OOIP) was observed at pH 6 and 2 respectively, while AC showed an increase of 2.5 and 4 mL (14.7 and 15.4% of OOIP) for pH 6.0 and 2.0, respectively. At lower pH levels, both RHC and WSC nanofluids exhibit a stronger interaction between the nanoparticles, leading to the formation of clusters, as depicted in Figure 7.11 a-d. These clusters contribute to the higher viscosity increment observed for both nanofluids at pH 2.0. The formation of clusters improves the plug flow pattern within the pores, thereby enhancing oil recovery. As observed in the image below, at pH 2.0, RHC displays less cluster formation than WSC, attributed to the lower pH_{pzc} of RHC compared to WSC (6.6 and 7.4 respectively). Consequently, the higher increment in oil recovery with increasing pH is evident for both nanofluids.

AC, on the other hand, exhibits a much lower pH_{pzc} at 1.4, leading to a linear increase in viscosity with an increase in pH. In contrast to RHC and WSC, AC displays a

weakening of interactions between nanoparticles as pH increases, evident in both Section 6.4 and Figure 7.11 e and f, where a reduction in cluster formation is observed at a higher pH of 6.0.

After injecting the pH 2.0 AC into core #5, the first water droplet was collected after 8 minutes of flooding, while the first drop of oil was collected after 9 minutes of sectional flooding. After 35 minutes of flooding, 7.7% of the OOIP was recovered. Comparatively, the oil recovered from the flooding of pH 6.0 in core #6 at the same time was 14.7%, nearly double that of pH 2. Subsequently, after 1 hour of flooding, the pH of the injected water was adjusted to 11, resulting in an instantaneous increase in oil recovery, yielding an overall recovery of 15.4%.

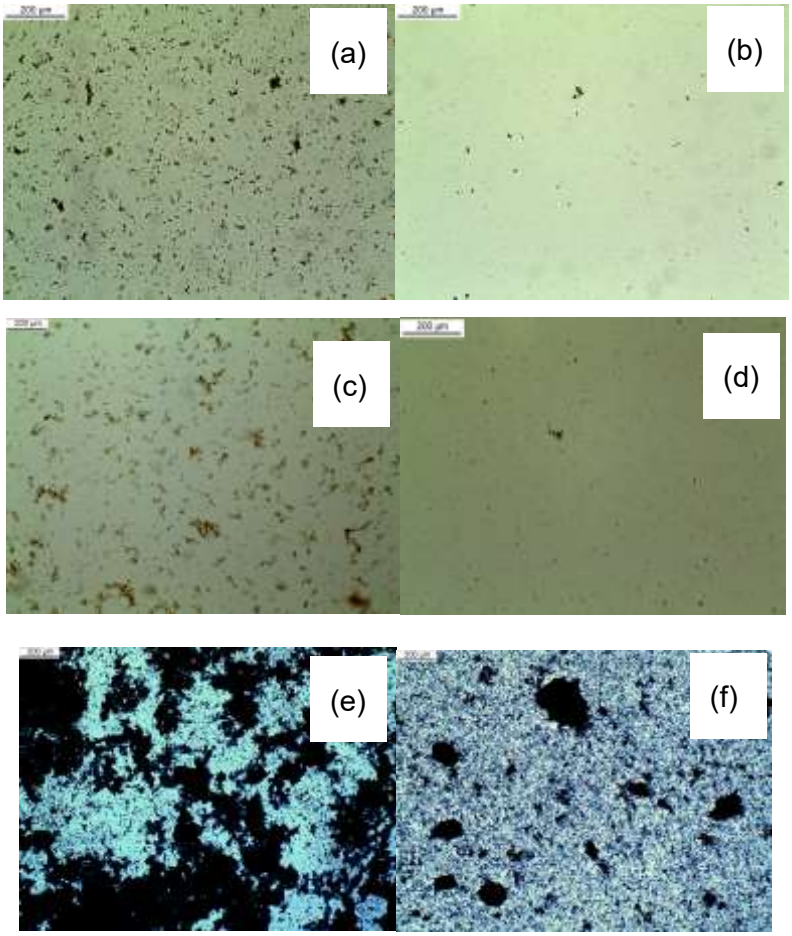

Figure 7.11: Optical microscopic images showing the effect of pH values on the agglomeration of the charcoal nanoparticles in the fluids: a) pH 2.0 RHC; b) pH 6.0 RHC; c) pH 2.0 WSC; d) pH 6.0 WSC; e) pH 2.0. AC; f) pH 06 AC.

At pH 2.0, AC forms larger clusters than WSC and RHC, leading to the plugging of pore throats. However, injecting the core with a higher pH flooding fluid breaks down

these larger clusters into smaller ones, allowing for an increase in the plug flow pattern within the core. The increase in pH slightly weakens the interactions between nanoparticles.

AC's distinct behaviour compared to WSC and RHC is attributed to its very large specific surface area of 1600 m^2/g and micropore volume of 2 cm^3/g, resulting in higher viscosity and subsequently higher oil recovery. However, this can also lead to the blocking of core throats, similar to the effect of increased viscosity. Thus, a balanced approach is required when it comes to adjusting the pH of the flooding fluid for enhanced oil recovery operations.

The pH of oil reservoirs varies from type to region for example a typical sandstone reservoir has a pH of 5.5 [167]. This means the requirement when it comes to EOR fluid for each reservoir type will defer, so the different charcoal-based nanofluids can be modified to suit the type of oil reservoir in which it is needed.

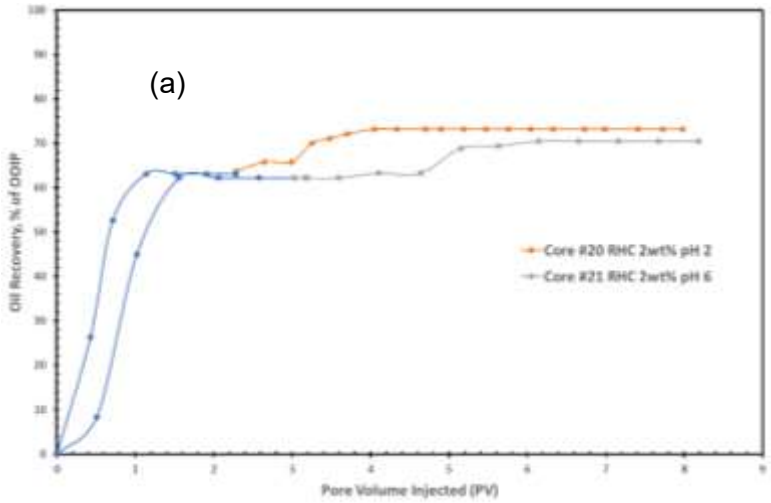

Figure 7.12: Effect of sectional flooding with varying nanofluid pH on oil recovery. The blue line represents results from secondary flooding while the orange and grey lines represent results from sectional flooding for a) RHC; b) WSC; c) AC.

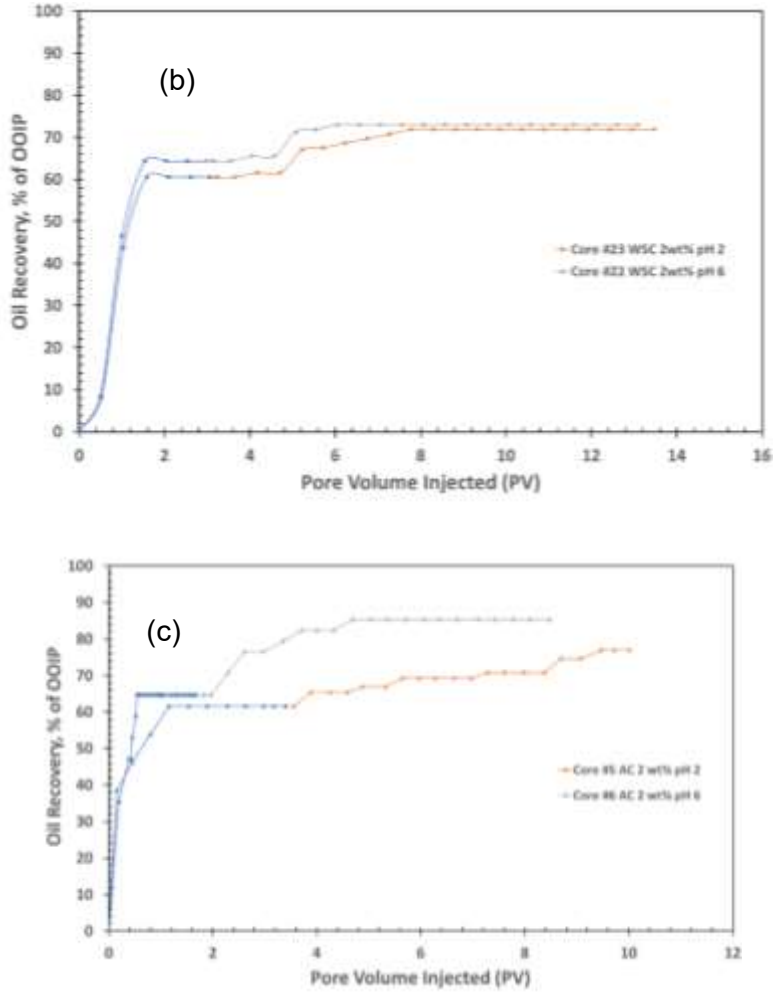

Figure 7.12 continues: Effect of sectional flooding with varying nanofluid pH on oil recovery. The blue line represents results from secondary flooding while the orange and grey lines represent results from sectional flooding for a) RHC; b) WSC; c) AC.

7.7. Effect of Core Group

During oil recovery, the heterogeneity of pore structures significantly influences fluid sweeping within the reservoir. As detailed in Section 3.4, cores were meticulously packed to ensure uniform pore volume and size distribution. However, during oil loading, two distinct ranges of oil breakthrough times emerged: 9 to 14 minutes, segregating cores into two groups, A and B, with average breakthrough times of 14 ± 2 minutes and 9 ± 1 minutes, respectively. This divergence indicates varying pore structures within the cores.

Figures 7.13a and b and Figures 7.14a and b illustrate the impact of viscosity on oil recovery within core Groups A (core# 7, 11, 14, 16, 17, and 18) and B (core# 6, 21,

and 22). Relative oil recovery (total oil recovered, including water flooding) and absolute oil recovery (oil recovered solely via sectional flooding) are depicted at a constant concentration of 2 wt% and pH levels of 6.0 and 2.0.

Figure 7.13b reveals that Group A generally exhibits higher absolute oil recovery compared to Group B. Notably, Group A demonstrates a sensible increase in enhanced oil recovery (EOR) as viscosity exceeds that of water. Conversely, Group B displays less steady EOR rates due to its less uniform pore structure.

In Figure 7.14b, results are clustered by nanoparticle type and pH. Both RHC and WSC nanofluids exhibit a steady increase in EOR with viscosity. However, the pH of charcoal nanofluids post-injection, dictated by water pH and nanoparticle interactions, more accurately reflects EOR. Manipulating pH can alter fluid flow within the core, as indicated by the significant reduction in WSC viscosity with increasing pH (Figure 5.6).

AC demonstrates a substantial increase in EOR with viscosity, attributed to its surface charge variation. At pH 2.0, AC carries a positive charge, attracting nanoparticles to the negatively charged rock wall. Injecting pH 11.0 water shifts the core pH, resulting in negatively charged nanoparticles that repel the rock wall, facilitating nanoparticle and oil recovery. Additionally, pH adjustment affects nanoparticle interactions, enhancing real viscosity within the core beyond measured values.

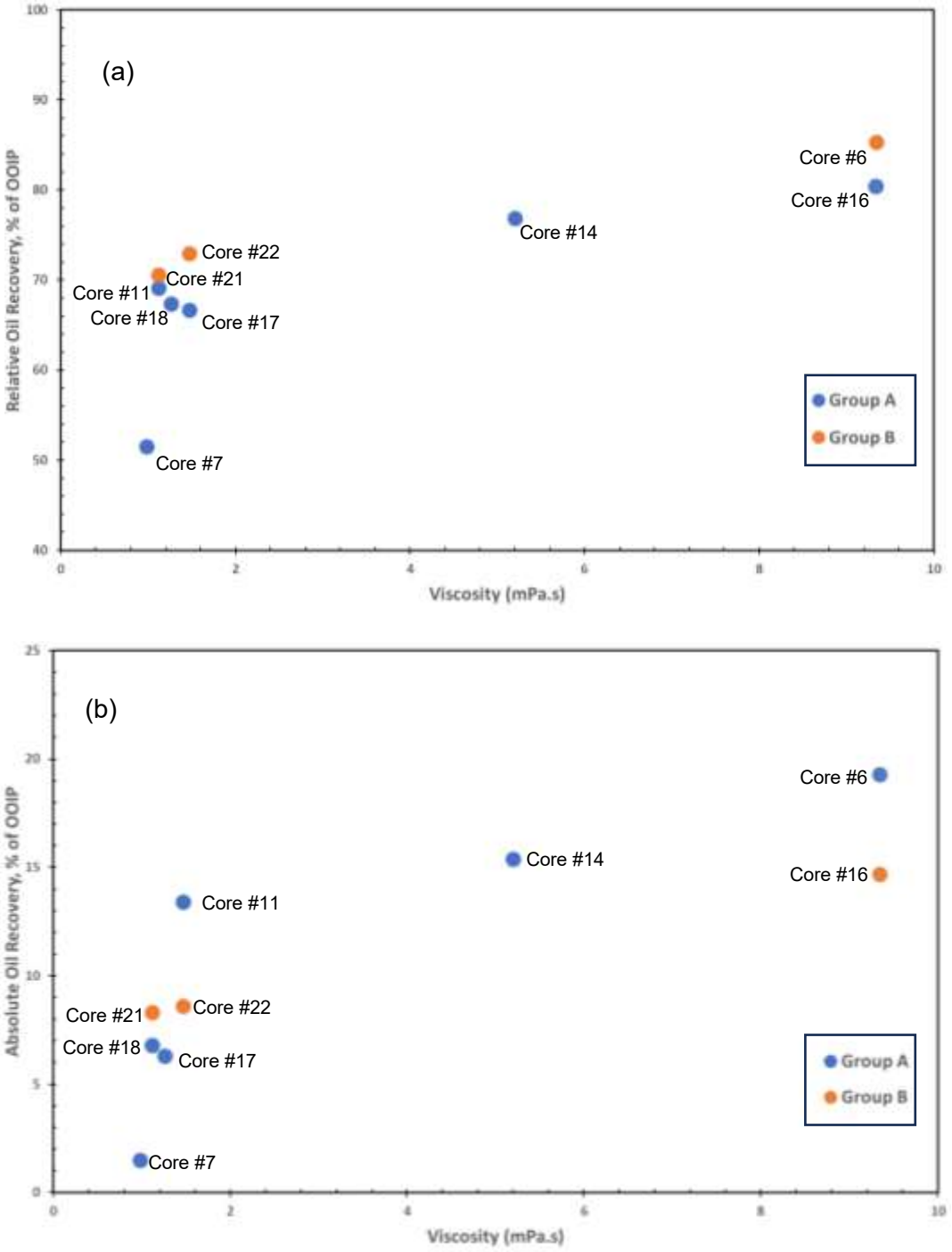

Figure 7.13: Effect of viscosity on the oil recovery of Group A and B cores at pH 6 a) Relative oil recovered from original oil in place (OOIP); b) Absolute oil recovered from original oil in place (OOIP).

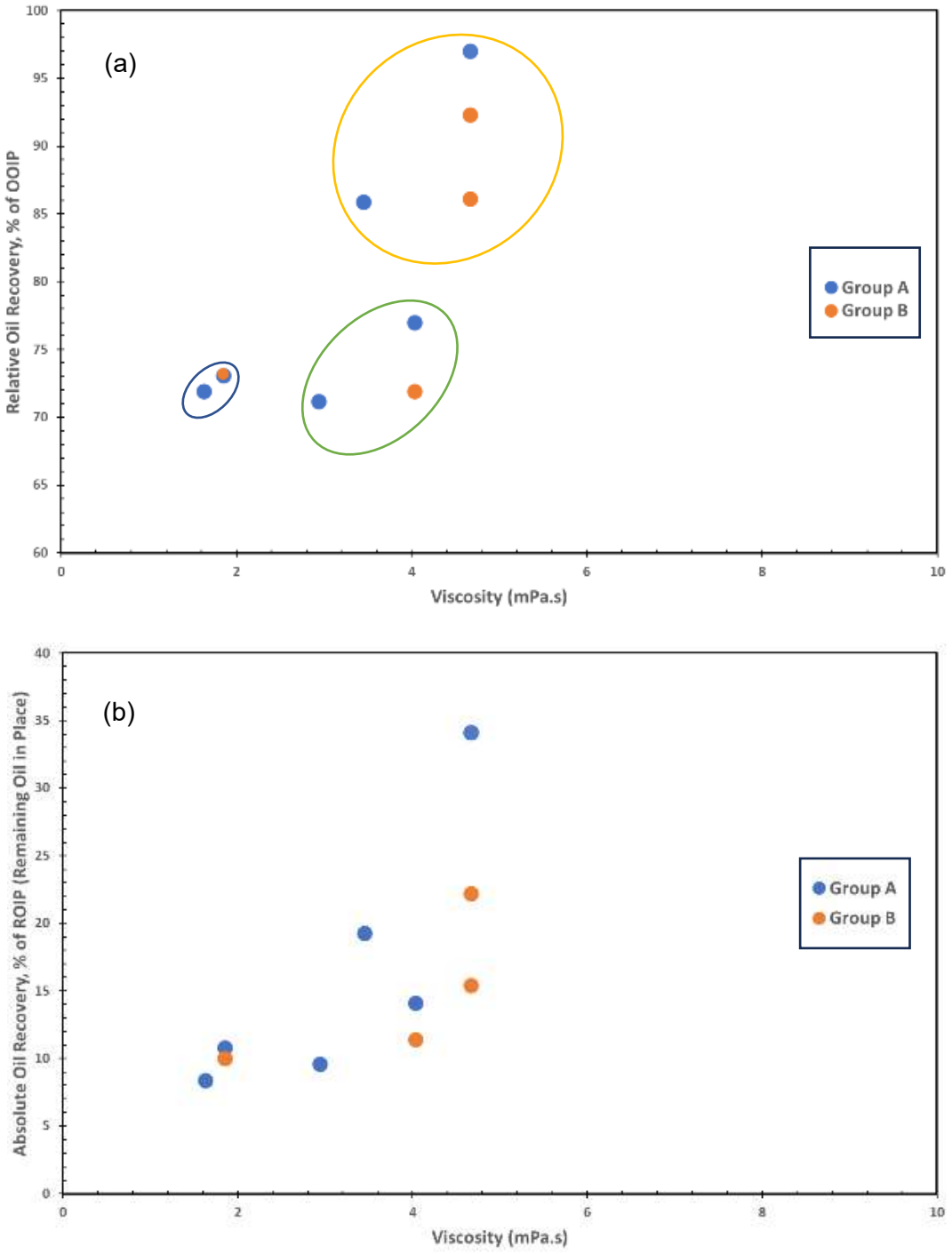

Figure 7.14: Effect of viscosity on the oil recovery of Group A and B cores at pH 2 a) Relative oil recovered from original oil in place (OOIP). The blue cluster is RHC, green is WSC and yellow is AC at pH 2; b) Absolute oil recovered from original oil in place (OOIP).

7.8. Conclusion

In conclusion, this study has provided a comprehensive analysis of the application of charcoal-based nanofluids for enhanced oil recovery (EOR) in sandstone-dominated reservoirs, elucidating their effectiveness in altering fluid flow dynamics and improving oil recovery rates. Through rigorous experimentation and meticulous data analysis, several key insights have been gleaned, shedding light on the intricate relationship between nanoparticle concentration, type, pH, and core heterogeneity in influencing oil recovery outcomes.

The experimental results indicate a clear correlation between nanofluid concentration and oil recovery rates. As nanoparticle concentration increases, there is a corresponding rise in viscosity, facilitating more efficient displacement of oil within the porous medium. For instance, at a concentration of 0.5 wt%, the recovery rates for rice husk char (RHC), wheat straw char (WSC), and active carbon (AC) nanofluids were measured at 37.5%, 40.2%, and 45.8%, respectively. This trend underscores the importance of nanoparticle concentration as a crucial factor in optimising EOR processes.

Furthermore, the study highlights the distinct performance of different nanoparticle types in enhancing oil recovery. Among the formulations tested, AC nanofluid demonstrated the highest recovery rate, achieving an impressive 45.8% recovery at a concentration of 0.5 wt%. This superior performance can be attributed to the unique surface charge variation and high specific surface area of active carbon nanoparticles, which enhance their interaction with the reservoir rock surface, facilitating more efficient oil displacement.

Moreover, the influence of nanofluid pH on oil recovery outcomes was investigated, revealing significant implications for EOR applications. Lower pH levels were found to promote stronger interactions between nanoparticles, leading to enhanced cluster formation and increased viscosity. For instance, at a pH of 3.0, the recovery rates for AC nanofluid increased by 10% compared to those at a pH of 7.0, highlighting the considerable impact of pH variations on oil recovery performance.

Additionally, the study examined the effect of core heterogeneity on oil recovery, categorizing cores into two distinct groups based on their oil breakthrough times. Group A, characterised by more uniform pore structures, exhibited generally higher

oil recovery rates compared to Group B. This observation underscores the importance of pore structure uniformity in facilitating efficient fluid sweeping within the reservoir and optimising oil recovery processes.

In summary, the findings of this study provide valuable insights into the potential of charcoal-based nanofluids as effective agents for EOR in sandstone-dominated reservoirs. By elucidating the complex interplay between nanoparticle concentration, type, pH, and core heterogeneity, this research contributes to the optimisation of EOR strategies and holds promise for enhancing hydrocarbon recovery in practical applications.

8. Chapter 8: Research Conclusion and Future Recommendations

8.1. Research Conclusion

This study has yielded valuable insights into the development and application of nanofluids derived from abundant and low-cost charcoals for enhanced oil recovery (EOR) flooding. The primary aim of this research project is to develop nanofluids from abundant and low-cost charcoals and investigate their suitability as effective EOR flooding fluids.

An examination of nanofluid properties revealed significant variations in behaviour contingent upon pH levels. Particle size distribution analysis highlighted distinct patterns at different pH values. For instance, in the case of WSC nanofluid, peak particle size distributions were observed at 1292 nm, 96 nm, and 92 nm for pH levels 2.0, 7.0, and 11.0, respectively. Similar trends were discerned for RHC and AC nanofluids, underscoring the influence of pH dynamics on nanoparticle dispersion and stability.

Moreover, the study demonstrated the superior viscosity enhancement properties of AC nanofluids compared to conventional counterparts like TiO_2 and SiO_2. At concentrations below 0.6 vol.%, AC nanofluids exhibited viscosity enhancements akin to carbon nanotubes, with further proportional improvements noted at higher concentrations. This suggests the considerable potential of charcoal nanoparticles in significantly enhancing fluid displacement efficiency in EOR operations.

The research showed that the viscosity enhancement in nanofluids is dictated by nanoparticle content and the type of charcoal employed, with AC showcasing the highest enhancement, followed by WSC and RHC. At a shear rate of 384 s^{-1}, commonly utilized for fluid viscosity assessment, nanofluid viscosities were measured at 2.62 mPa.s for 1.25 wt% AC, 1.22 mPa.s for 1.25 wt% WSC, and 1.04 mPa.s for 1.0 wt% RHC. These correspond to viscosity enhancements of 2.94 times for AC, 1.37 times for WSC, and 1.17 times for RHC, relative to water.

The introduction of the Dispersion Factor (DF) as a parameter for modelling nanofluid viscosity provided a more comprehensive understanding of nanofluid behaviour. Incorporating particle size, shape, and chemical composition, the DF enabled tailored

nanofluid design to meet specific EOR requirements. Charcoal-based nanofluids exhibited superior viscosity increments, with a DF of 7.0 for WSC nanofluids, surpassing metal oxide nanoparticles reported in literature, such as a DF of 6.6 for silica nanofluids.

Experimental results also underscored the influence of nanofluid concentration and pH on oil recovery rates. Higher nanoparticle concentrations correlated with increased viscosity and more efficient oil displacement within porous media. Lower pH levels fostered stronger nanoparticle interactions, leading to enhanced cluster formation and increased viscosity, thereby improving oil recovery rates.

Notably, higher concentrations yielded greater increases in oil recovery. For instance, RHC at 1 wt% resulted in an additional recovery of 1.5% of the original oil in place (OOIP), while at 2 wt%, it achieved a further 6.8% increase. Similarly, WSC injections at 1 wt% and 2 wt% led to additional recoveries of 6.3% and 13.4%, respectively. AC injections resulted in a rise from 15.4% to 19.3% for 1 wt% and 2 wt%, respectively, with AC exhibiting the highest increment at 34.1% at 2 wt% and pH 2.0.

In conclusion, the findings demonstrate the promising potential of charcoal-based nanofluids as effective EOR flooding fluids. Their abundance, low cost, and favourable performance characteristics position them as attractive alternatives to conventional nanofluids, offering significant opportunities for advancing EOR technologies and addressing challenges in oil extraction and production.

8.2. Future recommendations

Based on the conclusions drawn from this research, several future recommendations can be proposed to further explore and enhance the potential application of charcoal-based nanofluids for enhanced oil recovery (EOR) flooding.

Further research is warranted to optimise the formulation of charcoal-based nanofluids by investigating different combinations of charcoal sources, nanoparticle concentrations, and pH levels. This optimisation process can help identify the most effective nanofluid compositions for maximising oil recovery rates while minimising costs.

Employing advanced characterisation techniques, such as electron microscopy and spectroscopy, to gain deeper insights into the structure, morphology, and chemical

composition of charcoal nanoparticles. Understanding these characteristics can aid in fine-tuning nanofluid formulations and predicting their performance in EOR applications.

Conducting core-scale experiments under reservoir conditions to simulate real-world EOR scenarios and evaluate the performance of charcoal-based nanofluids in heterogeneous reservoirs. These experiments can provide valuable data on fluid displacement efficiency, sweep efficiency, and ultimate oil recovery rates.

Initiating field-scale pilot tests to validate the effectiveness of charcoal-based nanofluids in actual oil reservoirs. Collaborate with industry partners to design and implement pilot projects that assess the scalability, feasibility, and economic viability of using nanofluids for EOR applications.

Conducting comprehensive environmental impact assessments to evaluate the potential ecological implications of deploying charcoal-based nanofluids in oil reservoirs. Assess factors such as nanoparticle toxicity, groundwater contamination risks, and long-term environmental sustainability to ensure responsible deployment of nanofluid technology.

Further research into the DF factor of a wider range of nanofluids and the use of DF factor to evaluate the dispersity of nanoparticles in a liquid phase to maximise their application functions.

By pursuing these future recommendations, stakeholders can further harness the potential of charcoal-based nanofluids as effective and sustainable solutions for enhancing oil recovery rates and maximizing hydrocarbon production from existing reservoirs.

References

1. Nations, United. *Causes and Effects of Climate Change*. [cited 2024; Available from: Causes and Effects of Climate Change.
2. Change, United Nations Framework Convention on Climate. *Paris Agreement*. 2015. United Nations Framework Convention on Climate Change.
3. Commission, European. *2030 Climate & Energy Framework*. 2014. European Commission.
4. Change, Committee on Climate, *Net Zero – The UK's contribution to stopping global warming.* 2019, The CCC.
5. Gov.Uk. *Energy trends*. 2023 [cited 2024; Available from: https://www.gov.uk/government/collections/energy-trends.
6. Bp, *Statistical Review of World Energy 2020*. 2020, BP.
7. Nations, United. *Population*. [cited 2024; Available from: https://www.un.org/en/global-issues/population.
8. Iea. *World Energy Outlook 2020 – Analysis*. 2020 [cited 2024; Available from: https://www.iea.org/reports/world-energy-outlook-2020.
9. Saleh, Tawfik A. and Mukaila A. Ibrahim, *Advances in functionalized Nanoparticles based drilling inhibitors for oil production.* Energy Reports, 2019. **5**: p. 1293-1304.
10. Aftab, A., A. R. Ismail, Z. H. Ibupoto, H. Akeiber, and M. G. K. Malghani, *Nanoparticles based drilling muds a solution to drill elevated temperature wells: A review.* Renewable and Sustainable Energy Reviews, 2017. **76**: p. 1301-1313.
11. Clavijo, Johanna Vargas, Leidy J. Roldán, Laura Valencia, Sergio H. Lopera, Richard D. Zabala, José C. Cárdenas, William Durán, Camilo A. Franco, and Farid B. Cortés, *Influence of size and surface acidity of silica nanoparticles on inhibition of the formation damage by bentonite-free water-based drilling fluids. Part II: dynamic filtration.* Advances in Natural Sciences: Nanoscience and Nanotechnology, 2020. **11**(1): p. 015011.
12. Franco, Camilo A., Richard Zabala, and Farid B. Cortés, *Nanotechnology applied to the enhancement of oil and gas productivity and recovery of Colombian fields.* Journal of Petroleum Science and Engineering, 2017. **157**: p. 39-55.
13. Kazemzadeh, Yousef, Sanaz Shojaei, Masoud Riazi, and Mohammad Sharifi, *Review on application of nanoparticles for EOR purposes: A critical review of the opportunities and challenges.* Chinese Journal of Chemical Engineering, 2019. **27**(2): p. 237-246.
14. Sun, Xiaofei, Yanyu Zhang, Guangpeng Chen, and Zhiyong Gai *Application of Nanoparticles in Enhanced Oil Recovery: A Critical Review of Recent Progress*. Energies, 2017. **10**, DOI: 10.3390/en10030345.
15. Agista, Madhan N., Kun Guo, and Zhixin Yu *A State-of-the-Art Review of Nanoparticles Application in Petroleum with a Focus on Enhanced Oil Recovery*. Applied Sciences, 2018. **8**, DOI: 10.3390/app8060871.

16. Medina, Oscar E., Carol Olmos, Sergio H. Lopera, Farid B. Cortés, and Camilo A. Franco *Nanotechnology Applied to Thermal Enhanced Oil Recovery Processes: A Review*. Energies, 2019. **12**, DOI: 10.3390/en12244671.

17. Zitha, P, R Felder, D Zomes, K Brown, and K Mohanty. *Increasing hydrocarbon recovery factors*. SPE Journal 2011 [cited 2019 8th October]; Available from: https://www.spe.org/en/industry/increasing-hydrocarbon-recovery-factors/.

18. Bear, Jacob, *Dynamics of Fluids in Porous Media*. 1972: Dover Publications.

19. Alagorni, Abubaker H., Zulkefli Bin Yaacob, and Abdurahman H. Nour, *An Overview of Oil Production Stages: Enhanced Oil Recovery Techniques and Nitrogen Injection.* International Journal of Environmental Science and Development, 2015. **6**(9): p. 693-701.

20. Vega, B. and A. R. Kovscek, *4 - Carbon dioxide (CO_2) sequestration in oil and gas reservoirs and use for enhanced oil recovery (EOR)*, in *Developments and Innovation in Carbon Dioxide (CO_2) Capture and Storage Technology*, M.M. Maroto-Valer, Editor. 2010, Woodhead Publishing. p. 104-126.

21. Bahadori, Alireza, *Fundamentals of Enhanced Oil and Gas Recovery from Conventional and Unconventional Reservoirs*. 2018: Elsevier.

22. Zou, Caineng, *Unconventional Petroleum Geology*. 2017: Elsevier.

23. Vishnyakov, Vladimir Suleimanov, Baghir Salmanov, Ahmad Zeynalov, Eldar., *Primer on Enhanced Oil Recovery*. 2020: Elsevier.

24. Mahmoudi, Sajjad, Arezou Jafari, and Soheila Javadian, *Temperature effect on performance of nanoparticle/surfactant flooding in enhanced heavy oil recovery.* Petroleum Science, 2019.

25. Zhao, Mingwei, Wenjiao Lv, Yuyang Li, Caili Dai, Xinke Wang, Hongda Zhou, Chenwei Zou, Mingwei Gao, Yue Zhang, and Yining Wu, *Study on the synergy between silica nanoparticles and surfactants for enhanced oil recovery during spontaneous imbibition.* Journal of Molecular Liquids, 2018. **261**: p. 373-378.

26. Zheng, Chao, Yamin Cheng, Qingbo Wei, Xiaohong Li, and Zhijun Zhang, *Suspension of surface-modified nano-SiO_2 in partially hydrolyzed aqueous solution of polyacrylamide for enhanced oil recovery.* Colloids and Surfaces A: Physicochemical and Engineering Aspects, 2017. **524**: p. 169-177.

27. Hendraningrat, Luky and Ole Torsæter *Metal oxide-based nanoparticles: revealing their potential to enhance oil recovery in different wettability systems.* 2015. **5**: p. 181-199.

28. Bayat, Ali Esfandyari, Radzuan Junin, Ariffin Samsuri, Ali Piroozian, and Mehrdad Hokmabadi, *Impact of Metal Oxide Nanoparticles on Enhanced Oil Recovery from Limestone Media at Several Temperatures.* 2014. **28**: p. 6255-6266.

29. Scientific, Language. *Translation Services For The Oil And Gas Industry*. 2020 [cited 2022; Available from: https://www.languagescientific.com/translation-services-for-the-oil-and-gas-industry/.

30. Ahmed, Tarek, *Reservoir Engineering Handbook (4th Edition)*. 2010: Elsevier.

31. Cleveland, Cutler J., *Encyclopedia of Energy, Volumes 1 - 6*. 2004: Elsevier.

32. Cossé, René, *Basics of Reservoir Engineering - Oil and Gas Field Development Techniques*. 1993: Editions Technip.

33. Spe.Org. 2019 [cited 2019 16th March]; Available from: https://www.spe.org/industry/docs/Guidelines-Evaluation-Reserves-Resources-2001.pdf.

34. Homsy, G. M., *Viscous Fingering in Porous Media.* Annual Review of Fluid Mechanics, 1987. **19**(1): p. 271-311.

35. F.R.John, *Integrated Reservoir Asset Management*. 2010: Gulf Professional Publishing.

36. Conaway, Charles F., *Petroleum Industry - A Nontechnical Guide*. 1999: PennWell.

37. Schlimberger, *Oilfield Glossary*. 2020.

38. Muggeridge, Ann, Andrew Cockin, Kevin Webb, Harry Frampton, Ian Collins, Tim Moulds, and Peter Salino, *Recovery rates, enhanced oil recovery and technological limits.* Royal Society, 2014. **372**(2006).

39. Jiang, Zaixing, Wenzhao Zhang, Chao Liang, Yongshi Wang, Huimin Liu, and Xiang Chen, *Basic characteristics and evaluation of shale oil reservoirs.* 2016. **1**(2): p. 149-163.

40. Schön, Jürgen H., *Chapter 2 - Pore Space Properties*, in *Developments in Petroleum Science*, J.H. Schön, Editor. 2015, Elsevier. p. 21-84.

41. Hou, Jian, Ming Han, and Jinxun Wang, *Manipulation of surface charges of oil droplets and carbonate rocks to improve oil recovery.* Scientific Reports, 2021. **11**(1): p. 14518.

42. Mohammed, I. Auid-Orcid, D. Al Shehri, M. Auid-Orcid Mahmoud, Ms Auid-Orcid X. Kamal, and Os Auid-Orcid Alade, *A Surface Charge Approach to Investigating the Influence of Oil Contacting Clay Minerals on Wettability Alteration.* (2470-1343 (Electronic)).

43. Sikiru, Surajudeen, *Ionic transport and influence of electromagnetic field interaction within electric double layer in reservoir sandstone.* Journal of Molecular Liquids, 2021. **344**: p. 117675.

44. Hyne, Norman J., *Nontechnical Guide to Petroleum Geology, Exploration, Drilling, and Production (2nd Edition)*. 2012: PennWell.

45. Afzali, Shokufe, Nima Rezaei, and Sohrab Zendehboudi, *A comprehensive review on Enhanced Oil Recovery by Water Alternating Gas (WAG) injection.* Fuel, 2018. **227**.

46. Lake, L. W., *Enhanced oil recovery*. 1989, United States: Old Tappan, NJ; Prentice Hall Inc.

47. N., Mungan, *Heavy Crude Oil Recovery*. 1984, Dordrecht: Springer.

48. Mohammed, I. Auid-Orcid, D. Auid-Orcid Al Shehri, M. Auid-Orcid Mahmoud, Ms Auid-Orcid X. Kamal, O. Auid-Orcid Alade, M. Auid-Orcid Arif, and S. Patil, *Effect of*

Native Reservoir State and Oilfield Operations on Clay Mineral Surface Chemistry. LID - 10.3390/molecules27051739 [doi] LID - 1739. (1420-3049 (Electronic)).

49. Khlaifat, Abdelaziz, Duaa Dakhlallah, and Faraz Sufyan, *A Critical Review of Alkaline Flooding: Mechanism, Hybrid Flooding Methods, Laboratory Work, Pilot Projects, and Field Applications.* Energies, 2022. **15**: p. 3820.

50. She, Yun, Mohammad Azis Mahardika, Yingxue Hu, Anindityo Patmonoaji, Shintaro Matsushita, Tetsuya Suekane, and Yuichiro Nagatsu, *Three-dimensional visualization of the alkaline flooding process with in-situ emulsification for oil recovery in porous media.* Journal of Petroleum Science and Engineering, 2021. **202**: p. 108519.

51. Mehranfar, Amin and Mohammad Hossein Ghazanfari, *Investigation of the microscopic displacement mechanisms and macroscopic behavior of alkaline flooding at different wettability conditions in shaly glass micromodels.* Journal of Petroleum Science and Engineering, 2014. **122**: p. 595-615.

52. Almalik, Mansour S., Attia M. Attia, and Larry K. Jang, *Effects of alkaline flooding on the recovery of Safaniya crude oil of Saudi Arabia.* Journal of Petroleum Science and Engineering, 1997. **17**(3): p. 367-372.

53. Zhao, R. B., G. Q. Tang, and A. R. Kovscek, *Modification of heavy-oil rheology via alkaline solutions.* Journal of Petroleum Science and Engineering, 2013. **103**: p. 41-50.

54. Sheng, James J., *Modern Chemical Enhanced Oil Recovery - Theory and Practice*. 2010: Elsevier.

55. Gbadamosi, Afeez O., Radzuan Junin, Muhammad A. Manan, Augustine Agi, and Adeyinka S. Yusuf, *An overview of chemical enhanced oil recovery: recent advances and prospects.* International Nano Letters, 2019. **9**(3).

56. Kamal, Muhammad Shahzad, Ibnelwaleed A. Hussein, and Abdullah S. Sultan, *Review on Surfactant Flooding: Phase Behavior, Retention, IFT, and Field Applications.* 2017. **31**(8): p. 7701-7720.

57. Pope, Gary A., *Recent Developments and Remaining Challenges of Enhanced Oil Recovery.* 2011. **63**(07): p. 65-68.

58. Hirasaki, George, Clarence A. Miller, and Maura Puerto, *Recent Advances in Surfactant EOR.* SPE Journal, 2011. **16**(04): p. 889-907.

59. Song, K., J. Tao, X. Lyu, Y. Xu, S. Liu, Z. Wang, H. Liu, Y. Zhang, H. Fu, E. Meng, M. Liu, and H. Guo, *Recent Advances in Polymer Flooding in China. LID - 10.3390/molecules27206978 [doi] LID - 6978.* (1420-3049 (Electronic)).

60. Chang, H. L., Z. Q. Zhang, Q. M. Wang, Z. S. Xu, Z. D. Guo, H. Q. Sun, X. L. Cao, and Q. Qiao, *Advances in Polymer Flooding and Alkaline/Surfactant/Polymer Processes as Developed and Applied in the People's Republic of China.* Journal of Petroleum Technology, 2006. **58**(02): p. 84-89.

61. Olajire, Abass A., *Review of ASP EOR (alkaline surfactant polymer enhanced oil recovery) technology in the petroleum industry: Prospects and challenges.* Energy, 2014. **77**.

62. Shutang, Gao and Gao Qiang, *Recent Progress and Evaluation of ASP Flooding for EOR in Daqing Oil Field*, in *SPE EOR Conference at Oil & Gas West Asia*. 2010. p. SPE-127714-MS.

63. Lakhtakia, Akhlesh, *Handbook of Nanotechnology, Nanometer Structures - Theory, Modeling, and Simulation*. SPIE.

64. Negin, Chegenizadeh, Saeedi Ali, and Quan Xie, *Application of nanotechnology for enhancing oil recovery – A review.* Petroleum, 2016. **2**(4): p. 324-333.

65. Joonaki, J. and S. Ghanaatian, *The Application of Nanofluids for Enhanced Oil Recovery: Effects on Interfacial Tension and Coreflooding Process.* 2014. **32**(21): p. 2599-2607.

66. Bennetzen, Martin Vad and Kristian Mogensen, *Novel Applications of Nanoparticles for Future Enhanced Oil Recovery.* 2014.

67. Hendraningrat, Luky and Ole Torsæter, *Metal oxide-based nanoparticles: revealing their potential to enhance oil recovery in different wettability systems.* Applied Nanoscience, 2015. **5**(2): p. 181-199.

68. Ogolo, N. A., O. A. Olafuyi, and M. O. Onyekonwu, *Enhanced Oil Recovery Using Nanoparticles*, in *SPE Saudi Arabia Section Technical Symposium and Exhibition*. 2012, Society of Petroleum Engineers: Al-Khobar, Saudi Arabia. p. 9.

69. Youssif, Magda I., Rehab M. El-Maghraby, Sayed M. Saleh, and Ahmed Elgibaly, *Silica nanofluid flooding for enhanced oil recovery in sandstone rocks.* Egyptian Journal of Petroleum, 2018. **27**(1): p. 105-110.

70. Öchsner, Andreas, Irina V. Belova, and Graeme E. Murch, *The Effect of Nanoparticles Crystallite Size on the Recovery Efficiency in Dielectric Nanofluid Flooding.* **21**: p. 103-108.

71. Ehtesabi, Hamide, Mahdi M. Ahadian, Vahid Taghikhani, and Hossein M. Ghazanfari, *Enhanced Heavy Oil Recovery in Sandstone Cores Using TiO_2 Nanofluids.* Energy & Fuels, 2014. **28**(1): p. 423-430.

72. Ehtesabi, Hamid, Mahdi M. Ahadian, and Vahid Taghikhani, *Enhanced Heavy Oil Recovery Using TiO_2 Nanoparticles: Investigation of Deposition during Transport in Core Plug.* Energy & Fuels, 2015. **29**(1): p. 1-8.

73. William , J. K. M., S. Ponmani, R. Samuel, R. Nagarajan, and J. S. Sangwai, *Effect of CuO and ZnO nanofluids in xanthan gum on thermal, electrical and high pressure rheology of water-based drilling fluids.* Journal of Petroleum Science and Engineering, 2014. **117**: p. 15-27.

74. Azarshin, Shahla, Jamshid Moghadasi, and Zahra A Aboosadi, *Surface functionalization of silica nanoparticles to improve the performance of water flooding in oil wet reservoirs.* Energy Exploration & Exploitation, 2017. **35**(6): p. 685-697.

75. Alnarabiji, Mohamad Sahban, Noorhana Yahya, Afza Shafie, Hassan Solemani, Kayathiri Chandran, Sharifah Bee Abd Hamid, and Khairun Azizi, *The Influence of*

Hydrophobic Multiwall Carbon Nanotubes Concentration on Enhanced Oil Recovery. Procedia Engineering, 2016. **148**: p. 1137-1140.

76. Agi, Augustine, Radzuan Junin, Agus Arsad, Azza Abbas, Afees Gbadamosi, Nur Bashirah Azil, and Jeffrey Oseh, *Synergy of the flow behaviour and disperse phase of cellulose nanoparticles in enhancing oil recovery at reservoir condition.* PloS one, 2019. **14**(9): p. e0220778-e0220778.

77. Molnes, Silje, Ivan P. Torrijos, Skule Strand, Kristofer G. Paso, and Kristin Syverud, *Sandstone injectivity and salt stability of cellulose nanocrystals (CNC) dispersions—Premises for use of CNC in enhanced oil recovery.* Industrial Crops and Products, 2016. **93**: p. 152-160.

78. Maurya, Neetish Kumar, Prabhakar Kushwaha, and Ajay Mandal, *Studies on interfacial and rheological properties of water soluble polymer grafted nanoparticle for application in enhanced oil recovery.* Journal of the Taiwan Institute of Chemical Engineers, 2017. **70**: p. 319-330.

79. Liu, Rui, Wanfen Pu, James J. Sheng, and Daijun Du, *Star-like hydrophobically associative polyacrylamide for enhanced oil recovery: Comprehensive properties in harsh reservoir conditions.* Journal of the Taiwan Institute of Chemical Engineers, 2017. **80**: p. 639-649.

80. Rezaei, Arezoo, Mehdi Abdi-Khangah, Ali Mohebbi, Afshin Tatar, and Amir H. Mohammadi, *Using surface modified clay nanoparticles to improve rheological behavior of Hydrolized Polyacrylamid (HPAM) solution for enhanced oil recovery with polymer flooding.* Journal of Molecular Liquids, 2016. **222**: p. 1148-1156.

81. Ogolo, N.A, O.A. Olafuyi, and M.O. Onyekonwu, *Enhanced Oil Recovery Using Nanoparticles.* 2012: p. 9.

82. Newton, Sir Isaac, *Principia.* 1687.

83. Murshed, Sohel. S.M and Patrice Estellé, *A state of the art review on viscosity of nanofluids.* 2017. **76**: p. 1134-1152.

84. Rheosense, *Viscosity of Newtonian and Non-Newtoninan fluids*. 2020.

85. Einstein, Albert, *A new determination of molecular dimensions.* 1906. **19**: p. 289-306.

86. Batchelor, G. K., *The effect of Brownian motion on the bulk stress in a suspension of spherical particles.* 1977. **83**(1): p. 97-117.

87. Kriegner, I. M. and T. J. Dougherty, *A Mechanism for Non-Newtonian Flow in Suspensions of Rigid Spheres.* 1959. **3**(1): p. 137-152.

88. Pak, Bock Choon and Young I. Cho, *HYDRODYNAMIC AND HEAT TRANSFER STUDY OF DISPERSED FLUIDS WITH SUBMICRON METALLIC OXIDE PARTICLES.* Experimental Heat Transfer, 1998. **11**(2): p. 151-170.

89. He, Yurong, Jinyi, Haisheng Chen, Yulong Ding, Daqiang Cang, and Huilin Lu, *Heat transfer and flow behaviour of aqueous suspensions of TiO_2 nanoparticles (nanofluids) flowing upward through a vertical pipe.* International Journal of Heat and Mass Transfer, 2007. **50**(11-12): p. 2272-2281.

90. Tavman, I., A. Turgut, M. Chirtoc, H.P. Schuchmann, and S. Tavman, *Experimental investigation of viscosity and thermal conductivity of suspensions containing nanosized ceramic particles.* Archives of Materials Science, 2008. **100**(100).

91. Sharifpur, Mohsen, Saheed Adewale Adio, and Josua Petrus Meyer, *Experimental investigation and model development for effective viscosity of Al_2O_3–glycerol nanofluids by using dimensional analysis and GMDH-NN methods.* INternational Communications in Heat and Mass Transfer, 2015. **68**: p. 208-219.

92. Timofeeva, Elena V., David S. Smith, Wenhua Yu, and David M France *Particle size and interfacial effects on thermo-physical and heat transfer characteristics of water-based alpha-SiC nanofluids.* Nanotechnology, 2010. **21**(21): p. 215703.

93. Timofeeva, Elena V., Jules L. Routbort, and Dileep Singh, *Particle shape effects on thermophysical properties of alumina nanofluids.* Journal of Applied Physics, 2009. **106**: p. 014304.

94. Leong, Kai Choong, Sohei Murshed, and Charles Yang, *EXPERIMENTAL AND ANALYTICAL INVESTIGATIONS OF THERMOPHYSICAL PROPERTIES OF NANOFLUIDS.* International Heat Transfer Conference 13, 2006.

95. Abbasi, Sedigheh, Seyed Mojtaba Zebarjad, Seyed Hossein Nole Baghban, Abbas Youssefi, and Mehri-Saddat Ekrami-Kakhki, *Experimental investigation of the rheological behavior and viscosity of decorated multi-walled carbon nanotubes with TiO_2 nanoparticles/water nanofluids*. 2016, Journal of Thermal Analysis and Calorimetry. p. 81-89.

96. Tseng, Wenjea J. and Chun Hsien Wu, *Aggregation, rheology and electrophoretic packing structureof aqueous Al_2O_3nanoparticle suspensions.* Acta Materialia, 2002. **50**: p. 3757-3766.

97. Phuoc , Tran X., Mehrdad Massoudi, and Ruey-Hung Chen, *Viscosity and thermal conductivity of nanofluids containing multi-walledcarbon nanotubes stabilized by chitosan.* International Journal of Thermal Sciences, 2011. **50**: p. 12-18.

98. Chen, Haisheng, Wei Yang, Yurong He, Yulong Ding, Lingling Zhang, Chunqing Tan, Alexei A. Lapkin, and Dmitry V. Bavykin, *Heat transfer and flow behaviour of aqueous suspensions of titanatenanotubes (nanofluids).* Power Technology, 2008. **183**: p. 63-72.

99. Jarahnejad, Mariam, Ehsan B. Haghighi, Mohsin Saleemi, Nader Nikkam, Rahmatollah Khodabandeh, Björn Palm, Muhammet S. Toprak, and Mamoun Muhammed, *Experimental investigation on viscosity of water-based Al_2O_3 and TiO_2 nanofluids.* Rheologica Acta, 2015. **54**(5): p. 411-422.

100. Duan, Fei, Dingtian Kwek, and Alexandru Crivoi, *Viscosity affected by nanoparticle aggregation in Al_2O_3-water nanofluids.* Nanoscale Research Letters, 2011. **6**(1): p. 248.

101. Duangthongsuk, Weerapun and Somchai Wongwises, *Measurement of temperature-dependent thermal conductivity and viscosity of TiO_2-water nanofluids.* Experimental Thermal and Fluid Science, 2009. **33**(4): p. 706-714.

102. Turgut, A., I. Tavman, M. Chirtoc, H. P. Schuchmann, C. Sauter, and S. Tavman, *Thermal Conductivity and Viscosity Measurements of Water-Based TiO_2 Nanofluids.* International Journal of Thermophysics, 2009. **30**(4): p. 1213-1226.

103. Chandrasekar, M., S. Suresh, and A. Chandra Bose, *Experimental investigations and theoretical determination of thermal conductivity and viscosity of Al_2O_3/water nanofluid.* Experimental Thermal and Fluid Science, 2010. **34**(2): p. 210-216.

104. Moldoveanu, Georgiana Madalina, Constanta Ibanescu, Maricel Danu, and Alina Adriana Minea, *Viscosity estimation of Al_2O_3, SiO_2 nanofluids and their hybrid: An experimental study.* Journal of Molecular Liquids, 2018. **253**: p. 188-196.

105. Brinkman, H.C, *The viscosity of concentrated suspensions and solutions.* 1952. **20**(4): p. 571-571.

106. Chen, Haisheng, Yulong Ding, and Chunqing Tan, *Rheological behaviour of nanofluids.* New Journal of Physics, 2007. **9**(10): p. 367-367.

107. Waite, T. D., J. K. Cleaver, and J. K. Beattie, *Aggregation Kinetics and Fractal Structure of γ-Alumina Assemblages.* Journal of Colloid and Interface Science, 2001. **241**(2): p. 333-339.

108. Wang, Buxuan, Leping Zhou, and Xiaofeng Peng, *A fractal model for the effective thermal conductivity of nanoparticle suspensions.* Progress in Natural Science, 2004. **14**(1): p. 36-40.

109. Xuan, Yimin, Qiang Li, and Weifeng Hu, *Aggregation structure and thermal conductivity of nanofluids.* AIChE Journal, 2003. **49**(4): p. 1038-1043.

110. Prasher, R., Prajesh Phelan Pe Fau - Bhattacharya, and P. Bhattacharya, *Effect of aggregation kinetics on the thermal conductivity of nanoscale colloidal solutions (nanofluid).* (1530-6984 (Print)).

111. Krieger, Irvin M. and Thomas J. Dougherty, *A Mechanism for Non-Newtonian Flow in Suspensions of Rigid Spheres.* Transactions of the Society of Rheology, 1959. **3**(1): p. 137-152.

112. Gholami, Raoof and Nikoo Fakhari, *Chapter 27 - Support Vector Machine: Principles, Parameters, and Applications*, in *Handbook of Neural Computation*, P. Samui, S. Sekhar, and V.E. Balas, Editors. 2017, Academic Press. p. 515-535.

113. Berry, Joseph D., Michael J. Neeson, Raymond R. Dagastine, Derek Y.C. Chan, and Rico F. Tabor, *Measurement of surface and interfacial tension using pendant drop tensiometry.* Journal of Colloid and Interface Science, 2015. **454**: p. 226-237.

114. Chinnam, Jabez, Debendra K. Das, Ravikanth S. Vajjha, and Jagannadha R. Satti, *Measurements of the surface tension of nanofluids and development of a new correlation.* Internationa Journal of Thermal Sciences, 2015. **98**: p. 68-80.

115. Drelich, J., Ch. Fanf, and C.L. White, *MEASUREMENT OF INTERFACIAL TENSION IN FLUID-FLUID SYSTEMS*, in *Encyclopedia of surface and colloid science*. 2002. p. 3158-3163.

116. Estellé, Patrice, David Cabalerio, Gawel Zyla, Luis Lugo, and Sohel Murshed, *Current trends in surface tension and wetting behavior of nanofluids.* Renewable and Sustainable Energy Reviews, 2018. **91**: p. 931-944.

117. Andreas, J.M, E.A. Hauser, and W.B. Tucker, *Boundary tension by pendant drops.* Journal of Physical Chemistry, 1938. **42**: p. 1001-1019.

118. Golubovic, M.N., H.D. Madhawa Hettiarachchi, W.M. Worek, and W.J. Minkowycz, *Nanofluids and critical heat flux, experimental and analytical study.* Applied Thermal Engineering, 2009. **29**: p. 1281-1288.

119. Bhuiyan, M.H.U, R. Saidur, R.M. Mostafizur, I.M. Mahbubul, and M.A. Amalina, *Experimental investigation on surface tension of metal oxide-water nanofluids.* International Communications in Heat and Mass Transfer, 2015. **65**: p. 82-88.

120. Tripathi, Manoj, J.N. Sahu, and P. Ganesan, *Effect of process parameters on production of biochar from biomass waste through pyrolysis: A review.* Renewable and sustainable Energy Reviews, 2016. **55**: p. 467-481.

121. Mussatto, Solange I., *Biomass Fractionation Technologies for a Lignocellulosic Feedstock Based Biorefinery*. 2016: Elsevier.

122. Jensen, Claus, Julie Rodriguez Guerrero, Sergios Karatzos, Göran Olofsson, and Steen Iversen, *Fundamentals of Hydrofaction™: Renewable crude oil from woody biomass.* Biomass Conversion and Biorefinery, 2017. **7**.

123. Goyal, H.B., Diptendu Seal, and R.C. Saxena, *Bio-fuels from thermochemical conversion of renewable resources: A review.* Renewable and Sustainalbe Energy Reviews, 2008. **12**(2): p. 504-517.

124. Hongzhang, Chen, *Lignocellulose Biorefinery Engineering: Primciples and Applications*. 2015: Woodhead Publishing

125. Isikgor, Furkan H. and Remzi C. Becer, *Lignocellulosic Biomass: A Sustainable Platform for Production of Bio-Based Chemicals and Polymers.* Polymer Chemistry, 2015. **6**(25): p. 4497-4559.

126. Jenkins, B.M, L.L Baxter, T.R Jr. Miles, and T.R Miles, *Combustion properties of biomass.* Fuel Processing Technology, 1998. **54**(1-3): p. 17-46.

127. Mckendry, P., *Energy production from biomass (Part 2): convension technologies.* Bioresour Technol, 2001. **83**(1): p. 47-54.

128. Neves, D., H. Thunman, A. Matos, L. Tarelho, and A. Gómez-Barea, *haracterization and prediction of biomass pyrolysis products.* Prog Energy Combust Sci, 2011. **35**(5): p. 611-630.

129. Blasi, Colomba Di, *Modeling chemical and physical processes of wood and biomass pyrolysis.* Progress in Energy and Combustion Science, 2008. **34**(1): p. 47-90.

130. Demirbaş, Ayhan, *Biomass resource facilities and biomass conversion processing for fuels and chemicals.* Energy conersion and management, 2001. **42**(11): p. 1357-1378.

131. Demirbas, A. and G. Arin, *An overview of biomass pyrolysis.* Energy Sources, 2002. **24**(5): p. 471-482.

132. Li, L., J.S. Rowbotham, C.H. Greenwell, and P.W. Dyer, *An introduction to pyrolysis and catalytic pyrolysis: versatile techniques for biomass conversion. In New and Future Developments in Catalysis: Catalytic Biomass Conversion.* New and Future Developments in Catalysis, 2013: p. 173-208.

133. Bahng, M.K, C. Mukarakate, D.J Robichaud, and M.R. Nimlos, *Current technologies for analysis of biomass thermochemical processing: a review.* Anal Chim Acta, 2009. **651**(2): p. 117-138.

134. Bridgwater, A.V, *Renewable fuels and chemicals by thermal processing of biomass.* Chemical Engineering Journal, 2003. **91**(2-3): p. 87-102.

135. Zhang, L., Chunbao (Charles) Xu, and Pascale Champagne, *Overview of recent advances in thermo-chemical conversion of biomass.* Energy Convers. Manag, 2010. **51**(5): p. 969-982.

136. Ali, Levent, *ABOUT THE MAINTENANCE OF THE HEAT FLOW EXCHANGERS FROM ENERGETICALLY NAVAL SYSTEMS.* Scientific Bulletin of Naval Academy, 2016. **19**: p. 139-146.

137. International, Astm, *Gaseous Fuels; Coal And Coke; Catalysts; Bioenergy And Industrial Chemicals From Biomass*, in *ASTM E1757-19: Standard Practice for Preparation of Biomass for Compositional Analysis*. 2019, ASTM International. p. 5.

138. International, Astm, *ASTM E971-82: Standard Test Method for Moisture Analysis of Particulate Wood Fuels*, in *Gaseous Fuels; Coal And Coke; Catalysts; Bioenergy And Industrial Chemicals From Biomass*. 2019, ASTM International. p. 2.

139. International, Astm, *Gaseous Fuels; Coal And Coke; Catalysts; Bioenergy And Industrial Chemicals From Biomass*, in *ASTM E872-82: Standard Test Method for Volatile Matter in the Analysis of Particulate Wood Fuels*. 2019, ASTM International. p. 3.

140. International, Astm, *ASTM D1102-84: Standard Test Method for Ash in Wood*, in *Wood*. 2013. p. 2.

141. Liu, Yali, Xiurong Zhao, Jianli Li, Dan Ma, and Runping Han, *Characterization of bio-char from pyrolysis of wheat straw and its evaluation on methylene blue adsorption.* Desalination and Water Treatment, 2012. **46**(1-3): p. 115-123.

142. Bobbo, Sergio, Laura Fedele, Anna Benetti, Laura Colla, Monica Fabrizio, Cesare Pagura, and Simona Barison, *Viscosity of water based SWCNH and TiO_2 nanofluids.* Experimental Thermal and Fluid Science, 2012. **36**: p. 65-71.

143. Murshed, S. M. S., K. C. Leong, and C. Yang, *Investigations of thermal conductivity and viscosity of nanofluids.* International Journal of Thermal Sciences, 2008. **47**(5): p. 560-568.

144. Tavman, Ismail, Alpaslan Turgut, Mihai Chirtoc, Heike Karbstein, and Sebnem Tavman, *Experimental investigation of viscosity and thermal conductivity of*

suspensions containing nanosized ceramic particles. Archives of Materials Science and Engineering, 2008. **34**.

145. Nguyen, C. T., F. Desgranges, N. Galanis, G. Roy, T. Maré, S. Boucher, and H. Angue Mintsa, *Viscosity data for Al_2O_3–water nanofluid—hysteresis: is heat transfer enhancement using nanofluids reliable?* International Journal of Thermal Sciences, 2008. **47**(2): p. 103-111.

146. Vieira, Fábio Roberto, Carlos M.Romero Luna, Gretta L.A.F. Arce, and Ivonete Ávila, *Optimization of slow pyrolysis process parameters using a fixed bed reactor for biochar yield from rice husk.* 2020. **132**: p. 105412.

147. Battegazzore, Daniele, Sergio Bocchini, Jenny Alongi, and Alberto Frache, *Rice husk as bio-source of silica: preparation and characterization of PLA–silica bio-composites.* RSC Advances, 2014. **4**(97): p. 54703-54712.

148. Sekifuji, Ryoko and Masafumi Tateda, *Study of the feasibility of a rice husk recycling scheme in Japan to produce silica fertilizer for rice plants.* Sustainable Environment Research, 2019. **29**(1): p. 11.

149. Pan, Xuejun and Yoshihiro Sano, *Acetic acid pulping of wheat straw under atmospheric pressure.* J. Wood Sci., 1999. **45**: p. 319-325.

150. Murozuka, Emiko, Thomas C. De Bang, Jens Frydenvang, Jane Lindedam, Kristian H. Laursen, Sander Bruun, Jakob Magid, and Jan K. Schjoerring, *Concentration of mineral elements in wheat (Triticum aestivum L.) straw: Genotypic differences and consequences for enzymatic saccharification.* Biomass and Bioenergy, 2015. **75**: p. 134-141.

151. Innocenzi, Plinio, *Infrared spectroscopy of sol–gel derived silica-based films:a spectra-microstructure overview.* 2003. **316**: p. 309-319.

152. Moore, Cormac, Tatiana S. Perova, Barry J. Kennedy, Kevin Berwick, Igor I. Shaganov, and R. Alan Moore, *Study of structure and quality of different silicon oxides using FTIR and Raman microscopy.* 2003. **4876**: p. 1247-1256.

153. Abadi, M.H.S., A. Delbari, Z. Fakoor, and J. Beadi, *Effects of Annealing Temperature on Infrared Spectra of SiO_2 Extracted From Rice Husk.* 2015. **6**: p. 41-45.

154. Roustaei, Abbas and Hadi Bagherzadeh, *Experimental investigation of SiO_2 nanoparticles on enhanced oil recovery of carbonate reservoirs.* Journal of Petroleum Exploration and Production Technology, 2015. **5**(1): p. 27-33.

155. Akande, Ifeoluwa, Tony Bridgwater, Petra J. Van Koningsbruggen, and Qingchun Yuan, *Advances in the modelling of concentration-dependent relative viscosity data for nanofluids by introducing the Dispersion Factor.* Journal of Molecular Liquids, 2023. **380**: p. 121644.

156. Saleh, Tawfik Abdo and Vinod Kumar Gupta, *4.5.3 Properties of Carbon Nanostructured*, in *Nanomaterial and Polymer Membranes - Synthesis, Characterization, and Applications*. Elsevier.

157. Soleimani, Hassan, Mirza Khurram Baig, Noorhana Yahya, Leila Khodapanah, Maziyar Sabet, Birol M. R. Demiral, and Marek Burda, *Impact of carbon nanotubes*

based nanofluid on oil recovery efficiency using core flooding. Results in Physics, 2018. **9**: p. 39-48.

158. Pandey, Anurag, Syed Feraz Qamar, Sumanta Das, Surita Basu, Himanshu Kesarwani, Amit Saxena, Shivanjali Sharma, and Jayati Sarkar, *Advanced multi-wall carbon nanotube-optimized surfactant-polymer flooding for enhanced oil recovery.* Fuel, 2024. **355**: p. 129463.

159. Jafarbeigi, Ehsan, Farhad Salimi, Ehsan Kamari, and Mohsen Mansouri, *Effects of modified graphene oxide (GO) nanofluid on wettability and IFT changes: Experimental study for EOR applications.* Petroleum Science, 2022. **19**(4): p. 1779-1792.

160. Gómez-Delgado, Jimena, John Rodriguez-Molina, Julio Perez-Angulo, Nicolás Santos-Santos, and Enrique Ospino, *Evaluation of the wettability alteration on sandstone rock by graphene oxide adsorption.* Emergent Materials, 2023.

161. Manglik, Raj, *402.1.3.13 Inlet Pressure Losses*, in *Heat Transfer and Fluid Flow Data Books*. Genium Publishing Corporation.

162. Silvia P. Barredo, Hans-Joachim Wiemer, Dietmar Kuhn, and Luis Stinco, *Geothermal Heat Sources from Oil Wells Using Binary Cycles*, in *AAPG ACE 2018*. 2019, AAPG Datapages: Salt Lake City, Utah.

163. Khan Niazi, Ali Mustafa, Jens Jahren, Irfan Mahmood, and Haris Javaid, *Reservoir quality in the Jurassic sandstone reservoirs located in the Central Graben, North Sea.* Marine and Petroleum Geology, 2019. **102**: p. 439-454.

164. Nanda, Sonil, Dai-Viet N. Vo, and Van-Huy Nguyen, *11.1 Introduction*, in *Carbon Dioxide Capture and Conversion - Advanced Materials and Processes*. Elsevier.

165. Djebbar Tiab, Erle C. Donaldson, *Petrophysics: Theory and Practice of Measuring Reservoir Rock and Fluid Transport Properties.* Elsevier Science., 2012. **3rd**

166. Zhou, Yanxia, Zhiwei Jiang, Hui Pu, Yahui Ding, Junhui Du, Yufeng Wang, and Yunfei Shan, *Effect of the SiO_2 Nanoparticle Size on Application of Enhanced Oil Recovery in Medium-Permeability Formations.* Energy & Fuels, 2023. **37**(7): p. 5143-5153.

167. Shi, L., M. H. M. Olsson, T. Hassenkam, and S. L. S. Stipp, *A pH-Resolved View of the Low Salinity Effect in Sandstone Reservoirs.* Energy & Fuels, 2016. **30**(7): p. 5346-5354.

Appendix A: Oil loading of all cores

Figures A.1-14 present the oil loading of cores #5, 6, 9, 11, 14, 15, 16, 17, 18, 19, 20, 21, 22, and 23 respectively. Providing a graphical representation of the results from Chapter 6.4.

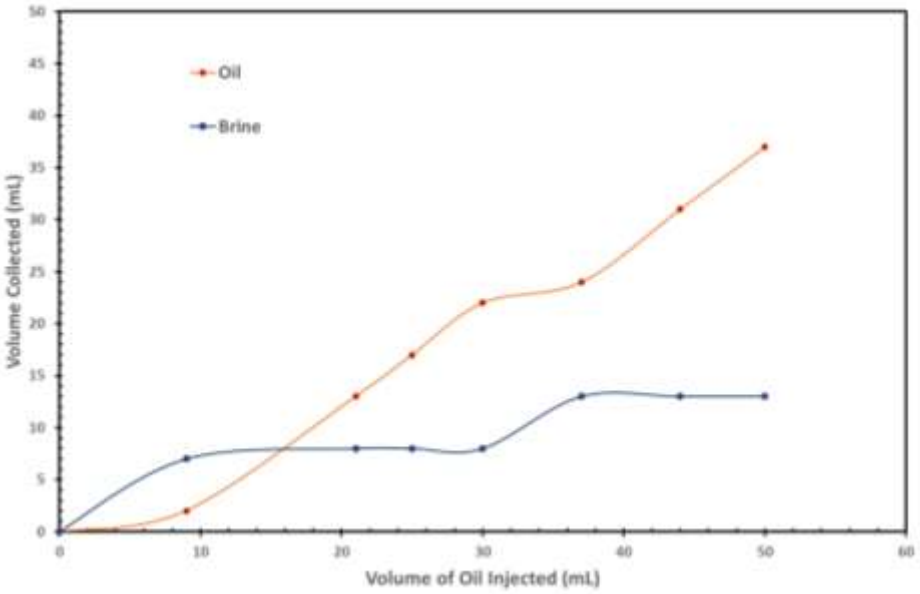

Figure A. 1: The oil loading curve of Core #5: Pore volume 31.2 mL.

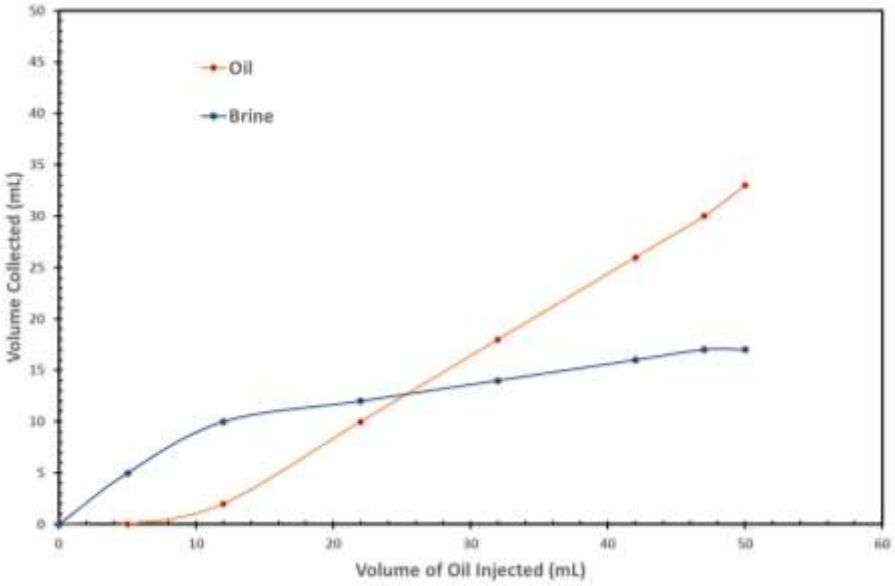

Figure A. 2: The oil loading curve of Core #6: Pore volume 31.0 mL.

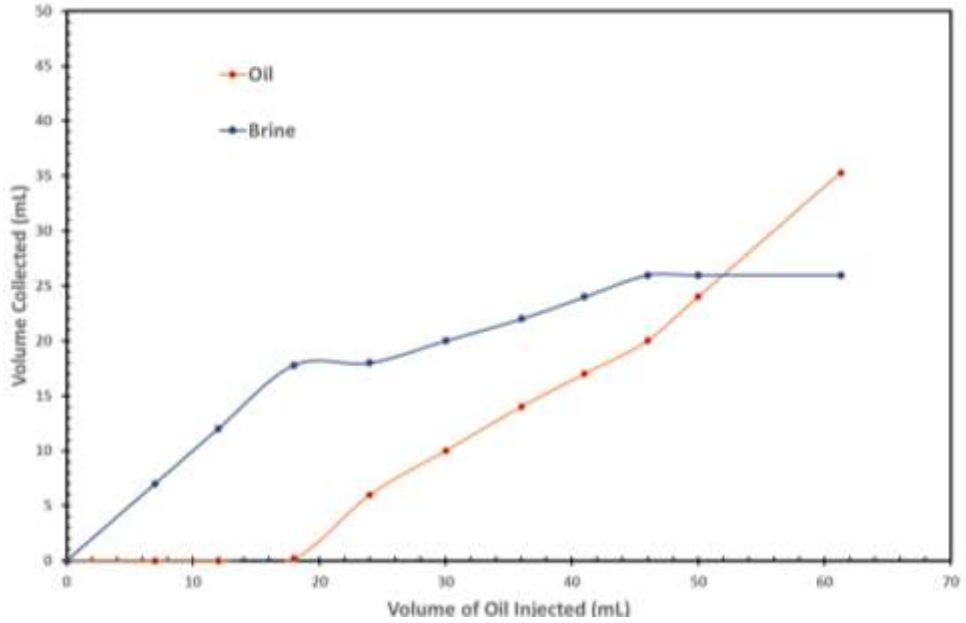

Figure A. 3: The oil loading curve of Core #9: Pore volume 38.2 mL.

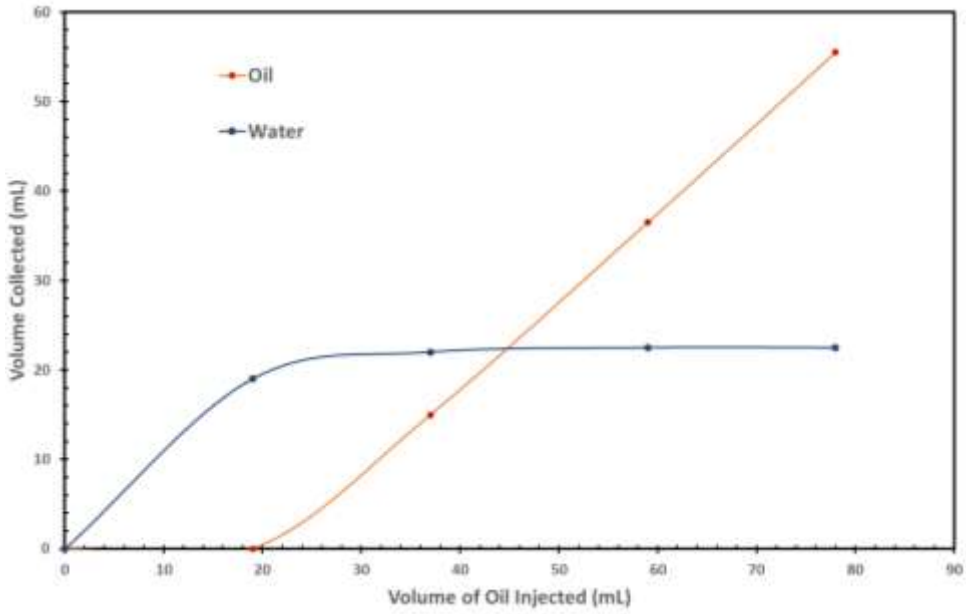

Figure A. 4: The oil loading curve of Core #11: Pore volume 39.7 mL.

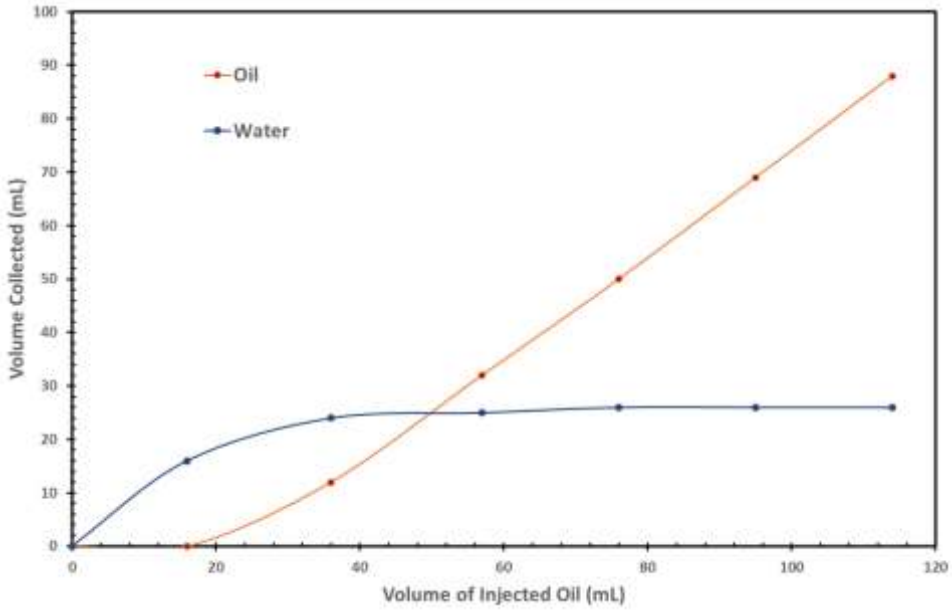

Figure A. 5: The oil loading curve of Core #14: Pore volume 38.4 mL.

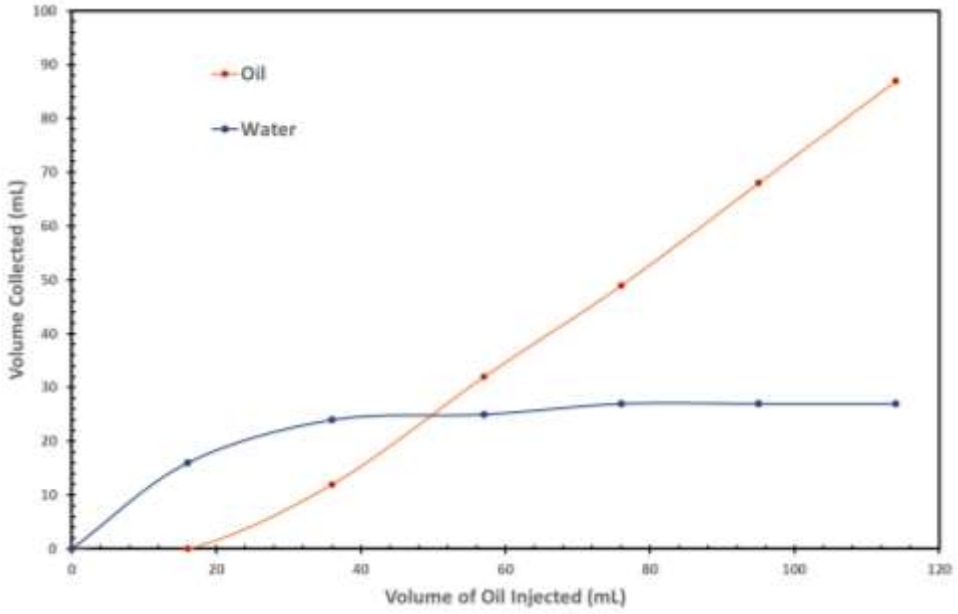

Figure A. 6: The oil loading curve of Core #15: Pore volume 39.7 mL.

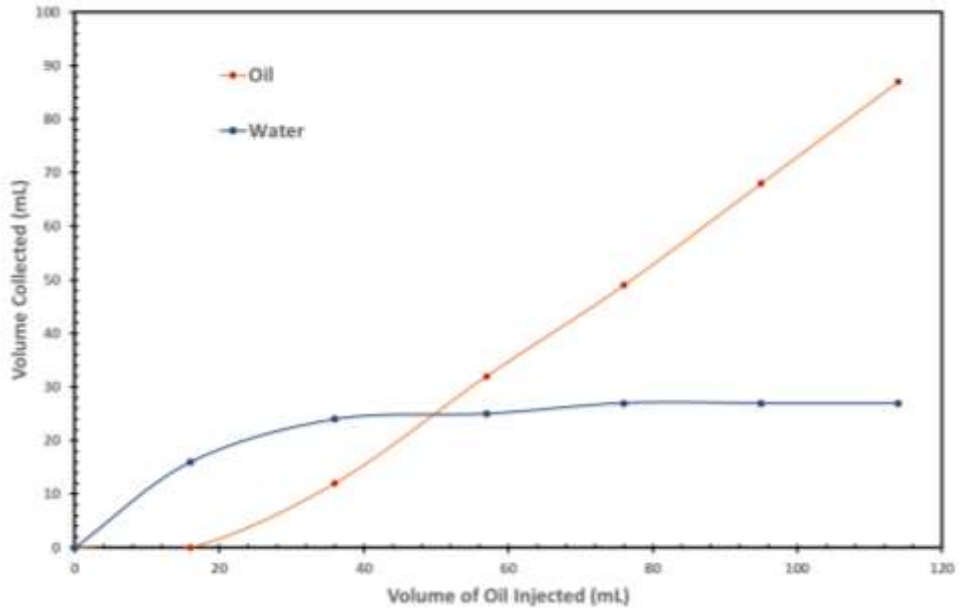

Figure A. 7: The oil loading curve of Core #16: Pore volume 36.4 mL.

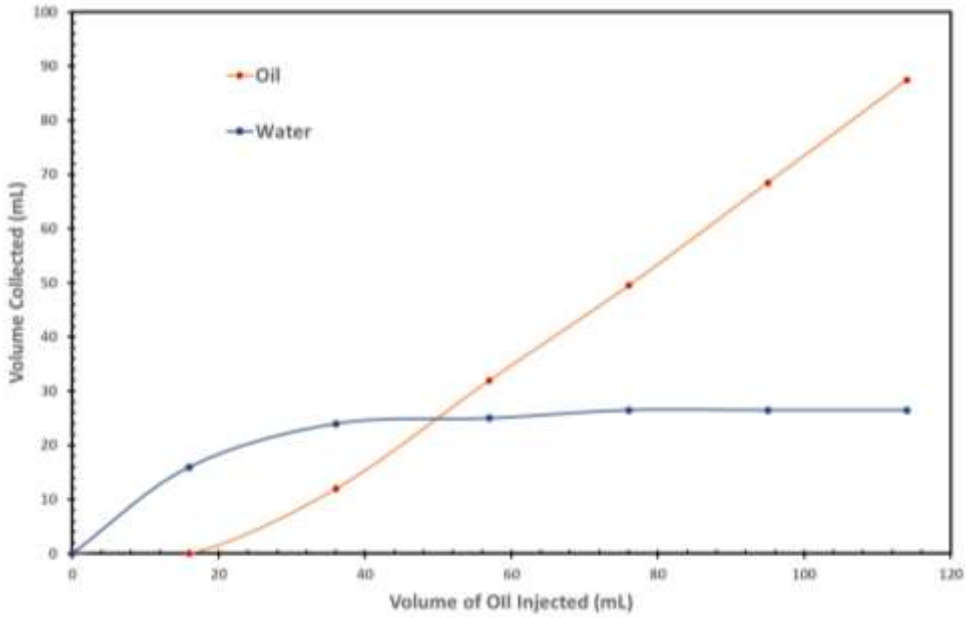

Figure A. 8: The oil loading curve of Core #17: Pore volume 34.9 mL.

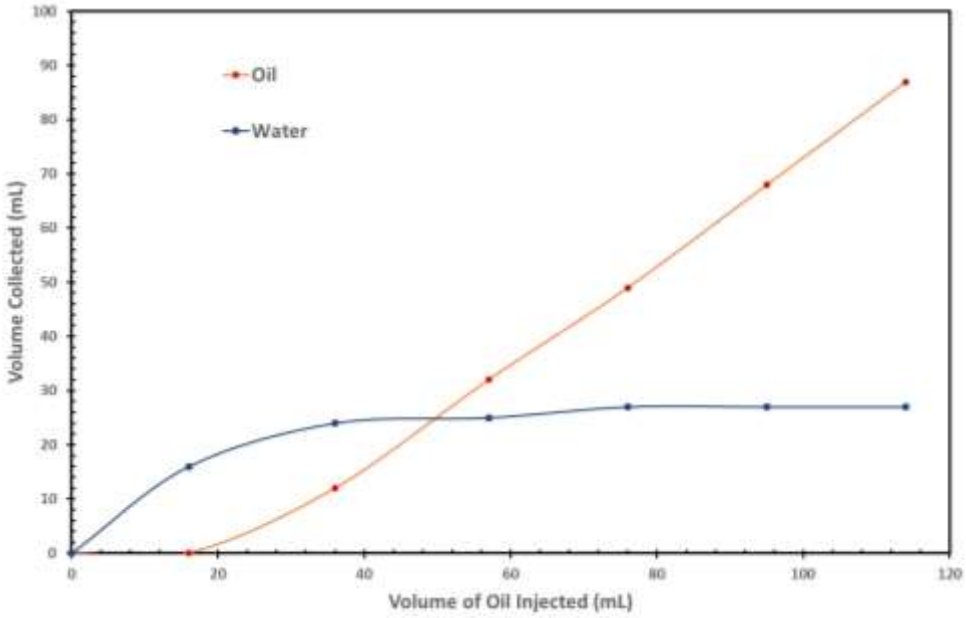

Figure A. 9: The oil loading curve of the Core #18: Pore volume 36.8 mL.

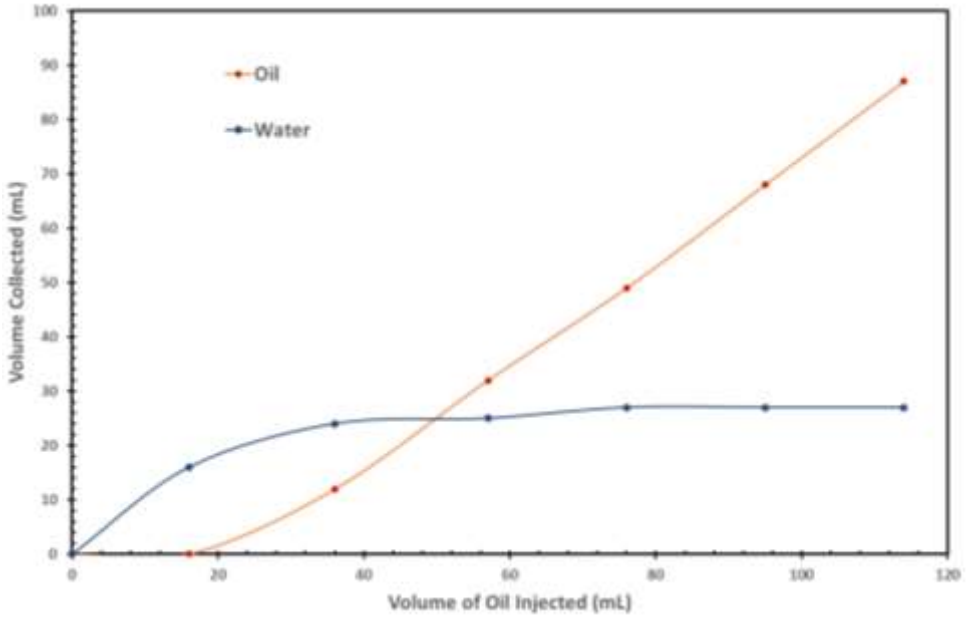

Figure A. 10: The oil loading curve of the Core #19: Pore volume 35.3 mL.

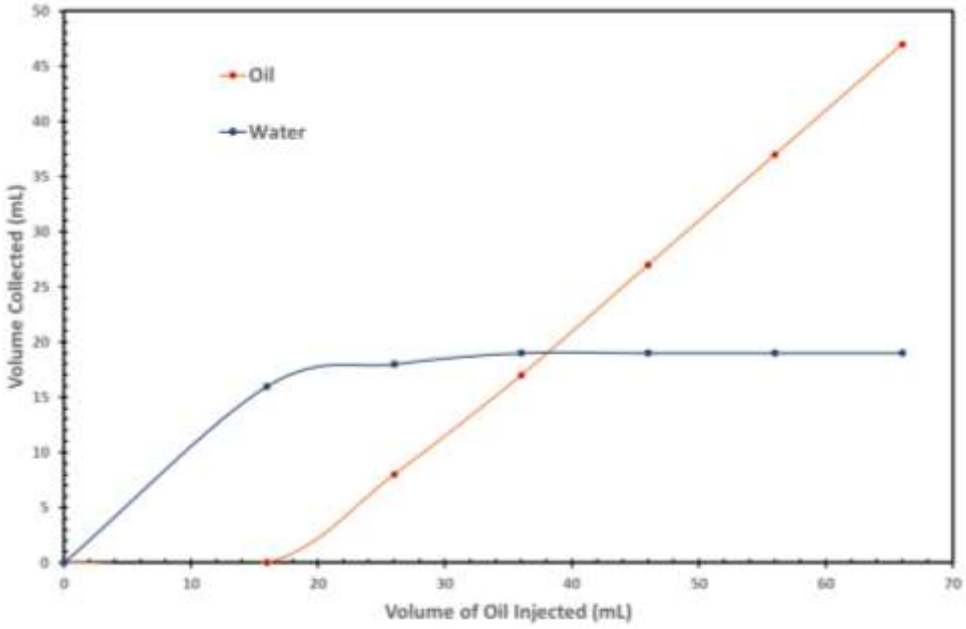

Figure A. 11: The oil loading curve of Core #20: Pore volume 32.9 mL.

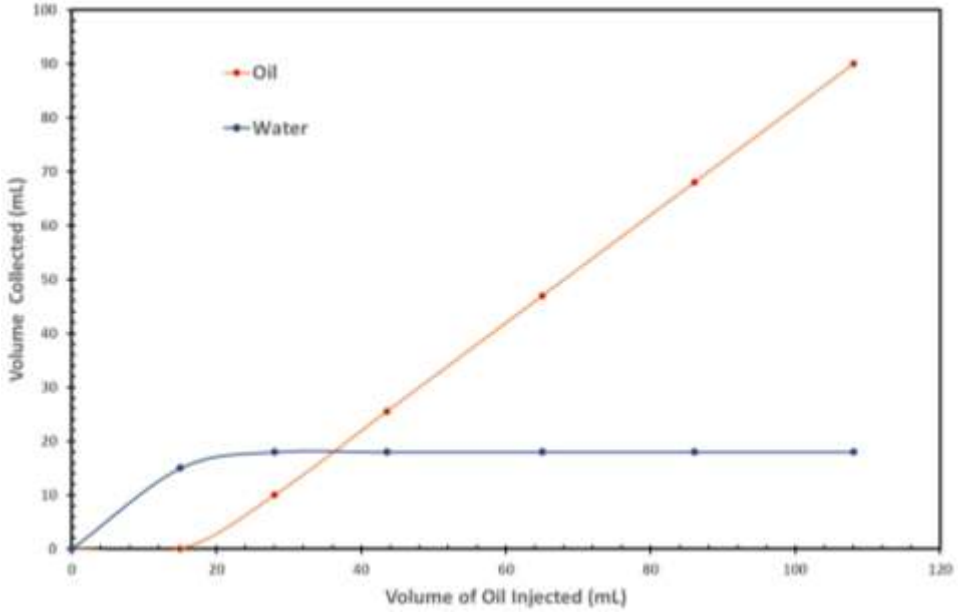

Figure A. 12: The oil loading curve of Core #21: Pore volume 31.8 mL.

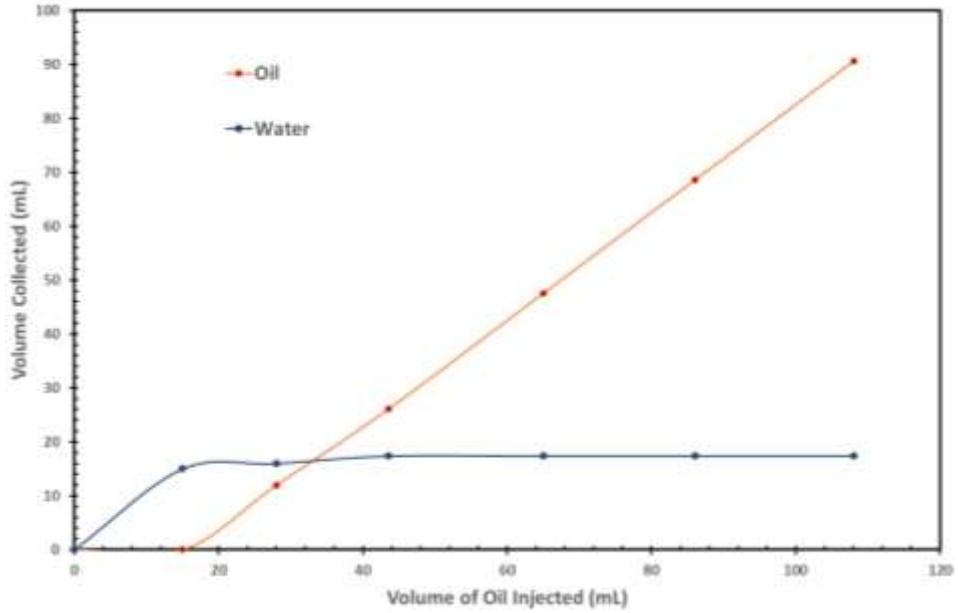

Figure A. 13: The oil loading curve of Core #22: Pore volume 34.8 mL.

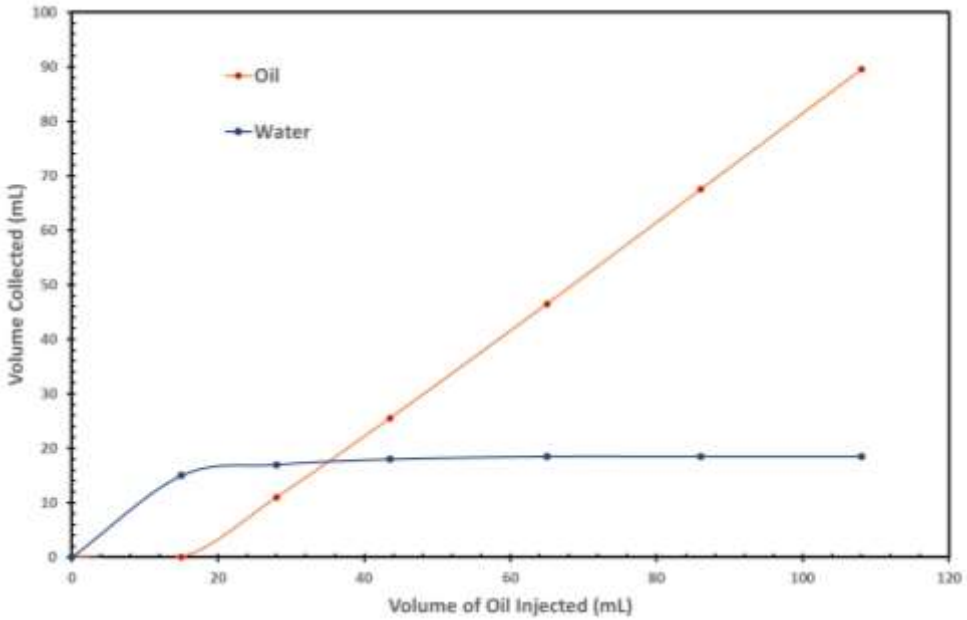

Figure A. 14: The oil loading curve of Core #23: Pore volume 38.3 mL.

Appendix B: Water flooding of all cores

Figures B.1-14 present the water flooding curve of cores #5, 6, 9, 11, 14, 15, 16, 17, 18, 19, 20, 21, 22, and 23 respectively. Providing a graphical representation of the results from Chapter 6.4.

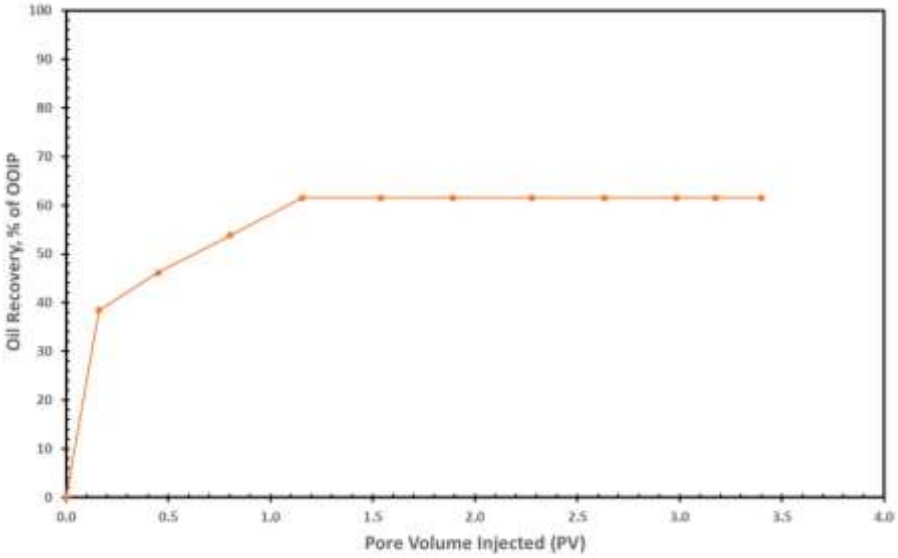

Figure B. 1: The Oil recovery curve of the oil loaded in Core #5 during water flooding OOIP = 41.7%.

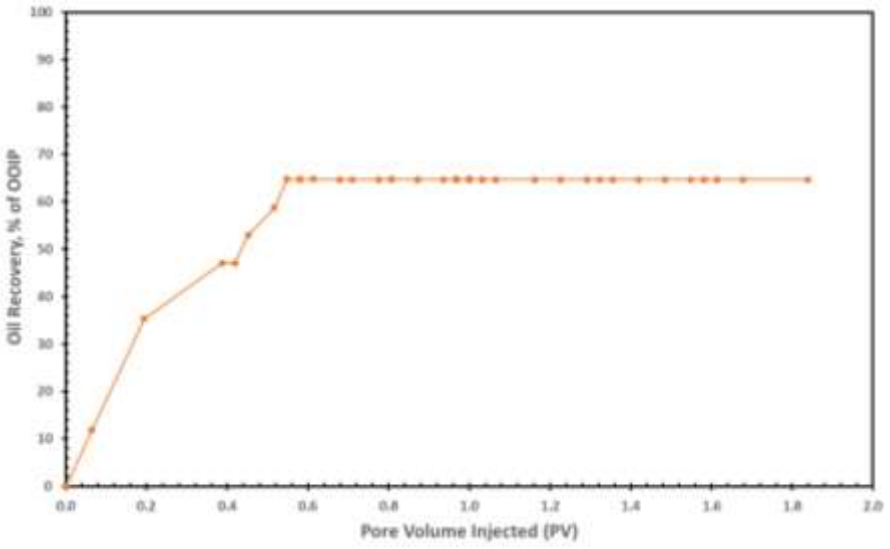

Figure B. 2: The Oil recovery curve of the oil loaded in Core #6 during water flooding OOIP = 54.9%.

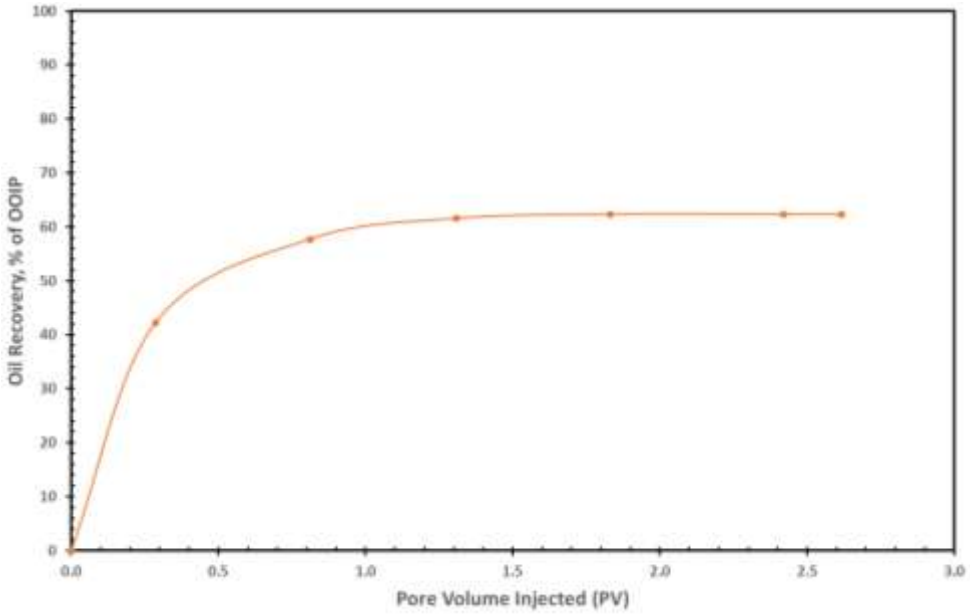

Figure B. 3: The Oil recovery curve of the oil loaded in Core #9 during water flooding OOIP = 68.0%.

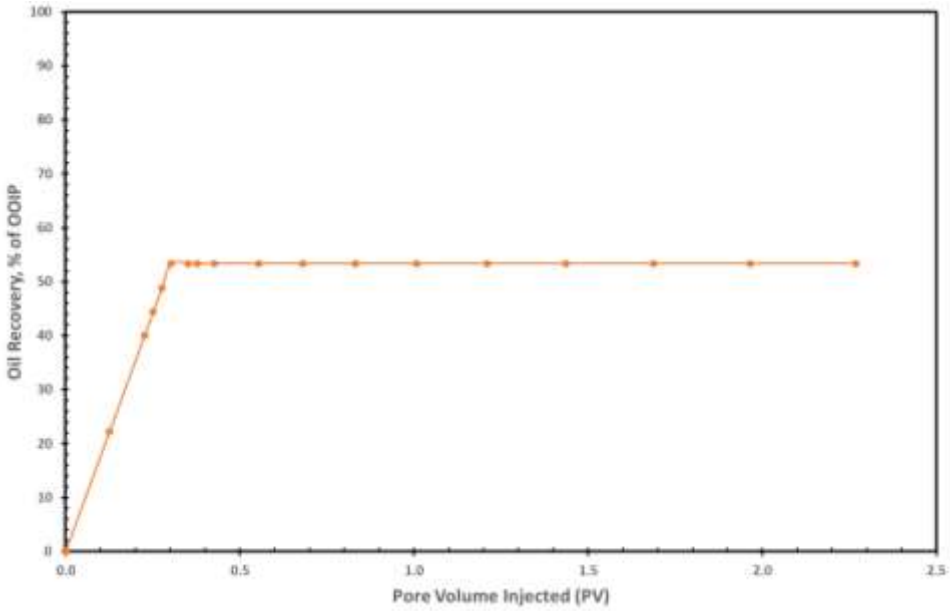

Figure B. 4: The Oil recovery curve of the oil loaded in Core #11 during water flooding OOIP = 56.7%.

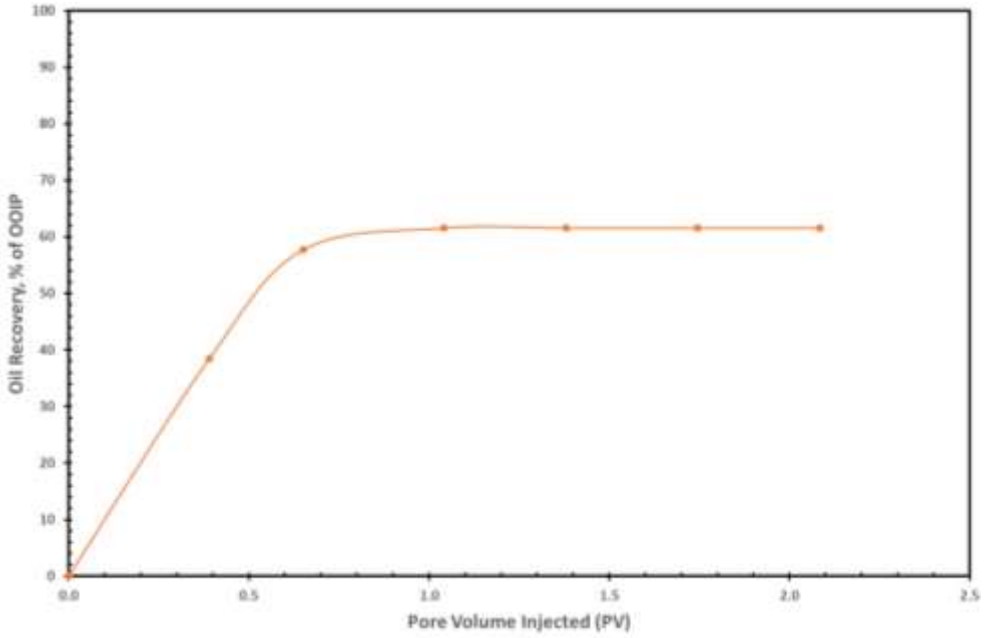

Figure B. 5: The Oil recovery curve of the oil loaded in Core #14 during water flooding OOIP = 67.7%.

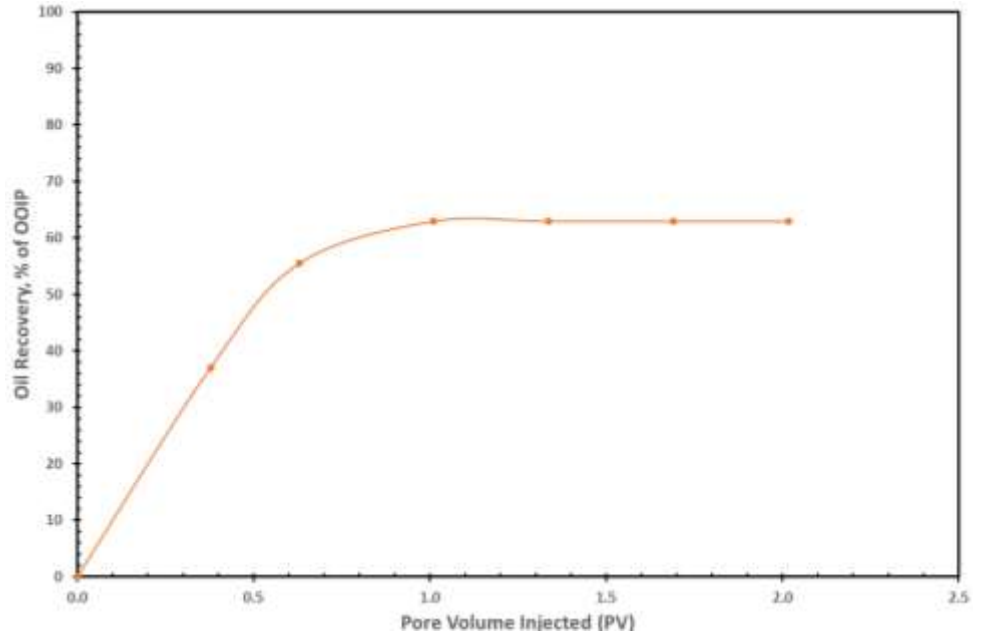

Figure B. 6: The Oil recovery curve of the oil loaded in Core #15 during water flooding OOIP = 68.1%.

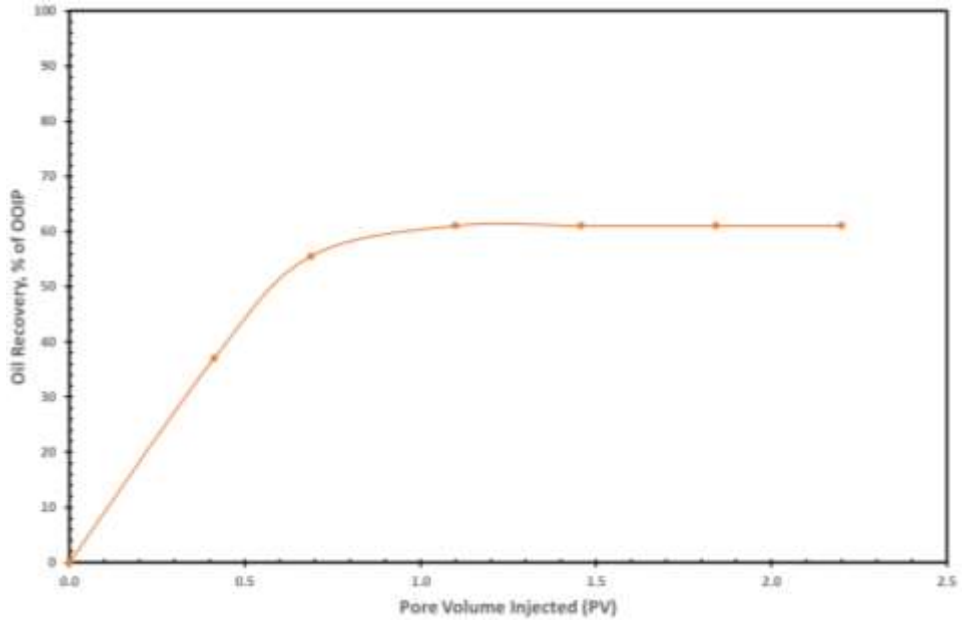

Figure B. 7: The Oil recovery curve of the oil loaded in Core #16 during water flooding OOIP = 74.1%.

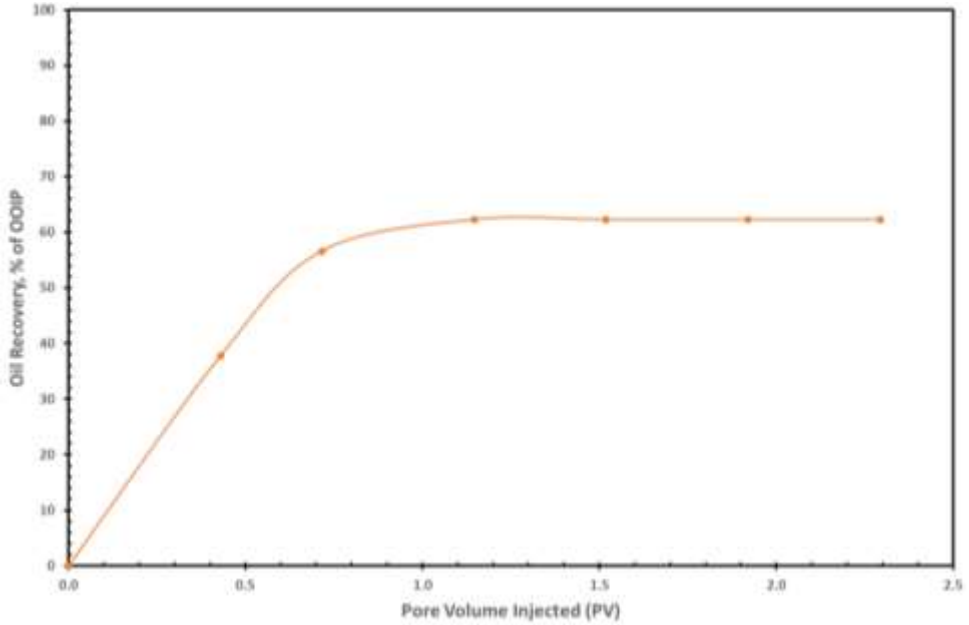

Figure B. 8: The Oil recovery curve of the oil loaded in Core #17 during water flooding OOIP = 76.0%.

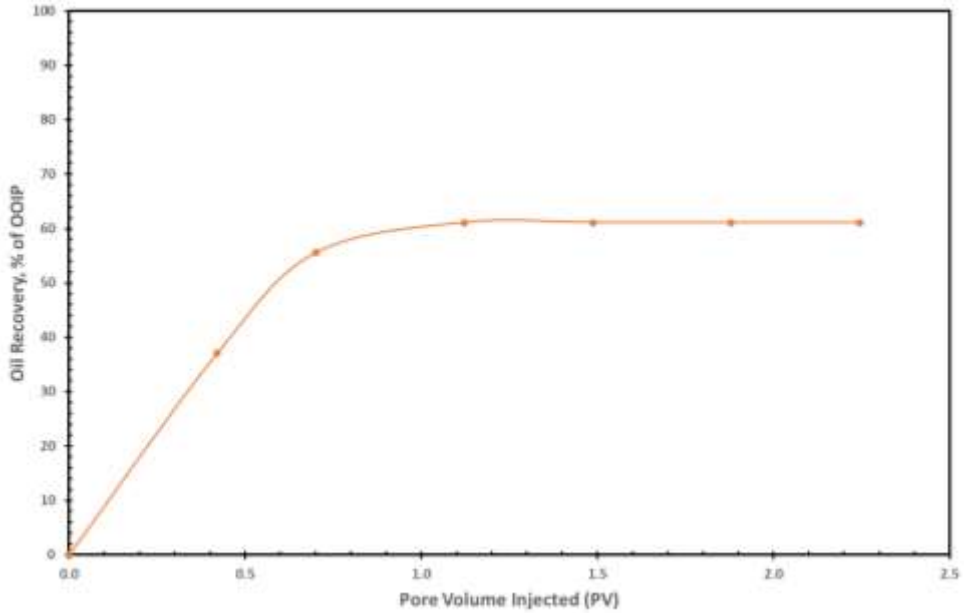

Figure B. 9: The Oil recovery curve of the oil loaded in Core #18 during water flooding OOIP = 75.7%.

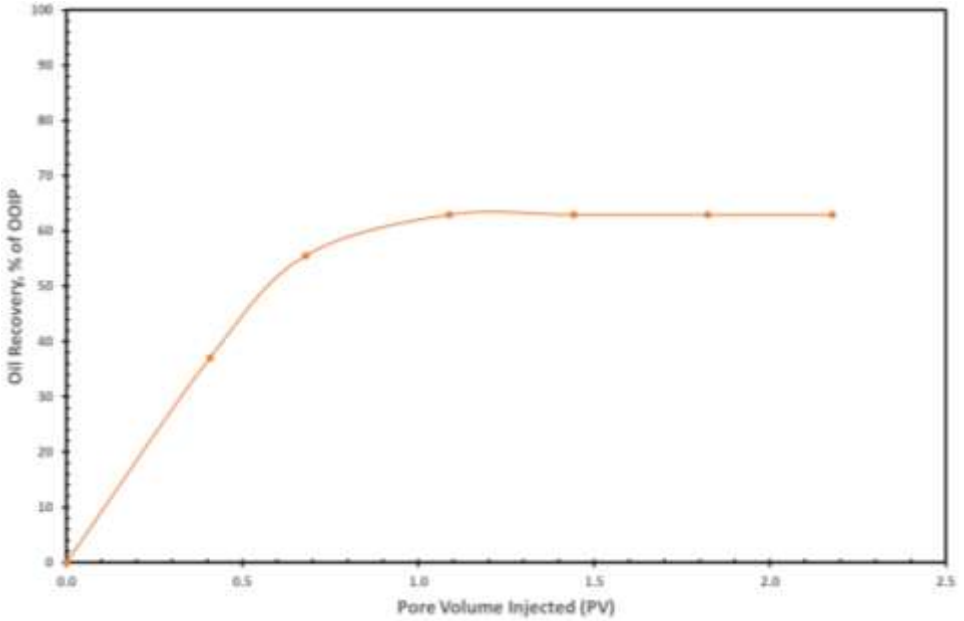

Figure B. 10: The Oil recovery curve of the oil loaded in Core #19 during water flooding OOIP = 73.4%.

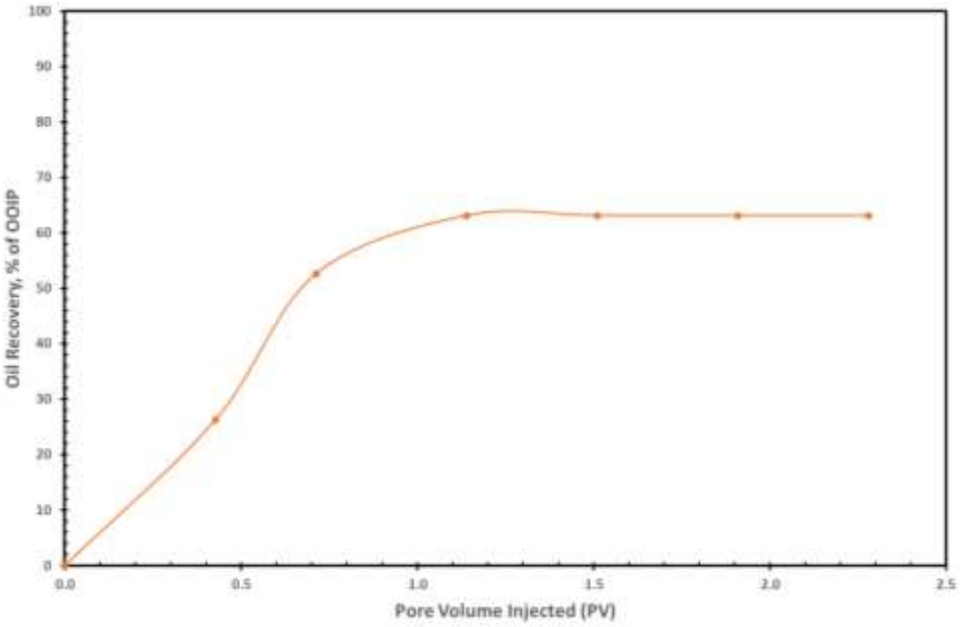

Figure B. 11: The Oil recovery curve of the oil loaded in Core #20 during water flooding OOIP = 54.2%.

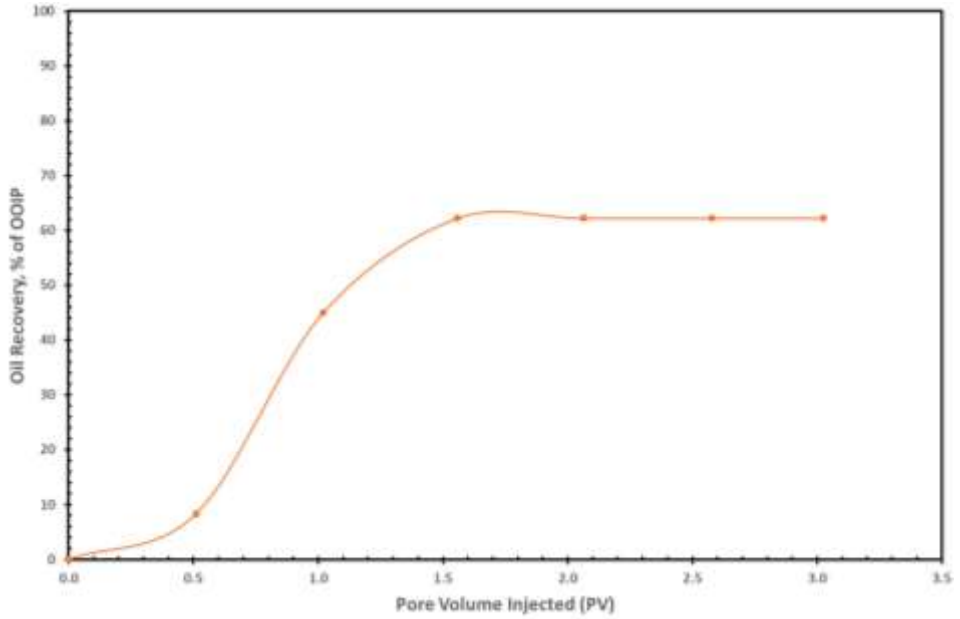

Figure B. 12: The Oil recovery curve of the oil loaded in Core #21 during water flooding OOIP = 51.0%.

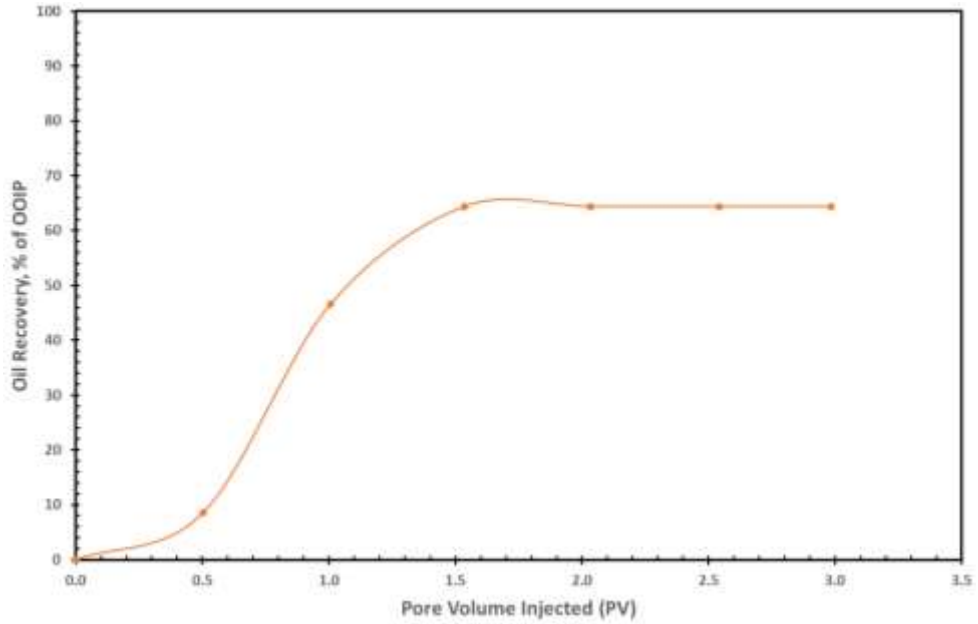

Figure B. 13: The Oil recovery curve of the oil loaded in Core #22 during water flooding OOIP = 48.6%.

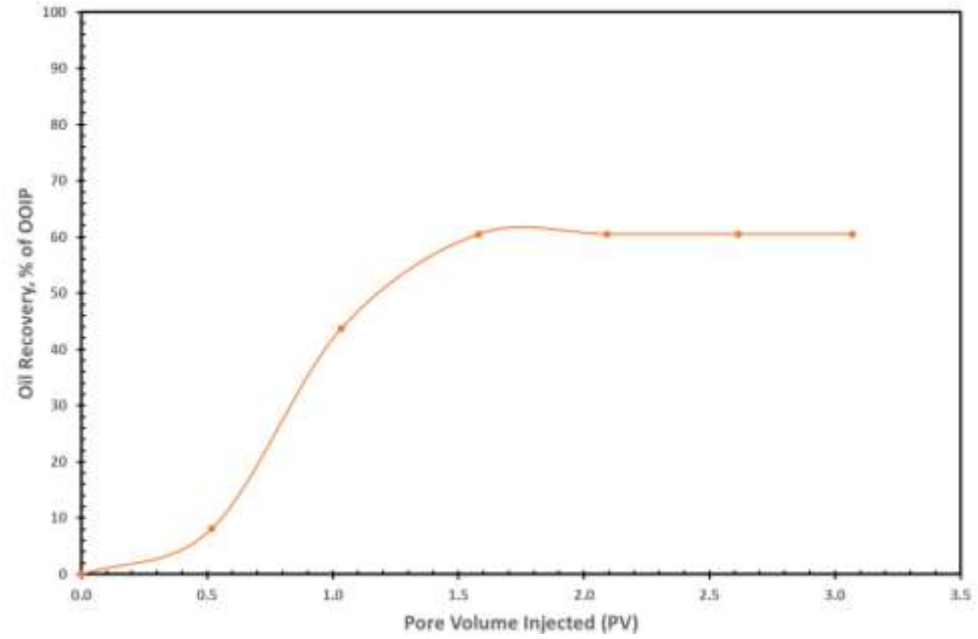

Figure B. 14: The Oil recovery curve of the oil loaded in Core #23 during water flooding OOIP = 53.2%.

Appendix C: Nanofluid flooding of cores

Figures C.1-14 present the sectional flooding curve of cores #5, 6, 9, 11, 14, 15, 16, 17, 18, 19, 20, 21, 22, and 23 respectively. Providing a graphical representation of the results from Chapter 6.5.

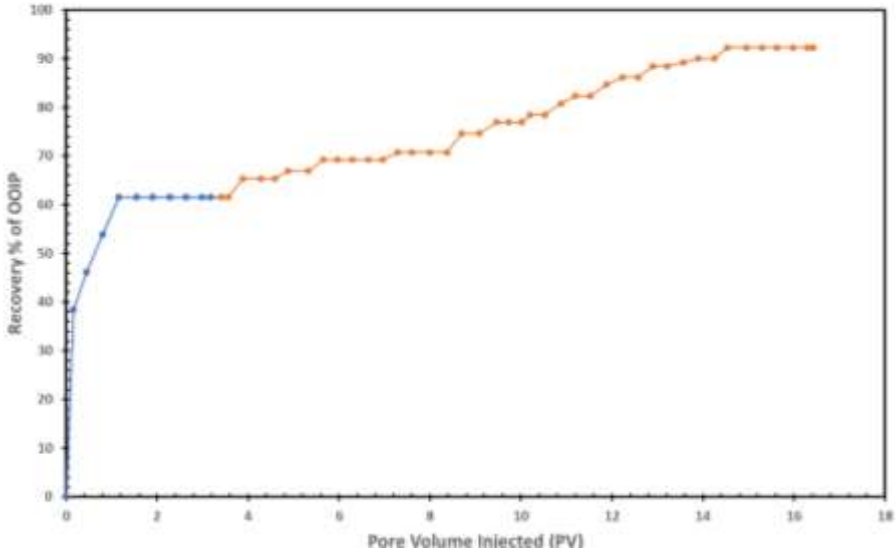

Figure C. 1: The oil recovery curve of the Sectional flooding of 2 wt% pH 2.0 AC nanofluid of Core #5. The blue line represents water flooding and the orange line represents sectional flooding.

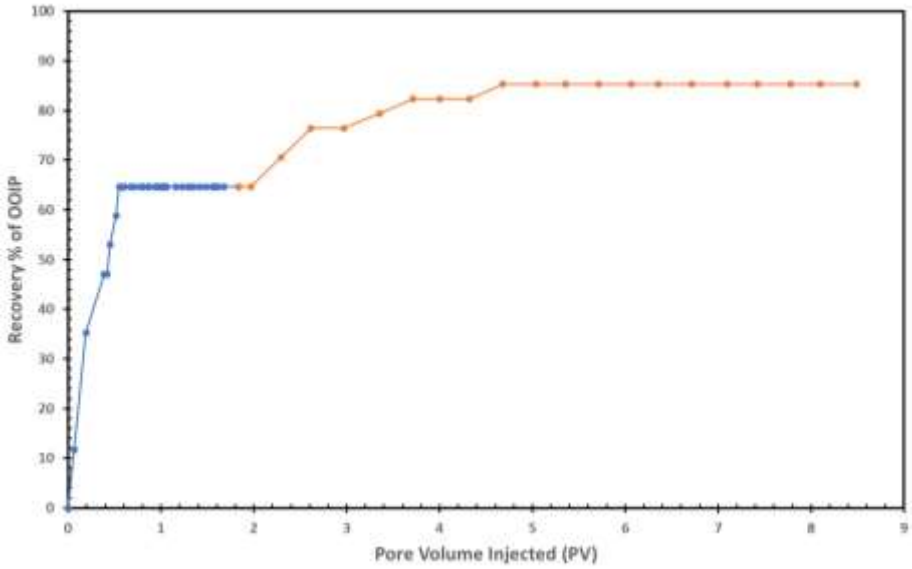

Figure C. 2: The oil recovery curve of the Sectional flooding of 2 wt% pH 6.0 AC nanofluid of Core #6. The blue line represents water flooding and the orange line represents sectional flooding.

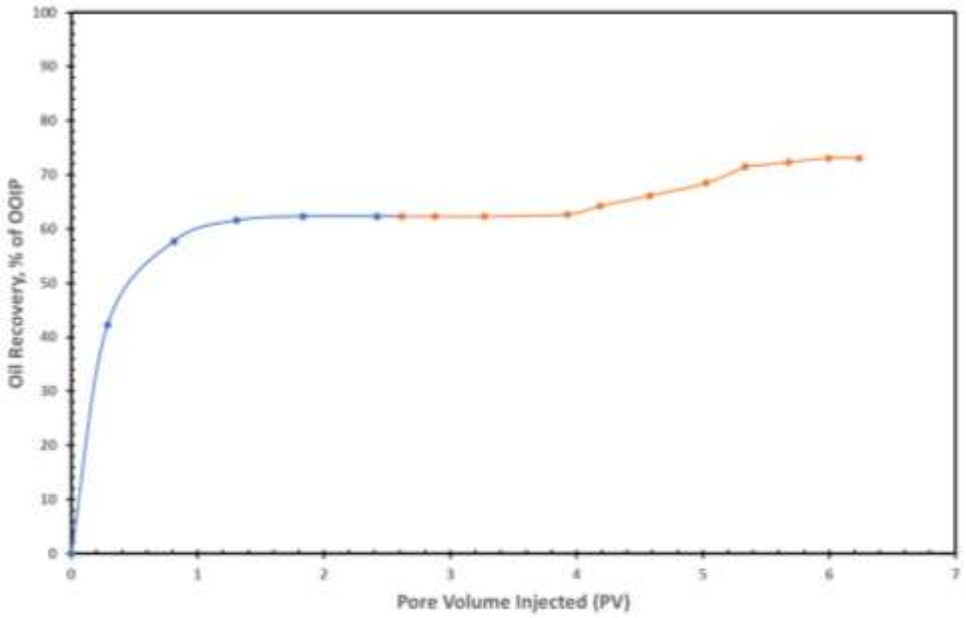

Figure C. 3: The oil recovery curve of the Sectional flooding of 2 wt% pH 2.0 RHC nanofluid of Core #9. The blue line represents water flooding and the orange line represents sectional flooding.

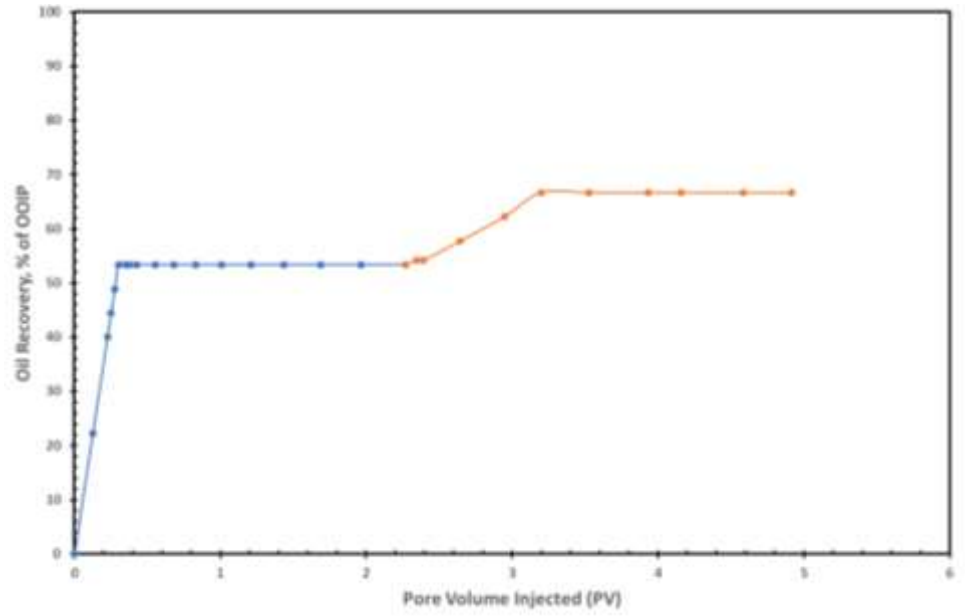

Figure C. 4: The oil recovery curve of the Sectional flooding of 2 wt% pH 6.0 WSC nanofluid of Core #11. The blue line represents water flooding and the orange line represents sectional flooding.

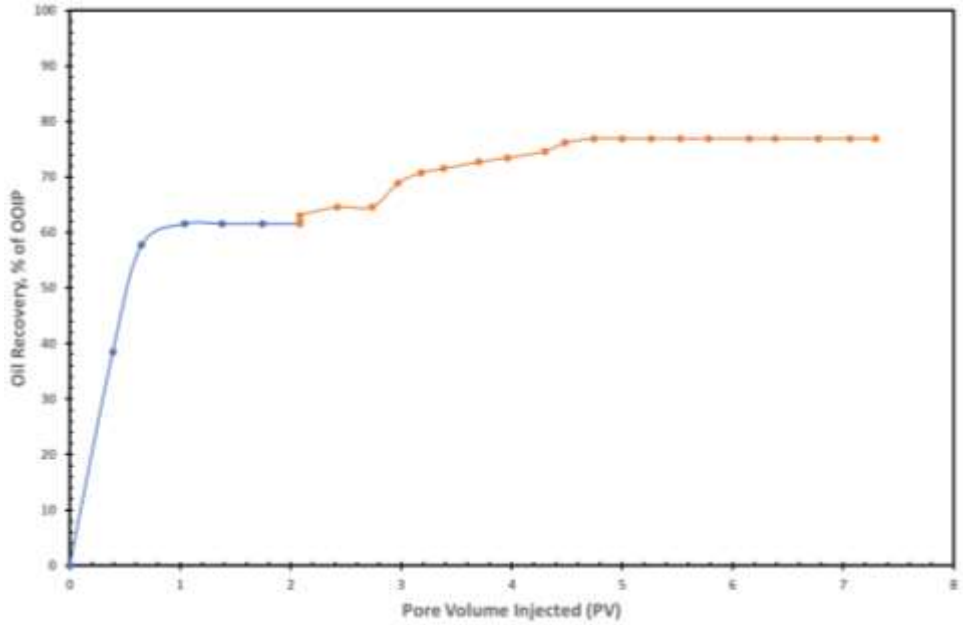

Figure C. 5: The oil recovery curve of the Sectional flooding of 1 wt% pH 6.0 AC nanofluid of Core #14. The blue line represents water flooding and the orange line represents sectional flooding.

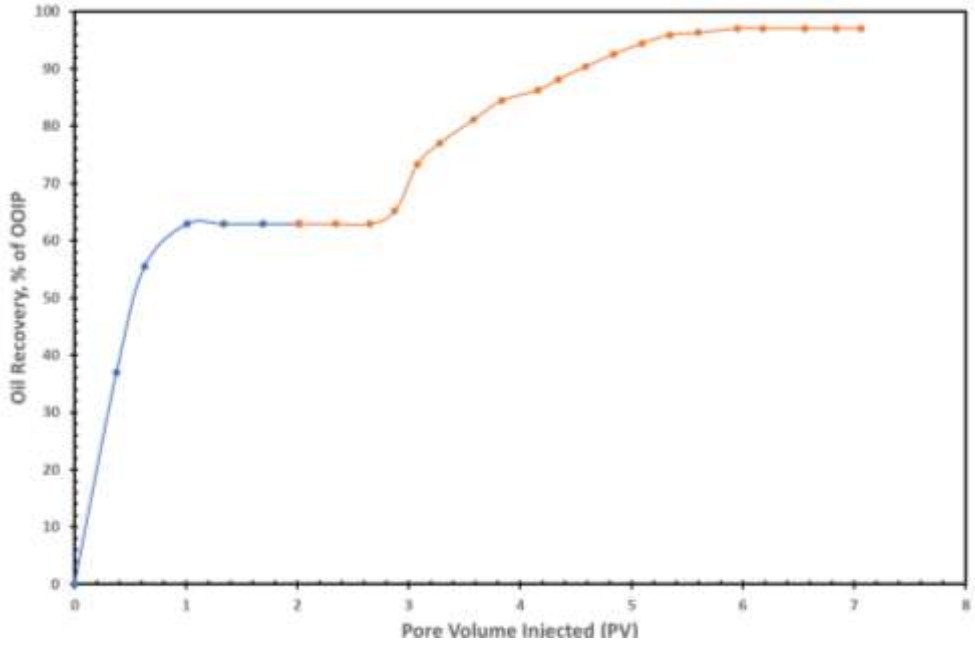

Figure C. 6: The oil recovery curve of the Sectional flooding of 2 wt% pH 2.0 AC nanofluid of Core #15. The blue line represents water flooding and the orange line represents sectional flooding.

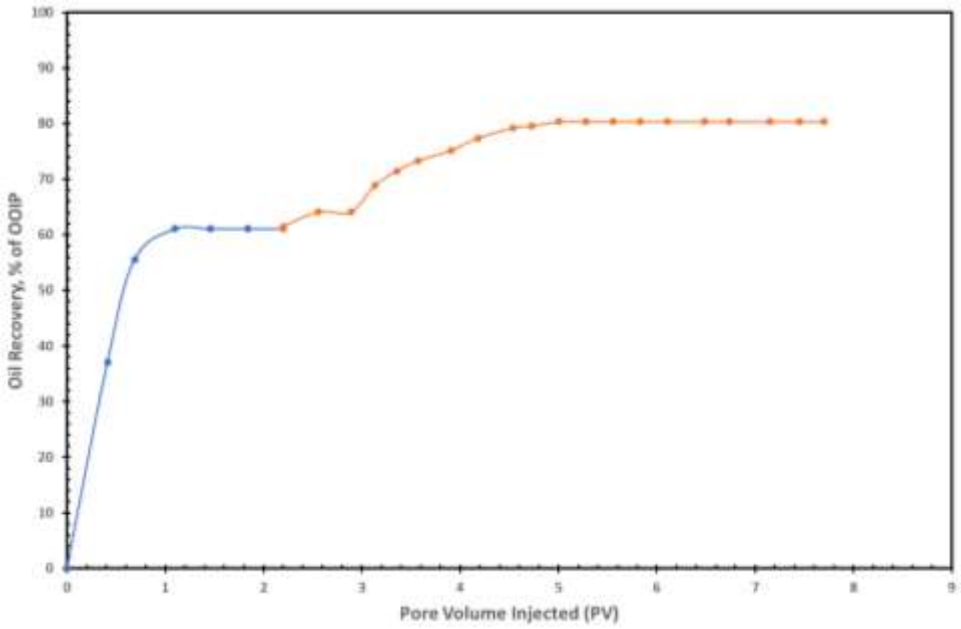

Figure C. 7: The oil recovery curve of the Sectional flooding of 2 wt% pH 6.0 AC nanofluid of Core #16. The blue line represents water flooding and the orange line represents sectional flooding.

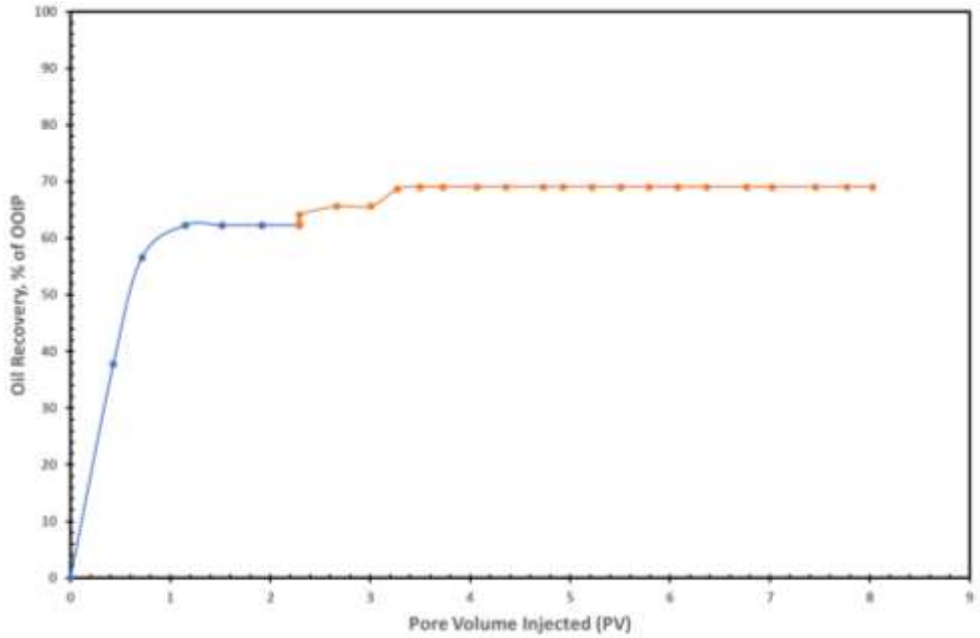

Figure C. 8: The oil recovery curve of the Sectional flooding of 2 wt% pH 6.0 RHC nanofluid of Core #17. The blue line represents water flooding and the orange line represents sectional flooding.

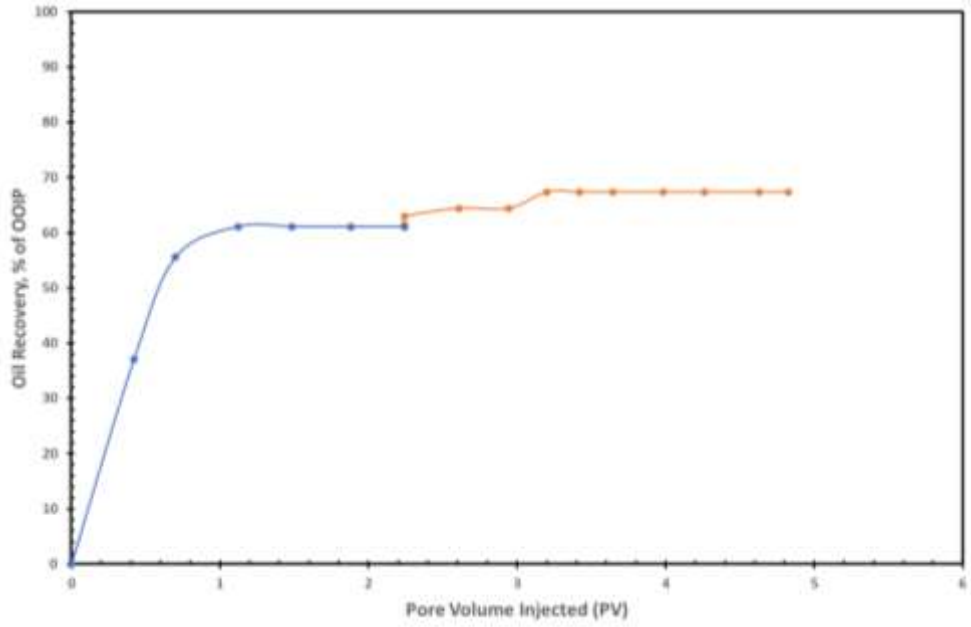

Figure C. 9: The oil recovery curve of the Sectional flooding of 1 wt% pH 6.0 WSC nanofluid of Core #18. The blue line represents water flooding and the orange line represents sectional flooding.

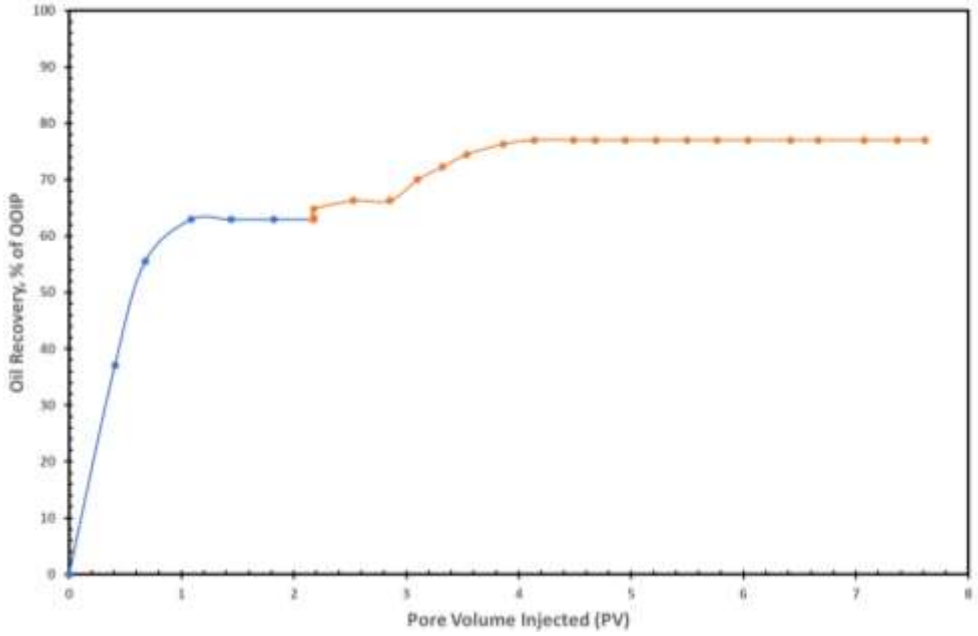

Figure C. 10: The oil recovery curve of the Sectional flooding of 2 wt% pH 2.0 WSC nanofluid of Core #19. The blue line represents water flooding and the orange line represents sectional flooding.

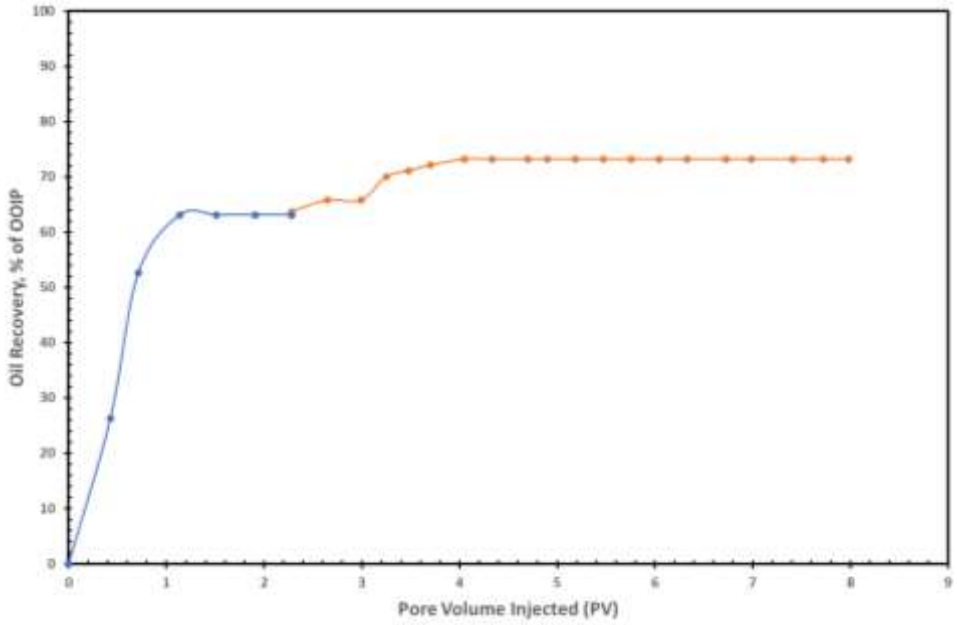

Figure C. 11: The oil recovery curve of the Sectional flooding of 2 wt% pH 2.0 RHC nanofluid of Core #20. The blue line represents water flooding and the orange line represents sectional flooding.

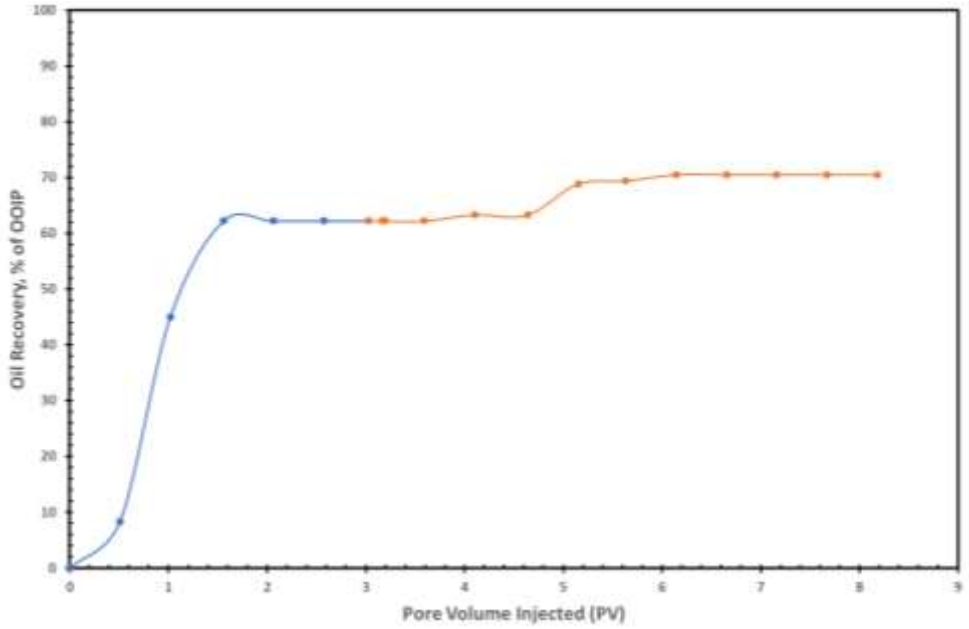

Figure C. 12: The oil recovery curve of the Sectional flooding of 2 wt% pH 6.0 RHC nanofluid of Core #21. The blue line represents water flooding and the orange line represents sectional flooding.

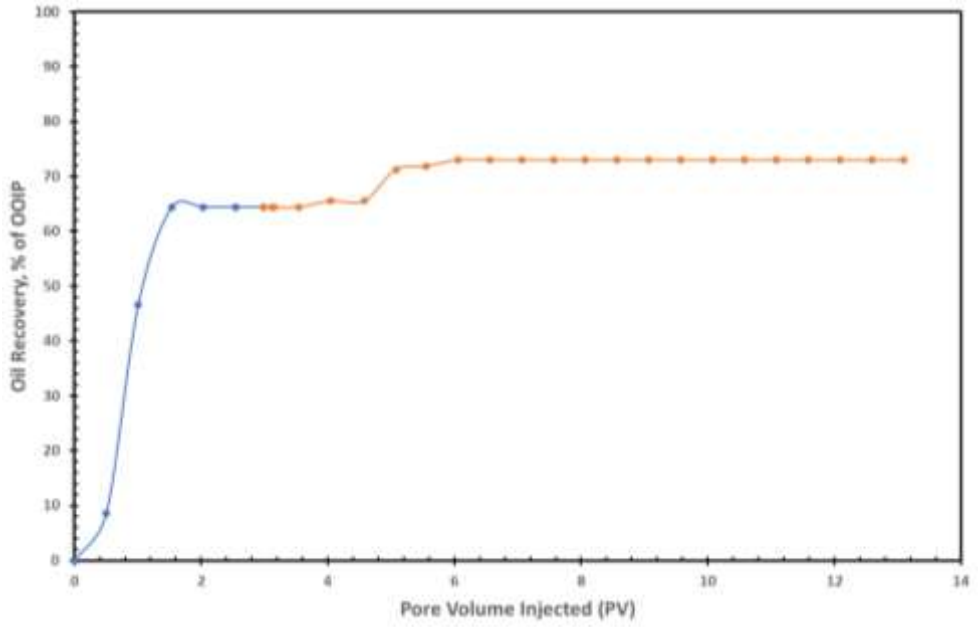

Figure C. 13: The oil recovery curve of the Sectional flooding of 2 wt% pH 6.0 WSC nanofluid of Core #22. The blue line represents water flooding and the orange line represents sectional flooding.

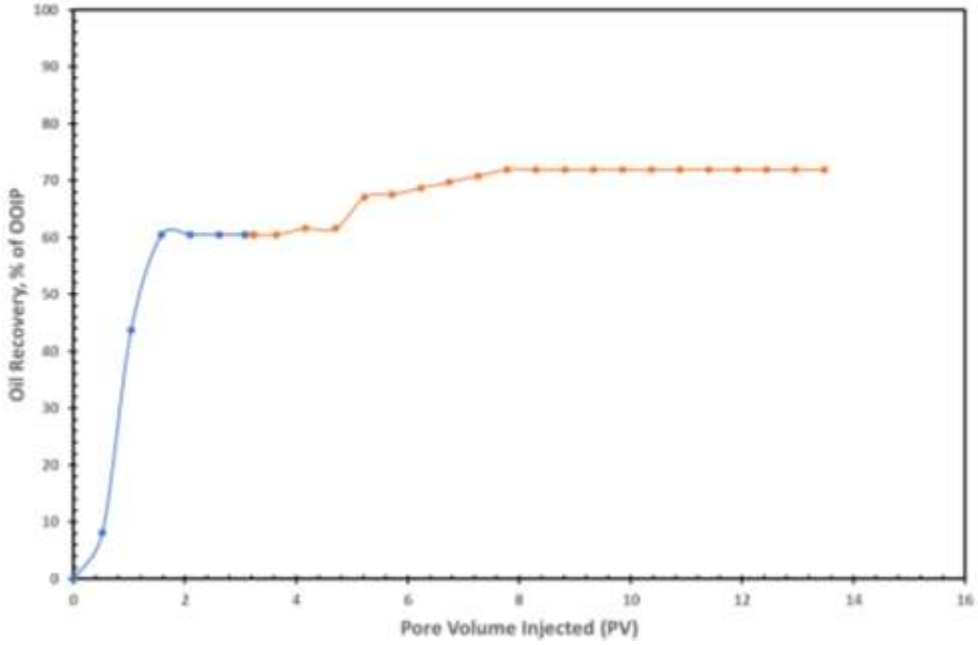

Figure C. 14: The oil recovery curve of the Sectional flooding of 2 wt% pH 2.0 WSC nanofluid of Core #23. The blue line represents water flooding and the orange line represents sectional flooding.

Appendix D: Lists of publications

Akande, I., Bridgwater, T., van Koningsbruggen, P. J., & Yuan, Q. (2023). Advances in the modelling of concentration-dependent relative viscosity data for nanofluids by introducing the Dispersion Factor. Journal of Molecular Liquids, 380, Article 121644. https://doi.org/10.1016/j.molliq.2023.121644

Akande, I., Bridgwater, T., van Koningsbruggen, P. J., & Yuan, Q. (2023). A viscosity study of charcoal-based nanofluids towards enhanced oil recovery. Journal of Molecular Liquids, 387, Article 122615. https://doi.org/10.1016/j.molliq.2023.122615